PERFORMING PARTICLE IMAGE VELOCIMETRY IN A SUPERSONIC

WIND TUNNEL USING CARBON DIOXIDE AS THE SEED MATERIAL

THESIS

Donald Wallace Peltier III, Ensign, USN

AFIT/GAE/ENY/07-J17

DEPARTMENT OF THE AIR FORCE

AIR UNIVERSITY

AIR FORCE INSTITUTE OF TECHNOLOGY

Wright-Patterson Air Force Base, Ohio

PERFORMING PARTICLE IMAGE VELOCIMETRY IN A SUPERSONIC WIND TUNNEL USING CARBON DIOXIDE AS THE SEED MATERIAL

THESIS

Presented to the Faculty

Department of Aeronautics and Astronautics

Graduate School of Engineering and Management

Air Force Institute of Technology

Air University

Air Education and Training Command

In Partial Fulfillment of the Requirements for the

Degree of Master of Science in Aeronautical Engineering

Donald W. Peltier III, BS

Ensign, USN

June 2007

AFIT/GAE/ENY/07-J17

PERFORMING PARTICLE IMAGE VELOCIMETRY IN A SUPERSONIC

WIND TUNNEL USING CARBON DIOXIDE AS THE SEED MATERIAL

Donald W. Peltier III, BS

Ensign, USN

Approved:

_____   _____

Dr. Mark F. Reeder (Chairman)   Date

_____   _____

Maj Richard Branam (Member)   Date

_____   _____

Lt Col Raymond C. Maple (Member)   Date

AFIT/GAE/ENY/07-J17

Abstract

Particle image velocimetry (PIV) was performed utilizing clean seed particles generated by injecting liquid carbon dioxide (CO_2) directly into an open-circuit blowdown Mach 2.9 supersonic wind tunnel. Rapid atomization and cooling of the liquid CO_2 created a preponderance of nearly uniform and well dispersed microscopic dry ice particles which were illuminated using a frequency double Nd:YAG laser. Ample light was scattered from the flow tracers, which provided a strong signal to noise ratio. The particles completely sublimed into an innocuous gas downstream of the test section causing no side effects or problems with wind tunnel operation. A variety of geometries were inspected using PIV. In addition to empty test section characterization, flow aft of a cone and transverse injection through a long shallow cavity was visualized and adaptive cross-correlation vector maps were computed. These vector maps revealed many relevant flow structures pertinent to each test setup. Measured velocities followed the trends expected for each test setup but the vector magnitudes were shifted 3-9% below those predicted by theory. Procedures and information pertinent to liquid CO_2 injection are provided to help researchers implement this process in similarly scaled supersonic wind tunnels.

For my Father, Mother, and Brother

You are at the heart of every good thing that I do.

Acknowledgments

Table of Contents

List of Figures

List of Tables

List of Symbols

English Symbols

a	local speed of sound [m/s]
A	local flow area [m^2]
A^*	nozzle throat flow area [m^2]
c	local speed of light [m/s]
c_{vac}	speed of light in a vacuum [m/s]
C_p	mixture mass specific heat at constant pressure [J/kg-K]
C_{p_i}	constituent mass specific heat at constant pressure [J/kg-K]
C_v	mixture mass specific heat at constant volume [J/kg-K]
d	seed particle diameter [m]
D	distance traveled by seed particle [pixels]
D_{MAX}	desired maximum particle displacement [m]
e	mixture mass specific internal energy [J/kg]
f	Darcy friction factor
F	particle size factor
g	gravitational acceleration constant [m/s^2]
h	mixture mass specific enthalpy [J/kg]
h_L	static pressure head loss [m]
h_O	mixture mass specific stagnation enthalpy [J/kg]
H	total pipe head [m]
ID	pipe inner diameter [m]
K	resistance factor
K_T	total piping branch resistance factor
K_{90}	resistance factor in local 90° bend
ℓ	number of coils in piping system

L pipe length [m]

m mixture mass [kg]

m_i constituent mass [kg]

$\hat{m}$ mixture molecular weight [kg/kgmol]

$\hat{m}_i$ constituent molecular weight [kg/kgmol]

$\dot{m}$ mixture mass flow rate [kg/s]

M local Mach number

n index of refraction

n_{90} number of 90° bends in local piping

N dimension of square interrogation region [pixels]

P mixture absolute static pressure [Pa = N/m^2 = kg/m-s^2]

P_{atm} local atmospheric static pressure [Pa]

P_G mixture gage static pressure [Pa]

P_O mixture absolute stagnation pressure [Pa]

q heat transferred per unit mass [J/kg]

$\bar{q}$ jet to freestream momentum flux ratio

r local 90° elbow bend radius [m]

R mixture mass specific gas constant [J/kg-K]

$\hat{R}$ universal gas constant = 8314.3 [J/kgmol-K]

Re   Reynolds number

s mixture mass specific entropy [J/kg-K]

S object plane to camera image plane scale factor [length/pixels]

t time elapsed during seed particle translation [s]

T mixture absolute static temperature [K]

T_O mixture absolute stagnation temperature [K]

U local one dimensional flow velocity [m/s]

V volume occupied by gas mixture [m^3]

v mixture mass specific volume [m^3/kg]

$\vec{V}$ local flow velocity [m/s]

We   Weber number

Z   elevation head [m]

Greek Symbols

α transverse injection angle [rad]

β shock wave angle [rad]

γ mixture ratio of specific heats

ΔP pressure drop across a pipe section [Pa]

ε local piping inner diameter ratio

θ local flow deflection angle [rad]

λ electromagnetic light wavelength [m]

μ dynamic viscosity [kg/m-s]

υ Prandtl-Meyer function [rad]

ρ mixture static density [kg/m^3]

ρ_o mixture stagnation density [kg/m^3]

σ liquid surface tension [N/m]

τ breakup regime parameter

ϕ reference pipe inner diameter ratio

List of Acronyms

1-D	one dimensional
2-D	two dimensional
3-D	three dimensional
AFIT	Air Force Institute of Technology
C-D	converging-diverging
CCD	charged couple device
CFD	computational fluid dynamics
CO_2	carbon dioxide
CP	control pressure
DAQ	data acquisition
FFT	fast Fourier transform
HP	high pressure
ID	inner diameter
IM	image map
IR	interrogation region
NACA	National Advisory Committee for Aeronautics
Nd:YAG	neodymium yittrium aluminum garnett
NI	National Instruments
OD	outer diameter
PIV	particle image velocimetry
VI	virtual instrument

PERFORMING PARTICLE IMAGE VELOCIMETRY IN A SUPERSONIC

WIND TUNNEL USING CARBON DIOXIDE AS THE SEED MATERIAL

1.   Introduction

1. 1   Motivation and Hypothesis

Fluid flow, the invisible art form of nature, is continually occurring around us. From the slow swirling of air in a classroom, to air rushing over the body of a car or the wings of an airplane, fluids are constantly in motion. The power of this motion can be harnessed to benefit humankind such as enabling an airplane to fly. Today scientists and researchers are developing ever improving mathematical models to describe fluidic motion. However, these computational fluid dynamics (CFD) models are left open to speculation and inquisition if they can not be confirmed by experimental evidence. Ernest Mach, a founding father of flow visualization stated "Modern science strives to construct its picture of the world not from speculations but so far as possible from facts. It verifies its constructs by recourse to observation." (Merzkirch, 1974:2) For visual verification to be accomplished, the actual motion of normally transparent (infinitesimal) fluid particles must be illuminated and recorded. This is indeed a monumental task, but the benefits of such an undertaking are clear. Once empirically confirmed, validated

CFD flow models could accurately predict the velocity field present around a particular geometric shape immersed in a flow. Furthermore this would yield the surface forces generated by the given geometry. Empowering engineers with this understanding, of how form effects force relations for application in design, is a major goal of fluid velocity measurement through flow visualization.

Fundamental measurement techniques used to monitor flow properties such as pressure, which is used to calculate flow velocity, require an external measuring device such as transducers or hot wire anemometers be placed in the flow path. These devices are inherently intrusive and cause discrepancies between measured flow properties and those that would have existed without the presence of the measuring device. Unfortunately, it is generally not possible to measure flow properties without the addition of some foreign material. However, minimizing the effective impact the added material has on the flow can limit the difference between the measured value and the actual value to negligible proportions.

In particle image velocimetry (PIV) small microscopic particles, generally spheres one micrometer (1 μm) in diameter, are added to a moving fluid and photographed for flow visualization (Melling, 1997:1411). Fortunately, due to their small size these flow tracing particles, or *seeds*, normally have little effect on the main flow. However, most traditional seed materials that have favorable characteristics for application with PIV are disruptive, or even hazardous to wind tunnel equipment. Wind tunnel equipment such as dryers, compressors and electronics utilized to recondition the flow media (air for example) for recirculation through a closed circuit wind tunnel can be damaged by

particle build up on surfaces or particle combustion due to high temperatures. Additionally, particle abrasion or build up can also have adverse effects on non-PIV related measurement equipment simultaneously employed during an experiment such as pressure sensitive paints and load cells. Preservation requires the wind tunnel be decommissioned for cleaning on a regular basis, which translates into a loss of facility productivity, and ultimately money.

It is proposed that carbon dioxide (CO_2) be used as the seed material in a supersonic wind tunnel for PIV primarily because of its self-cleaning attribute. Carbon dioxide is non-corrosive, non-flammable, non-toxic and most importantly can not build up on surfaces due to its phase characteristics; at room temperature and pressure, gas is the fundamental phase of CO_2. Successful feasibility research based on the clean seeding CO_2 hypothesis was completed by DeLapp (DeLapp, 2006) and recent application research performed by McNiel (McNiel, 2006) yielded promising results.

1. 2 Research Focus and Goals

The overarching goal of this research is to design a CO_2 seeding process for use with PIV that can be scaled for application in any supersonic wind tunnel. This paper will focus on three approaches to reach this goal. First, determine pertinent factors which affect the CO_2 from the time it leaves the storage tank until it exits the test section. This should afford future CO_2 researchers some understanding and control over seed dimensions and mixture constituents (discrete particles vs. vapor condensate). Second, find the optimal injector type and location to minimize system intrusiveness but maximize PIV results. Third, provide quality PIV examples using CO_2 seeds to further verify this technique with substantial visual evidence.

2.   Literature Review

2. 1   Compressible Gas Flows

In this paper *flow media,* or *medium*, refers to the gaseous mixture that flows through a wind tunnel. By definition, a gas is a continuum composed of molecules spread out relatively thin and thus have the potential to be compressed, or forced closer together. In fact, any fluid motion causes every real gas to be repeatedly compressed and expanded to some extent. However, density deviations from static, or motionless, values are generally insignificant at low Mach number flows (Anderson, 2003). The local Mach number M is defined as the ratio of local flow velocity $\vec{V}$ magnitude to local medium speed of sound a.

$$M = \frac{|\vec{V}|}{a} \tag{1}$$

Flows where the Mach number is less than 0.3 are generally assumed to be incompressible, which implies constant density. For most low speed problems incompressible flow can safely be assumed without introducing noticeable error into calculations. However the constant density assumption should be dropped if the density changes five percent or more due to fluid motion (Anderson, 2003:13).

5

2. 2. 1   Thermally Perfect Gases.

Most gases experiencing temperate thermodynamic flow conditions follow the ideal gas equation of state shown below and are termed *thermally perfect* or *ideal*. The gas absolute static pressure P, volume V, mass m, gas constant R, absolute static temperature T, and static density ρ can be related by

$$PV = mRT$$
$$P = \rho RT$$

(2)

The gas constant is calculated specifically for a particular gas using the universal gas constant $\hat{R} = 8314.3$ [J/kg-K] and the gas molecular weight $\hat{m}$, which should be noted is approximately 29 [kg/kgmol] for air (Hill and Peterson, 1992:33).

$$R = \frac{\hat{R}}{\hat{m}}$$

(3)

Absolute pressure is defined as the pressure felt at a given location due to local internal gage pressure P_G in addition to the ambient external atmospheric static pressure $P_{atm} = 101325$ Pa at sea level. A common conversion factor to obtain metric units is 1 [psi=lb$_f$/in^2] = 6894.7573 [Pa=N/m^2].

$$P = P_G + P_{atm}$$

(4)

The ideal gas equation holds when intermolecular forces are insignificant, which is a good assumption for most gases at moderate temperatures and pressures because of the relatively large ratio of molecular spacing to molecule size. Furthermore if a thermally perfect gas can be assumed to have approximately constant specific heats it is described as being calorically perfect. Thus a calorically perfect ideal gas shall be referred to as a *perfect gas* throughout the remainder of this paper. Real gas specific heats at constant pressure C_p and constant volume C_v are actually a function of temperature. However, a gas undergoing a thermodynamic process involving a minimal change in temperature, or a gas whose specific heat does not drastically change over the temperature range experienced, can safely be evaluated as a perfect gas for moderate temperatures (T<300K) (Hill and Peterson, 1992:694). Air has a $C_p = 1005$ J/kg-K for a temperature range of about 250 K to 340 K and a $C_p = 1026$ J/kg-K at 150 K. Carbon dioxide gas has a $C_p = 846$ J/kg-K at 300 K and a $C_p = 710$ J/kg-K at 175 K.

An important parameter when analyzing gas flows is the ratio of specific heats γ.

$$\gamma = \frac{C_p}{C_v} \qquad \qquad (5)$$

Assuming an ideal gas and combining the equation for mass specific enthalpy h and the specific heat equations another important relation can be developed which relates the specific heats to the gas constant. Mass specific enthalpy is defined as a function of mass specific internal energy e, pressure, and mass specific volume v.

7

$$h = e + Pv$$

$$C_v = \frac{de}{dT}$$

$$C_p = \frac{dh}{dT} \tag{6}$$

$$\therefore$$

$$C_p = C_v + R$$

Combining Eqn (5) and Eqn (6) the specific heat ratio can be expressed in an alternate form not dependent upon the specific heat at constant volume (Hill and Peterson, 1992:35).

$$\gamma = \frac{C_p \hat{m}}{C_p \hat{m} - \hat{R}} = \frac{C_p}{C_p - R} \tag{7}$$

For a gaseous mixture composed of many constituents, all of which are assumed thermally perfect, the following equations define the mixture properties where subscript i corresponds to different constituents of the gas mixture (Hill and Peterson, 1992:38).

$$\hat{m} = \frac{\sum \hat{m}_i m_i}{\sum m_i} = \frac{\sum \hat{m}_i m_i}{m} \tag{8}$$

$$C_p = \frac{\sum m_i C_{p_i}}{\sum m_i} = \frac{\sum m_i C_{p_i}}{m} \tag{9}$$

For air the gas constant $R = 8314.3/29 = 286.7\,\text{J/kg-K}$ and the specific heat ratio $\gamma = 1030/(1030 - 286.7) = 1.387$ at temperatures below 150 K, which can be

8

approximated as $\gamma = 1.4$. The constant pressure specific heat C_p of CO_2 is lower than air. For an air and carbon dioxide gaseous mixture Equations (7) through (9) allude that the introduction of CO_2 will effectively reduce the flow velocity at a given point. The magnitude of this reduction will depend on the percentage of the mixture that is CO_2; higher concentrations of CO_2 will result in lower local flow velocities. Qualitatively, as the mixture C_p decreases, γ will decrease, which as will be shown later results in a decrease in flow velocity for a constant Mach number because the speed of sound a is directly proportional to $\sqrt{\gamma}$.

2. 2. 2   Isentropic Flow.

Isentropic flow requires all flow processes be adiabatic (no heat transfer across system border) and reversible (no irrecoverable energy losses from system). This assumption holds true for uniform flows in the absence of transport gradients including viscous boundary layers, thermal diffusion layers and mass diffusion due to nonuniform molecular concentrations. Combining the first and second laws of thermodynamics for a reversible heating process yields Gibbs equation, relating the change in entropy s as follows

$$ s_2 - s_1 = C_p \ln \frac{T_2}{T_1} - R \ln \frac{P_2}{P_1} \tag{10} $$

9

If the isentropic flow of a perfect gas is considered Eqn (10) can be set equal to zero and the following isentropic relations can be derived employing the ideal gas law (Anderson, 2003:28-30)

$$\frac{P_2}{P_1} = \left(\frac{\rho_2}{\rho_1}\right)^{\gamma} = \left(\frac{T_2}{T_1}\right)^{\gamma/(\gamma-1)} \tag{11}$$

For steady one-dimensional (1-D) flow the mass, momentum and energy equations relating the flow properties at station 1 and station 2 along a streamline are given by

$$mass : \left(\rho U\right)_1 = \left(\rho U\right)_2 \tag{12}$$

$$momentum : \left(P + \rho U^2\right)_1 = \left(P + \rho U^2\right)_2 \tag{13}$$

$$energy : \left(h + \frac{U^2}{2}\right)_1 + q = \left(h + \frac{U^2}{2}\right)_2 \tag{14}$$

where q is the heat transferred per unit mass and U is the flow velocity in the variable direction (Anderson, 2003:72-73). Specializing further that the flow media is a perfect gas and the flow is adiabatic allows the energy equation to be combined with the enthalpy perfect gas equation of state $h = C_pT$ and rewritten as

$$\left(C_pT + \frac{U^2}{2}\right)_1 = \left(C_pT + \frac{U^2}{2}\right)_2 = C_pT_O = h_O \tag{15}$$

where the stagnation enthalpy h_o is constant everywhere in the absence of heat addition. With the mention of a stagnation property, it should be explicitly pointed out that the *stagnation*, or *total*, properties of a fluid are an edifice of energy conservation. A stagnation property is merely theoretical and represents the property obtained if a fluid were brought to rest isentropically. Examples of stagnation properties include stagnation density ρ_o, stagnation pressure P_o, and stagnation temperature T_o, and are identified with a subscript O.

Rewriting Eqn (15) in terms of Mach number and specific heat ratio yields a powerful equation relating the stagnation and static temperature of an adiabatic flow.

$$\frac{T_o}{T} = \left[1 + \frac{M^2(\gamma - 1)}{2} \right] \tag{16}$$

It is also important to note even though Eqn (16) was derived from the adiabatic energy equation for one dimensional flow it in fact holds for multidimensional flow simply by replacing the U with $\vec{V}$ because it is a general energy relation. Combining Eqn (16) with Eqn (11) yields two additional stagnation state relationships for any point in a compressible flow field (Anderson, 2003:78-81).

$$\frac{P_o}{P} = \left[1 + \frac{M^2(\gamma - 1)}{2} \right]^{\gamma/(\gamma-1)} \tag{17}$$

$$\frac{\rho_o}{\rho} = \left[1 + \frac{M^2(\gamma - 1)}{2} \right]^{1/(\gamma-1)} \tag{18}$$

Though these two equations utilized the isentropic relations, the flow itself need not be isentropic to employ them. However, if the flow is isentropic then the stagnation values will be constant throughout the flow field.

For quasi-one dimensional flow, such as that experienced in the free stream, isentropic nozzles and diffusers, the continuity equation yields a geometric relation to calculate the Mach number at any x-location in a converging-diverging (C-D) nozzle based on the ratio of flow area A available at a specified location to the flow area available at the throat A^* where $M^* = 1$

$$\frac{A}{A^*} = \frac{1}{M}\left[\frac{2}{\gamma+1}\left(1+\frac{M^2(\gamma-1)}{2}\right)\right]^{(\gamma+1)/2(\gamma-1)} \tag{19}$$

This equation can be solved to find $M = f(A, A^*, \gamma)$ but there is no simple analytic solution because the polynomial function is not whole numbered, as shown below in Eqn (20). However it is quite simple to solve the equation iteratively.

$$M^{2(\gamma-1)/(\gamma+1)}\left(\frac{A}{A^*}\right)^{2(\gamma-1)/(\gamma+1)} - M^2\left(\frac{\gamma-1}{\gamma+1}\right) - \left(\frac{2}{\gamma+1}\right) = 0 \tag{20}$$

The above equation makes a very important point; the local speed of a supersonic flow for a specified gas mixture (i.e. a specified γ) is *entirely* determined by the ratio of local flow area to throat area A/A^*. This equation includes an assumption that supersonic flow at the C-D nozzle exit has been obtained, which does in fact require a certain

12

pressure drop across the nozzle. This point will be discussed and explained further in section 2. 2.

The mass flow rate $\dot{m}$ of the flow media passing through a wind tunnel can be defined as $\dot{m} = \rho U A$. This can be rewritten as (Hill and Peterson, 1992:70-71)

$$\frac{\dot{m}}{A} = MP_O \sqrt{\frac{\gamma}{RT_O}} \left(1 + \frac{M^2(\gamma - 1)}{2} \right)^{(\gamma+1)/2(1-\gamma)} \tag{21}$$

at any point along the flow path when compressibility effects are considered, and can be specialized at the throat where the Mach number is known to be unity.

$$\frac{\dot{m}}{A^*} = P_O \sqrt{\frac{\gamma}{RT_O}} \left(\frac{(\gamma + 1)}{2} \right)^{(\gamma+1)/2(1-\gamma)} \tag{22}$$

Lastly, the local speed of sound of the main flow mixture is an important parameter associated with supersonic flow. The speed of sound is the velocity at which an infinitesimally weak pressure wave, or sound wave, travels through a medium. Since acoustic (sound) waves are defined as weak waves, changes in medium properties such as pressure, temperature and density across them are assumed to be infinitesimally small, thus quasi-equilibrium is maintained and entropy (system randomness) remains approximately constant. Additionally, the thermodynamic process across a sound wave happens so rapidly that no heat generated by compression within the fluid can escape. These two postulations of a reversible and adiabatic process allow the speed of sound to

13

be related to the isentropic compressibility of the medium. Furthermore, for a perfect gas the speed of sound can be succinctly written as (Anderson, 2003:74-77).

$$a = \sqrt{\gamma RT} = \sqrt{\frac{\gamma P}{\rho}} \tag{23}$$

2. 2. 3   *Shock Waves.*

When a flow media impinges upon an impermeable surface the local pressure momentarily rises due to a rapid increase in density. This local deviation in flow properties creates a pressure wave which attempts to equilibrate the system. In subsonic flow ($0 < M < 1$) sound waves can travel faster than the oncoming media which allows them to propagate infinitely upstream and downstream of a body blocking the flow. As noted before, sound waves are merely weak pressure differences translating through a fluid, bringing it into equilibrium. These acoustic waves broadcast the presence of a body and redirect oncoming atoms to a path of lesser resistance (lower pressure) around the body. Conversely, in supersonic flow ($1 < M$) sound waves can not travel upstream of a body blocking the flow because they are limited by the speed of sound which is less than the oncoming media velocity. Thus high-speed molecules are not forewarned and hit the body. Nature's solution to this problem is a shock wave which deflects the flow almost instantaneously. Shock waves are formed when an infinite number of sound waves pile up and coalesce into a single phenomenon. The presence of a shock wave preceding a body immersed in a super sonic flow is illustrated in Figure 1. An oblique shock wave, produced by a blockage with an inclined surface, is attached to the leading

14

edge of a 2-D wedge at zero angle of attack in Mach 2 air flow going left to right (Schlieren picture taken by Author at the W. R. Woolrich Laboratories, Aerospace Engineering Department, The University of Texas at Austin, 2005).

M = 2
α = 0°
shock wave
wedge
shock wave
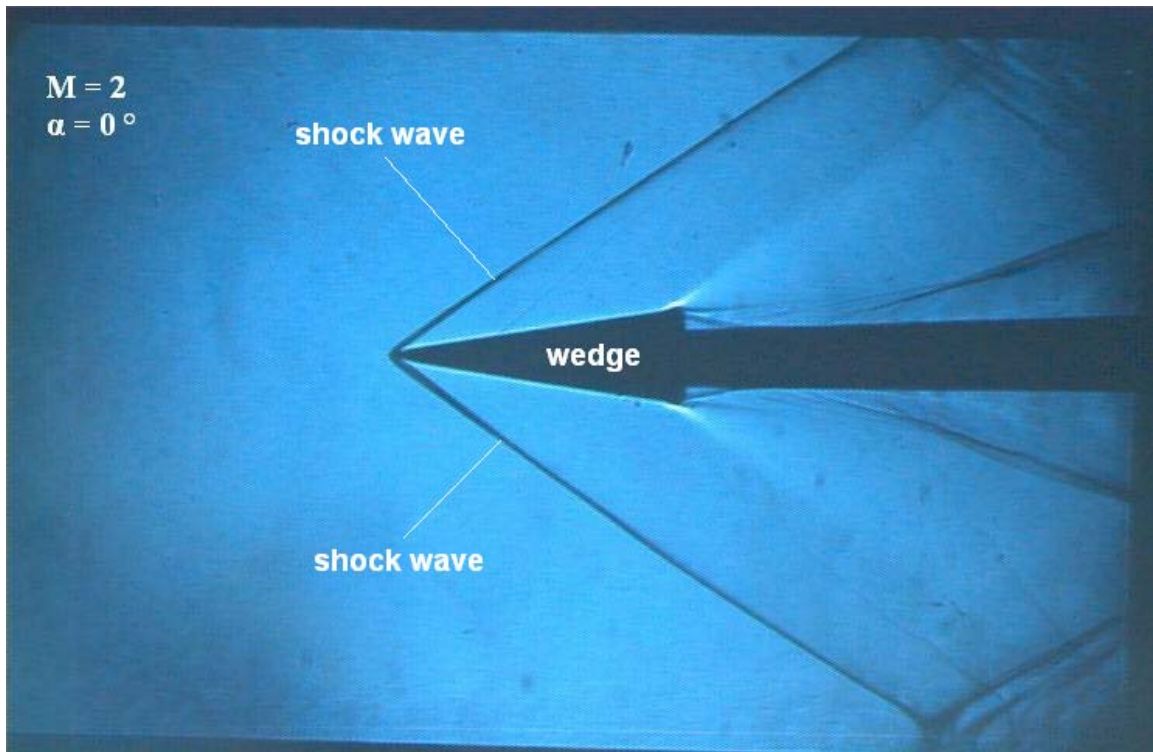
Figure 1:   A wedge immersed in supersonic air flowing left to right.

Flow properties change quickly and markedly across shock waves, which are quite thin (approximately 10^{-7}m thick) (Anderson, 2003:86). The magnitude of the change depends on the shock strength, which is determined by the free stream Mach number; higher freestream Mach numbers create stronger shock waves. In order to quantitatively determine the flow property variations across a shock, one can utilize the steady 1-D flow Equations (12), (13) and (14) by omitting the q term because the

process across a shock wave occurs so quickly it is assumed adiabatic (though definitely not isentropic due to large property gradients). From the manipulation of these equations the properties of a non-reacting perfect gas can be found both upstream and downstream of a normal shock wave, labeled subscript *1* and *2* respectively.

$$M_2^2 = \frac{1 + [(\gamma - 1)/2]M_1^2}{\gamma M_1^2 - (\gamma - 1)/2} \tag{24}$$

$$\frac{\rho_2}{\rho_1} = \frac{U_2}{U_1} = \frac{(\gamma + 1)M_1^2}{2 + (\gamma - 1)M_1^2} \tag{25}$$

$$\frac{P_2}{P_1} = 1 + \frac{2\gamma}{\gamma + 1}\left(M_1^2 - 1\right) \tag{26}$$

$$\frac{T_2}{T_1} = \frac{h_2}{h_1} = \frac{P_2}{P_1}\frac{\rho_1}{\rho_2} \tag{27}$$

$$T_{O1} = T_{O2} \qquad P_{O1} > P_{O2} \tag{28}$$

Notice all properties after the shock are known when the freestream flow parameters M_1 and γ are known a priori (Anderson, 2003:89-94). Equations (24) through (28) can also be interpreted to yield the property relations across a two dimensional (2-D) oblique shock wave. The primary difference for oblique shocks is only the freestream Mach number component normal to the shock wave M_{1n} is important in calculating the relative

shock strength. To use the above equations, merely replace M_1 with M_{1n} which can be found using Eqn (29).

$$M_{1n} = M \sin \beta \tag{29}$$

The downstream Mach number can be related using geometry where M_{2n} is the downstream Mach number component normal to the shock found from Eqn (24).

$$M_2 = \frac{M_{2n}}{\sin(\beta - \theta)} \tag{30}$$

The shock wave angle β is determined by the free stream Mach number M and the flow deflection angle θ caused by a 2-D surface, such as a wedge. This flow deflection angle, shock wave angle, Mach number dependence is called the $\theta - \beta - M$ relation (Anderson, 2003:135-136)

$$\tan \theta = 2 \cot \beta \left[\frac{M_1^2 \sin^2 \beta - 1}{M_1^2 (\gamma + \cos 2\beta) + 2} \right] \tag{31}$$

Similar closed form relations are not available for three-dimensional (3-D) surfaces, such as a cone because the third dimension introduces new complexities and nonlinearities which prevent analytical solutions similar to the $\theta - \beta - M$ relation. However, approximating the flow as inviscid allows an iterative technique developed by Taylor-

Maccoll to be employed to iteratively solve the flow field downstream of a conical shock (Anderson, 2003:370). Solutions for supersonic flow over a 3-D circular cone have been computed and found empirically. Graphical charts are available in technical reports such as NACA 1135 to determine the shockwave angle and surface properties caused by a given cone geometry and free stream conditions.

When a supersonic flow is turned away from itself a series of Mach waves are formed to isentropically adjust the flow to the downstream conditions. These waves fan out and termed Prandtl-Meyer expansion fans. Since the process is an expansion, the flow properties change opposite of those across a shock wave; the Mach number increases, temperature drops, etc. If the flow deflection angle θ is known the following equation relates the Mach number before and after the expansion fan to a Prandtl-Meyer function υ (Anderson, 2003:167-171). The Prandtl-Meyer function is tabulated in tables versus Mach number for easy reference.

$$\theta = \upsilon(M_2) - \upsilon(M_1) \tag{32}$$

2. 2   Wind Tunnels

A wind tunnel is an apparatus used to accelerate a fluid media (usually air) to a specified velocity. The media, or main flow, passes around a model, submersing the object of interest in a moving fluid. The fluid properties directly upstream of the test model should resemble the environment the actual product will experience during

operational application. This situational mockup allows researchers to measure flow effects (forces) on the test specimen. Test models are usually proportionally scaled down in size due to size limitations of most wind tunnel test sections, and therefore non-dimensional numbers describing the flow are recorded to relate the experimental results back to the full-scale structure operating at actual design conditions. The forces exerted on the model can be directly measured using load cells or calculated from pressure measurements directly measured, or, of more interest in this paper, inferred from velocity field measurements.

The fluid media typically used in wind tunnels is air. For supersonic wind tunnels, dry air is employed to prevent water condensate from forming as the air expands and the temperature drops along the wind tunnel path. A supersonic wind tunnel has a test section Mach number greater than unity ($M > 1$). The typical sections and components of a supersonic wind tunnel are shown in Figure 2.
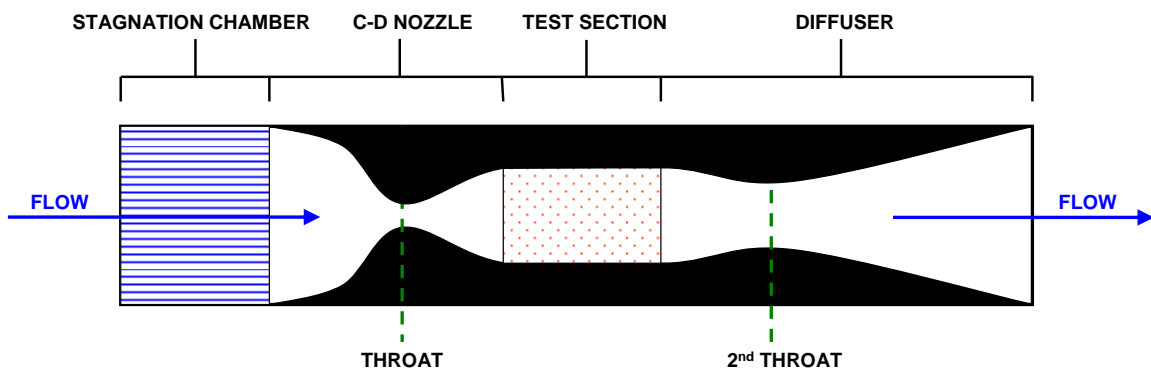
Figure 2:   Typical sections and components of a supersonic wind tunnel

The main flow is supplied to the stagnation chamber at a relatively low velocity and high static pressure; it is therefore a reasonable assumption to say that the stagnation

chamber (a.k.a. stilling chamber) properties represent the stagnation properties of the fluid. Flow straighteners are generally located within or directly upstream of the stagnation chamber to reduce the amount of rotation (vorticity) in the primary flow and create a uniform, collimated flow field. The stilling chamber feeds into the C-D nozzle. A rapidly converging nozzle portion is desired to thin out boundary layers and promote flow uniformity. The diverging nozzle portion should be designed using a geometric process such as the method of characteristics to prevent shock formation in the nozzle (Anderson, 2003:211). Creating a flow that replicates free-flight conditions accurately at the test section entrance (nozzle exit) is the ultimate goal. Across the test section the cross sectional area of the wind tunnel duct is kept constant so the flow is constant. Then, after the test section there is a choice of how the flow will be exhausted. The flow must eventually be brought to rest, and the more efficiently this is done, the better (i.e. lower operating cost, longer test run times and lower pressure ratios across the wind tunnel required to run).

To determine the pressure ratio across a wind tunnel required to run, define the following boundary conditions: (a) the flow must be stagnated at the entrance (b) the flow must be sonic at the nozzle throat and supersonic at the nozzle exit (c) the exhaust static pressure must equal the ambient static pressure at the wind tunnel exit. For a first approximation define the flow to be isentropic everywhere except across shock waves. When a wind tunnel is running there will be shock waves located in the test section; either weak Mach waves generated by surface imperfections along the test section wall, or a combination of oblique/bow shock waves generated by a test model. Regardless, a normal shock wave is the limiting case (worse case scenario). Assume a normal shock

wave is standing in the test section. Using the above boundary conditions and Figure 3 the following "pressure chain" can be used to determine the required pressure differential between the stagnation chamber and the diffuser exit for the wind tunnel to run (Anderson, 2003:220).

$$\frac{P_O}{P_E} = \left(\frac{P_O}{P_T}\right)_{M_T} \left(\frac{P_T}{P_2}\right)_{N.S.} \left(\frac{P_2}{P_{O2}}\right)_{M_2} \left(\frac{P_{O2}}{P_E}\right)_{M_E \approx 0} \tag{33}$$

The subscripts are T for test section properties, 2 for properties down stream of the normal shock and E for wind tunnel exit pressure, which will approximately equal the stagnation pressure downstream of the normal shock because the flow is decelerated significantly.
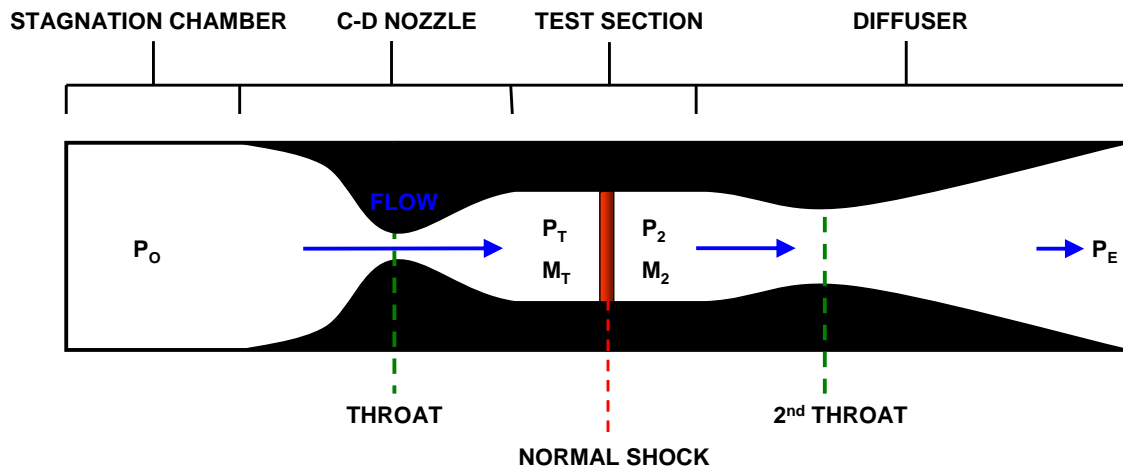
Figure 3:   Determining the required pressure ratio across a wind tunnel to run.

Realistically there will be a shock wave somewhere in the diffuser to increase the static pressure of the flow because ideal isentropic compression would require an impractically

large exit area. In order to reduce losses an extended second throat supersonic diffuser can be used to create a system of oblique shock waves to compress the flow instead of a single normal shock. Thus, when compared to a simple diverging diffuser, the advantage of a second throat diffuser is you can decelerate the flow before it enters the shock system described above. As discussed in section 2. 2. 3 the strength of a shock wave is determined by the incoming Mach number. Therefore the lower Mach number produced by the second throat will result in a weaker shock system in the supersonic diffuser and will increase the efficiency of the wind tunnel.

The second throat of the wind tunnel must be large enough to pass the mass flow of the system, which is constant throughout the wind tunnel. If the second throat is too small the upstream conditions will be forced to change. A shock wave will stand in the diverging part of the C-D nozzle and the wind tunnel will not start (reach it's design supersonic Mach number in the test section). Utilizing the conservation of mass, the perfect gas law, the normal shock relations and the isentropic relations, Eqn (34) can be derived. Equation (34) relates the throat ratio to the stagnation pressure ratio across the theoretical normal shock standing in the test section upon startup. The main flow media passing through the normal shock in the test section experiences a drop in stagnation pressure due to an increase in entropy (randomness). Thus, the flow becomes less organized and requires more duct area to pass the same amount of mass. Equation (34) illustrates the second throat area A_2^* required to start a two-throat supersonic wind tunnel must be larger than the nozzle throat area A_1^* because stagnation pressure always decreases across a shock wave (Anderson, 2003:223).

$$\frac{A_2^*}{A_1^*} = \frac{P_{O1}}{P_{O2}} \tag{34}$$

There are different categories of wind tunnels, based on the general setup. A blowdown wind tunnel is supplied with flow media from high-pressure tanks charged by compressors prior to each run. A pressure-vacuum wind tunnel employs both a high-pressure source at the stagnation chamber inlet and a low pressure chamber at the diffuser exit. A closed circuit wind tunnel takes the flow media discharged from the diffuser exit and feeds it back into the stagnation chamber after reconditioning it for reuse. Conversely, an open circuit wind tunnel uses flow matter only once.

For a pressure-vacuum wind tunnel system the lab operator has control over both the stagnation and exit pressures. If a maximum desired exit (vacuum) pressure is chosen, Eqn (33) can be used to calculate the required stagnation pressure required to run an empty wind tunnel at this pressure. However, if a test model is placed in the test section a higher pressure difference across the wind tunnel will be required to run the wind tunnel because the blockage will interrupt the starting shock wave which sweeps through the test section during start up.

2. 3 Particle Image Velocimetry

2. 4. 1 PIV Overview.

Particle image velocimetry is a laser diagnostic technique used to infer the 2-D planar velocity field of a moving fluid by measuring the instantaneous whole field velocity distribution of particles present in the flow (Scarano and van Oudheusden, 2003:3). Small tracer particles, or *seeds*, responsive enough to precisely track the fluid motion are introduced into the flow using various injection methods. At a point of interest along the flow path a thin plane of the seed field is photographed twice in rapid succession. From these two photographs, or image maps, the movement of the seed particles can be tracked and resolved into velocity vectors using Eqn (35) where D is the displacement of a particular seed particle between image one and image two (measured in pixels), t is the time elapsed between the two photographs and S is a scaling factor, which relates pixel displacements to actual distances traveled in the object reference frame (Mercer, 2003:71).

$$\bar{V} = \left(\frac{D}{t}\right)S \qquad\qquad (35)$$

The best pictures for use with PIV vector map correlations have high contrast between the seed particles and the image background; this is also known as a good *signal to noise ratio*. Thus photographs are generally taken in a dark environment (blackened room)

24

with the seeds being illuminated briefly by a planar stroboscopic light source. This technique produces a star field of white specs, which are the seeds, on a black image background. Figure 4 illustrates a generic PIV image pair.
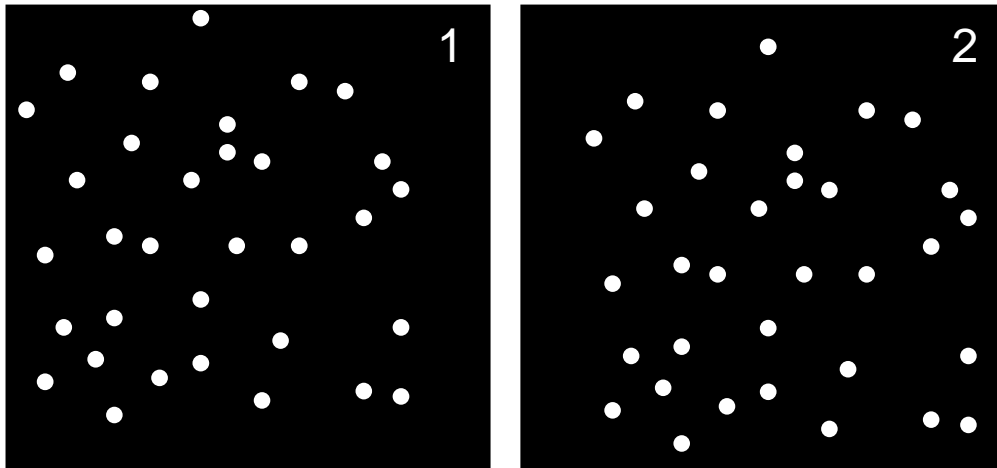
Figure 4:   High contrast PIV image pair.

A basic PIV setup consists of a fluid flow, a camera, a planar stroboscopic light source, a device used to deliver seeds into the flow and a computer synchronizes the whole PIV process and performs post-processing on the data collected. The planar light sheet slices through the fluid flow and is scattered by the seed particles. The camera lens is generally placed parallel to the planar light sheet to capture scattered light reflected from the seeds at 90°. Faster flows require shorter time separation between image pairs to keep a majority of the particles in both images. Small particles require high-energy light sources to generate reflections of sufficient intensity. Thus the best combination for high speed flow illumination and image capture is a pulsed dual laser and a frame

straddling charge coupled device (CCD) digital camera. Figure 5 is a simple schematic

showing the basic components of a PIV system used for high-speed flow inspection.
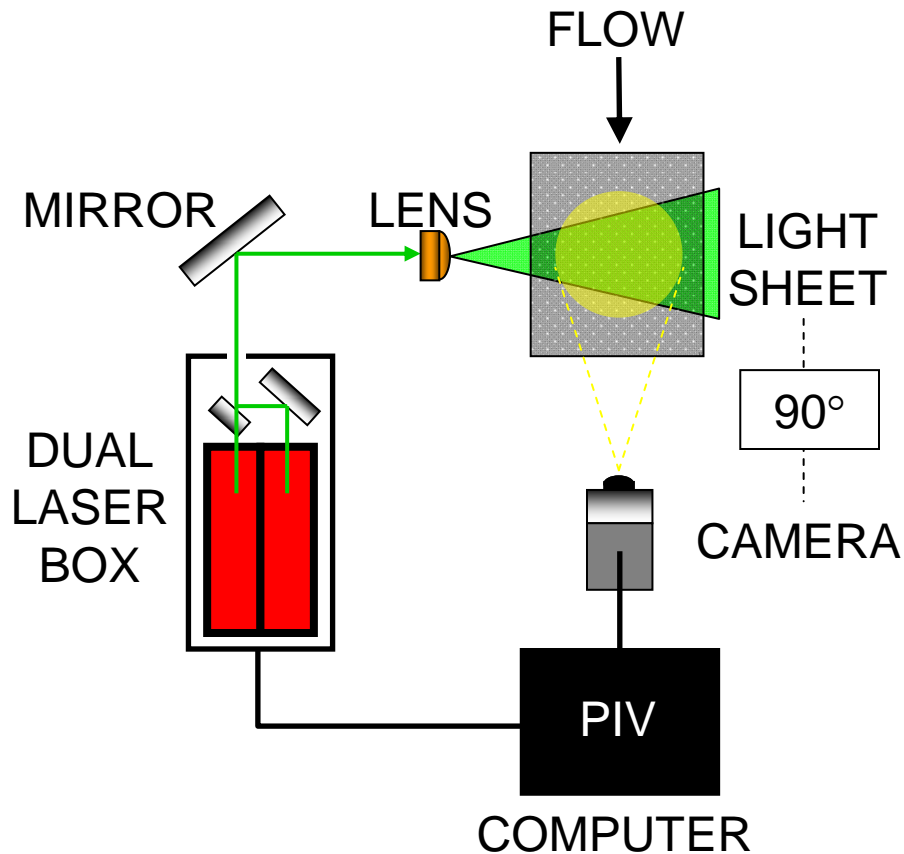
Figure 5:   Basic PIV setup for high speed flow inspection.

2. 4. 2   Seed Particles.

It is important to emphasize the vector maps calculated using the PIV technique

are representative of the particle motion, and not necessarily the fluid motion directly. It

is therefore advantageous to pick a seed material with properties conducive to tracking

the fluid motion as accurately as possible. Though there are many factors determining a

tracer particle's ability to follow the gas flow surrounding it, two characteristics having

the strongest influence are size and density. Both of these factors contribute directly to the particle relaxation time, which is a measure of the particle's ability to attain velocity equilibrium with a surrounding fluid (DeLapp, 2006:13). The atom or molecule can be thought of as the lower limit on particle size. Since a gas is composed of molecules, tracer particles the same order of magnitude as the flowing gas molecules would track the motion of the gas exactly. However, what good would that be? The whole point of introducing seed particles is because they are large enough to visualize. Thus, the classic dilemma is choosing good PIV seed particles small enough to accurately follow the velocity gradients of a moving fluid, but large enough to scatter sufficient light for photo recognition (Sambroske, 1993:3).

Based on the Mie solution to Maxwell's equations for the scattering of electromagnetic energy by spherical particles, Mie scattering is dominant when light incident on a particle has a wavelength λ smaller then the particle diameter d ($\lambda < d$). Conversely, elastic Rayleigh scattering is dominant when light scattered through a medium has a wavelength that is larger than the particle diameter ($\lambda > d$). Rayleigh scattering does not provide a signal to noise ratio high enough for PIV application; Rayleigh scattering provides a fog of illumination instead of discrete, high contrast particles. Melling commented, "Rayleigh scattering is far too weak for PIV, even with illumination by a laser of maximum available power or pulse energy" (Melling, 1997:1407). Additionally, the energy deficit is even higher because the original energy contained in a laser beam is diminished when it is fanned out into a thin sheet.

Two quantitative parameters that provide a good measure of a particle's ability to scatter light is the size factor F relating the ratio of particle diameter d to incident light

wavelength λ and the index of refraction n which portrays how the local speed of light c is dependent upon the material it is traveling through.

$$
\begin{aligned}
F &= d/\lambda \\
n &= c_{vac}/c
\end{aligned}
\tag{36}
$$

The intensity of light scattered perpendicularly from a particle is a strong function of both parameters above; nominal values for particles used in gas flow PIV are $F = 10^{-1} - 10^{-3}$ and $n \geq 1.4$ (Melling, 1997:1406-1407).

For a specified particle material density, larger seeds are more massive neglecting porous packing effects. Larger seeds have more inertia and respond slower to changes in fluid velocity, which is undesirable, especially in turbulent flows. One method used to quantify particle response is the relaxation time, or relaxation distance, required for the particle velocity to recover, or catch up, to the fluid velocity after experiencing a gradient. Shock waves represent the largest velocity gradients present within a flow, thus measuring the relaxation required after passing through a shock wave is a useful way of measuring particle responsiveness. Application of this method and the theoretical equations behind it are given by Melling (1997) and Scarano and van Oudheusden (2003). The final result of the analysis contained in these references is only particles less than 1 µm in diameter respond fast enough to accurately track high velocity gradients such as flow through shock waves and vortex flow.

Particles used to seed gaseous flows are generally one of two main types, atomized liquids or solid based powders. Both particle types have ample heritage in the

28

PIV community and have been employed numerous times. Liquid particles are formed by atomization and there are many injectors currently in use. Liquid based seeds are good because they can be injected at steady rates and naturally form into spherical particles due to surface tension effects. Solid particles are advantageous when high temperatures are expected or high particle concentrations are required, such as with combustion flows or high velocity flows. Desirable traits for any generic seed particles include: (1) large scattering cross section (2) low mass density (3) non-toxic, non-contaminating and chemically inert (4) reasonably priced and readily available. Desirable traits for associated particle injection systems include: (1) selectable particle size (2) controllable particle production rate (3) monodispersed particle size distribution (Crosswy, 1985). Typical particles used for gaseous flows are presented in Table 1 (Melling, 1997; Mercer, 2003).

Table 1: A small sample of seeds previously employed in gas flows PIV

Material	Specific Gravity	d [μm]	n
TiO_2	3.5	<1	2.6
Al_2O_3	3.97	0.3-3	1.76
Smoke	1	1	1.3
Olive Oil	0.97	1.06	1.3

Unfortunately, both classes of particles have inherent draw backs, as mentioned in Chapter 1. Both have a tendency to build up on surfaces, distorting or refracting light passing through transparent walls, or interfering with simultaneous measurement

techniques such as pressure sensitive paint (PSP) or temperature sensitive paint (TSP) (Melling, 1997:1412). Abrasion due to particle blasting and accumulation can also have adverse effects on wind tunnel or experiment hardware such as electronics, screens, and any moving parts. This becomes especially true in closed circuit wind tunnels where the seeds must repeatedly travel through the main media conditioning system. These concerns eventually imposed monetary and scheduling setbacks for researchers due to required cleaning of the wind tunnel and equipment. Lastly, health concerns are an important consideration when rating seed candidates on utility and handling. PIV seed particles are generally fine powders or atomized sprays which increases their potential to be hazardous to lab operators. Due to extremely small particle sizes, particles useful in PIV often pose an inhalation hazard. Even though any risk can be substantially mitigated through proper planning and safe operational procedures, it would be better if this was not an issue; thus particles that do not linger on surfaces and equipment are clearly superior in regards to safety (Brown, 1985).

2. 4. 3   Illumination Source.

There are clear-cut requirements for PIV illumination. For application in high-speed flows, these requirements are even more restrictive due to high velocities and associated short time scales. The primary role of PIV illumination equipment is to reveal the seed particles traveling along with the flow. Particles traveling through the illumination plane need to appear frozen during each light pulse to prevent photographic blurring. Thus, fast flows require short light pulse durations. Next, accurate PIV correlations require two images taken in rapid succession. The time delay between two

successive particle field images will determine the apparent distance traveled by the particles. Again, for faster flows the time delay must be decreased to keep particle translations within certain limits based on camera and software capability, as will be discussed later. These two restraints have driven the PIV research community to employ pulsed lasers, for good reason. Not only can pulsed lasers satisfy the two time requirements mentioned above, they also have many other favorable qualities for application with high speed flow PIV. Modern lasers provide a steady source of approximately monochromatic, collimated, high energy light. Off-the-shelf laser systems built with two laser heads are user friendly and very adjustable to provide excellent PIV illumination for a myriad of experimental setups. The laser most widely used for PIV is the frequency doubled neodymium yittrium aluminum garnett (Nd:YAG) due to its high energy (up to 400 mJ/pulse), short pulse duration (<10 ns) and short 532 nm wavelength emission (Mercer, 2003:72).

High light energy is important because the initially circular laser beam cross section is flattened and spread out into a diverging or collimated light sheet for planar illumination. This reduces the light intensity incident on the seed particles and thus the intensity of any scattered light. In order to retain a high energy density the light sheet should be as thin as possible. However, if high out of plane velocities are expected, a thicker light sheet helps prevent particle drop out (loss of particles between image one and two) and increases correlation accuracy (Mercer, 2003:73). The light sheet should span the entire camera field of view to maximize the amount of image area available for processing. Mercer (Mercer, 2003) presents basic illustrations and equations for

modeling cylindrical lens used to form laser light sheets; both collimated light sheet and diverging light sheet profiles are analyzed.

2. 4. 4   *Image Capture Device.*

Requirements for high speed PIV image capture devices, or cameras, are driven by the same demands as the illumination system, and in fact these two systems are closely coupled.   A single camera synchronized with the laser pulses from the illumination system must capture two images in rapid succession. The introduction of frame straddling charge couple device (CCD) digital cameras dramatically increased the capability of PIV systems. An alternating array of photosensitive pixels and storage cells is used to capture two images with a very short time separation, or transfer time, between frames. The two laser pulses are generally set to fire at the end of the first image exposure, or integration time, and at the beginning of the second image exposure (Mercer, 2003:80).

Cameras used for PIV are often combined with a high performance optical lens and filters to ensure optimal collection of scattered light and to enhance the signal to noise ratio of the desired wavelength. The camera lens is focused on the illumination plane and the f-stop is generally set small, leaving the camera aperture as open as possible. This admits plenty of scattered light into the lens. Filters blocking all wavelengths but that of the laser are useful in attenuating background light which can cause over exposure and noise. Another application of filters is to reduce the intensity of the scattered light captured by the camera when there is no desire to change the f-stop.

This may be required when overexposure, or pixel saturation, occurs because the camera is placed close to the test location to achieve optimal spatial resolution.

The two images captured on the CCD pixel array are much smaller than the actual objects photographed. A scale factor S is required to relate the image, sized in pixels, to the actual object, sized in length units.

$$S = \frac{object}{image} = \frac{length}{pixel} \tag{37}$$

It is important to obtain a correct scale factor when focusing the camera on the inspection plane (light sheet plane) prior to sealing up the wind tunnel for a test. If the scale factor is inaccurate, all of the velocities obtained during post-processing will be incorrect.

2. 4. 5   *PIV Post Processing.*

After a test run is complete, the data (image pairs) collected should be evaluated for PIV usability. Any image pair can be processed using PIV software but only those exhibiting the desired traits described in the preceding sections (high contrast, discrete particles, uniform particle distribution, minimal overexposure, etc.) will yield quality results.

Each image pair is compared using advanced mathematical correlations based on the simple formula given by Eqn (35). Each image, also know as an *image map*, is divided into a grid of interrogation regions (IR) which are generally squares ranging from 16x16 to 256x256 pixels. Figure 6 is an example of two image maps (IM) divided up

into $16^2 = 256$ interrogation regions, each one being 128 x 128 pixels. A single averaged particle velocity vector is calculated for each IR based on the gross particle movements from frame 1 to frame 2. The Fast Fourier Transform (FFT) is used to convert each IR pair (the same IR from frame 1 and frame 2) into two signals in the frequency domain. Then the statistical technique of spatial cross-correlation is applied to both signals from IR 1 and IR 2 to determine a spatial shift function. This spatial shift function is the missing key, validating the solution (image two) based on the input (image one).
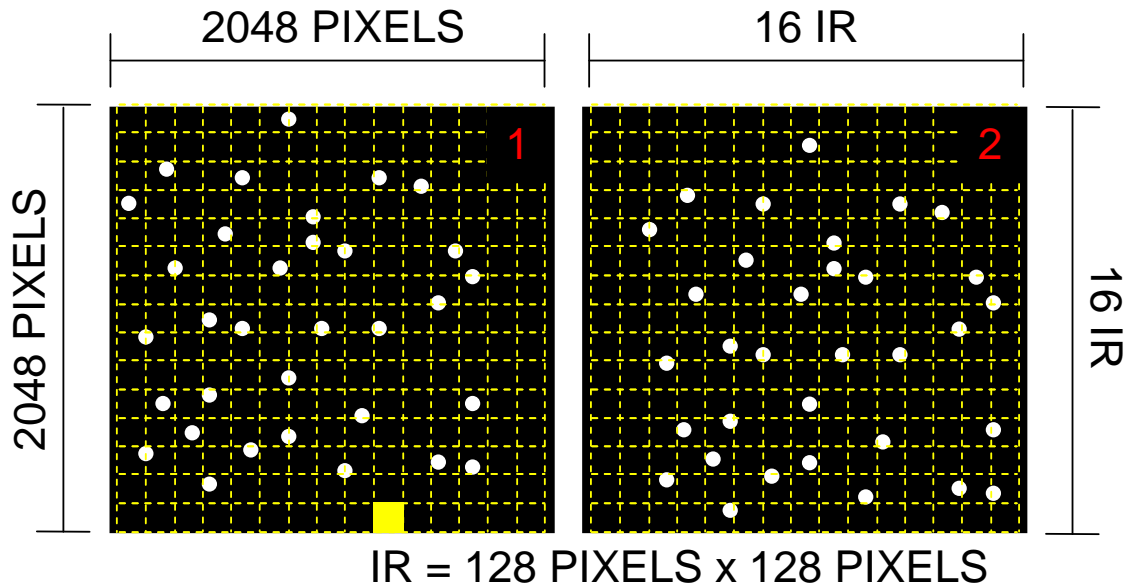
Figure 6:   Image map pair divided into interrogation regions for processing.

High (true) cross-correlation signal *peaks* appear when numerous particles from IR 1 match up with their spatial shifted equivalents in IR 2, and small (false) signal peaks appear when individual particles from IR 1 match up with different particles in IR 2. The overall highest peak (or signal) in the frequency domain is directly related back to the

average particle displacement occurring in the IR from frame 1 to frame 2. Unfortunately particles leaving the IR from frame 1 to frame 2 cannot contribute to true signal peaks because they are missing from one of the two signals. Instead, they decrease the signal to noise ratio equating to less accuracy. This is known as *signal drop out* and can be avoided by choosing IR sizes large enough to ensure a majority of the particles are present in both IR frames. Based off the Nyquist sampling criterion the maximum particle displacement should be 25% of the IR to prevent signal drop out (Dantec, 2002:4-6 to 4-8). This can be related to a maximum desired particle translation in the object plane using Eqn (38) where N is the dimension of the square IR measured in pixels and D_{MAX} is the desired maximum particle displacement.

$$D_{MAX} = \left(\frac{N}{4}\right)S \tag{38}$$

In fact, the above equation lends itself nicely for a first approximation for any one of the three variables. For example, if a known IR dimension is desired and the average particle displacement for a given flow can be estimated, then an appropriate scale factor can be calculated. This can be used to determine a suitable camera distance from the object plane of inspection.

Another way of accounting for signal drop out is to use IR overlapping, which is specified by a percentage of the IR to be overlapped with its neighbors. This is effectively a search for particles translated out of their original IR and traveled to an adjacent IR in frame 2. The higher the overlap percentage the longer the correlation

process will take. Overlapping also produces more vectors because more effective interrogation regions are created.

There are three correlation styles based on the cross-correlation technique that provide velocity vector maps of varying accuracy. The first style is simply the technique described above where the IR grid is a mesh with constant divisions. The second style is slightly different but more accurate. Adaptive correlation uses the same technique described above but the IR grid is not necessarily constant with respect to IR dimension or shape. An initial IR size is chosen, a final IR size is chosen, and deforming interrogation regions (variable aspect ratio) can be utilized if desired. The cross-correlation technique is then applied multiple times to a specific image pair and feedback is used to determine which areas of the image provide good signal peaks. These high peak areas are zeroed in on and the best IR shape is selected to obtain the most accurate vector. Unfortunately the adaptive technique significantly increases the processing time of an image pair, taking approximately five times longer. The final correlation style is the average correlation. This style combines multiple raw IM pairs into one IM pair and then employs the original cross-correlation technique (constant IR grid) to produce one vector map.

Each correlation style produces a raw vector map consisting of (generally) thousands of velocity vectors (one for each IR). For flows with good seeding characteristics (high monodispersed distribution density), the vectors will most likely be consistent and connect continuously across the image. However, *spurious* vectors (false; erroneous) will be created for regions of the IM that have sparse seeding due to the forced solution characteristic of FFT analysis. These vector groupings will appear as noise; a

scramble of vectors pointing in many directions. Vector validation methods are employed to alleviate this problem. A moving average technique compares each vector to its neighboring counterparts. If the vector being scrutinized is found to be grossly inconsistent with its surroundings it is replaced by an average. This technique may be tailored for different levels of confidence by changing the level of acceptance, the size of the averaging area, and the number of times the raw vector map is processed. The next validation is more direct and consists of placing boundary constraints on certain vector values such as length (velocity magnitude). This technique should be sparingly used to prevent accidental corruption of the information conveyed by each vector map.

2. 4   Carbon Dioxide

Carbon dioxide (CO_2) is a natural component of the atmosphere and it plays an important role in several diverse applications including beverage carbonation, rising agent in bakers yeast, rapid actuation systems, fire extinguishers, and frozen food transportation (Toromont Process Systems). Industrial carbon dioxide is generally stored as a liquefied compressed gas in large metal tanks at approximately 853 psia or 57 atm. However, the pressure of the storage tank is also dependent on the local ambient temperature, causing the pressure to rise in warmer environments (Wittemann). Owing to its many uses and applications CO_2 is extremely common and inexpensive to purchase. Unfortunately carbon dioxide is colorless, nearly odorless and it displaces air, making it a

health risk in non-ventilated areas. Properties of CO_2 relevant to this research are presented in Table 2 with the complete chart from Wittemann available in Appendix A.

Table 2: CO_2 properties relevant to this research.

PROPERTY	VALUE	UNITS	Conditions
Molecular Weight	44.001	kg/kg-mol	-
Solid Density	1562	kg/m3	Sublimation point
Liquid Density	1177	kg/m3	Triple Point
Gaseous Density	1.833	kg/m3	STP (P=1 atm, T=295 K)
Liquid C_p	1840	J/kg-K	220 K
Gaseous C_p	700-850	J/kg-K	175-300 K
Gaseous Gamma (γ)	1.294	-	STP
Sublimation Temperature	195	K	1 atm = 1.01325E5 Pa
Triple Point	216	K	5.11 atm
Heat of Vaporization	234500	J/kg	273 K
Heat of Fusion	571300	J/kg	Triple Point
Heat of Sublimation	199000	J/kg	195 K
Vapor Pressure	830	psig	STP
Liquid Viscosity	1.19E-04	kg/m-s	256 K
Solid Index of Refraction	1.4	-	-
Gaseous Index of Refraction	1.000449	-	-

2. 5 CO_2 Piping Effects

Compressed carbon dioxide stored in metal tanks exists in both liquid and gas phases. The top free surface of the liquid CO_2 vaporizes creating gaseous CO_2. The evaporation continues until adequate pressure has been reached at the liquid/gas interface to maintain a liquid state for the remainder of the CO_2 below, as illustrated in Figure 7. The liquid is extracted using a full-length eductor tube reaching all the way to the bottom

of the tank, out through which the liquid is forced by the high-pressure gas (Air Products, 2004).
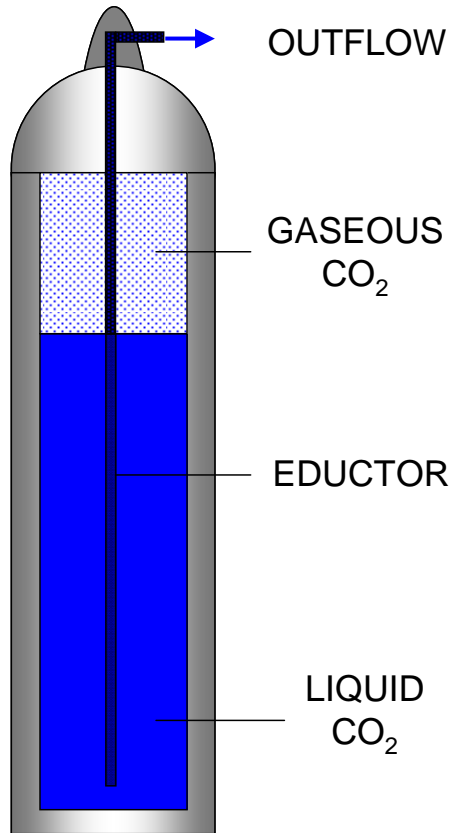
Figure 7: **Industrial steel storage tank containing compressed CO_2.**

Pressure drops will occur when transporting the liquefied CO_2 from the storage tank to the wind tunnel injection locations due to many different mechanisms, but primarily resulting from viscous resistance. These pressure drops should be understood if the phase and flow properties of the injector are to be predicted. Flow through pipes is based on both theoretical and empirical correlations due to varying values of pipe surface roughness associated with different materials and manufacturing processes. Substantial

research and testing has been done to characterize pipe flow. Specific values for particular pipes, valves and fittings are tabulated in technical reports available for reference.

The first step in characterizing pipe flow is to determine pertinent fluid properties, flow characteristics and pipe dimensions. Important values include liquid density ρ, liquid viscosity μ, average pipe flow velocity $\vec{V}$, pipe inner diameter ID and pipe length L. Most liquids are considered incompressible (note for clarification that *fluid* refers to both liquid and gas, but *liquid* does not encompass gases). The average pipe velocity can be calculated for an incompressible liquid using conservation of mass shown by Eqn (39).

$$\dot{m} = \rho A \left| \vec{V} \right|$$
$$\therefore$$
$$\left| \vec{V} \right| = \frac{\dot{m}}{\rho A}$$
(39)

The CO_2 mass flow rate $\dot{m}$ is assumed constant for the entire piping line. If a single line is split into two branches then the mass flow rate of each individual branch must be found and used to find the individual branch velocities.

Once the average pipe velocity is known the flow state (laminar, unstable or turbulent) can be predicted using the diameter-based Reynolds number for a pipe given by Eqn (40). Pipe flow conditions are laminar when $\text{Re} < 2000$, unstable when $2000 < \text{Re} < 4000$ and fully turbulent when $\text{Re} > 4000$ (Crane, 1988:1-4).

$$\text{Re} = \frac{\rho ID \left| \vec{V} \right|}{\mu}$$
(40)

40

Daniel Bernoulli's insight led the derivation of Eqn (41) which relates conservation of energy for an incompressible fluid flowing between two points under the influence of a conservative field (gravity). The total energy, or *head H*, is considered constant for a flow free from friction, heating, blockages and non-conservative fields. The individual terms are elevation head Z, pressure head $P/\rho g$ and velocity head $\vec{V}^2/2g$ where g is the gravitational constant.

$$Z + \frac{P}{\rho g} + \frac{\vec{V}^2}{2g} = H \tag{41}$$

In reality, there are pressure drops during pipe flow due to pipe friction, changes in flow direction, obstructions and changes in pipe cross section (Crane, 1988:2-8). These can be accounted for by including a static pressure head loss term h_L .as shown in Eqn (42)

$$Z_1 + \frac{P_1}{\rho g} + \frac{\vec{V}_1^2}{2g} = Z_2 + \frac{P_2}{\rho g} + \frac{\vec{V}_2^2}{2g} + h_L \tag{42}$$

The general equation derived for a pressure drop through a circular pipe, applicable to any incompressible fluid whether laminar or turbulent, is the Darcy formula presented as Eqn (43). The Darcy friction factor f is empirically correlated and is dependent upon the particular pipe geometry (ID and surface roughness) and flow conditions (Reynolds number).

41

$$h_L = \left(f \frac{L}{ID} \right) \frac{\bar{V}^2}{2g} \qquad \textbf{(43)}$$

Substituting Eqn (43) into Eqn (42) and setting all elevation head and velocity head terms to zero the pressure drop ΔP caused by frictional losses present during pipe flow is given by Eqn (44) (Crane, 1988:1-5 to 1-6).

$$\Delta P = \left(f \frac{L}{ID} \right) \frac{\rho \bar{V}^2}{2} \qquad \textbf{(44)}$$

Flow fluctuations caused by fittings and valves also contribute significant pressure drops. In order to relate these pressure losses to the local pipe branch a resistance factor K is substituted into the above equation.

$$K = \left(f \frac{L}{ID} \right) \qquad \textbf{(45)}$$

The resistance coefficient K relates a particular fitting or valve pressure loss to an equivalent pipe length required to obtain the same energy state. The result is a total piping line resistance $K_T = \sum K$ can be computed and then substituted into Eqn (44) to determine the total pressure drop across a pipe branch (Crane, 1988:2-8). However, a change in pipe cross sectional area will cause the flow velocity to change for a given mass flow rate. If the piping system employs pipes with different ID then the resistance

factors must be related back to a single set of flow conditions to employ the additive property of K_T. All of the resistance factors must be related back to an original reference pipe using Eqn (46) where $\phi = ID_{CURRENT}/ID_{REF}$.

$$K_{ref} = \frac{K}{\phi^4} \tag{46}$$

The local resistance coefficients for the different pipe fittings shown in Figure 8 can be calculated using the equations in Table 3 where $\varepsilon = ID_{SMALL}/ID_{LARGE}$, n_{90} is the number of 90° bends in the pipe section, K_{90} is the resistance of one 90° bend (which is a function of ID and bend radius r) and ℓ is the number of coils in local piping (Crane, 1988). A chart from Crane used to find K_{90} for pipe bends is presented in Appendix B.

Table 3:   Local resistance coefficients for different pipe fittings.

	FITTING	EQUATION
A	Straight Pipe	$K = f\dfrac{L}{ID}$
B	Sudden Contraction	$K = \dfrac{0.5\left(1 - \varepsilon^2\right)}{\varepsilon^4}$
C	Sudden Enlargement	$K = \left(1 - \varepsilon^2\right)^2$
D	90° Elbow Bend	$K_B = (n-1)\left(0.25\,f\pi\dfrac{r}{ID} + 0.5\,K_{90}\right) + K_{90}$
E	Circular Loop	$K_C = (4\ell-1)\left(0.25\,f\pi\dfrac{r}{ID} + 0.5\,K_{90}\right) + K_{90}$
F	Through Branch of "T"	$K = 20\,f$
G	90° Connection of "T"	$K = 60\,f$
H	Pipe Exit	$K = 1$
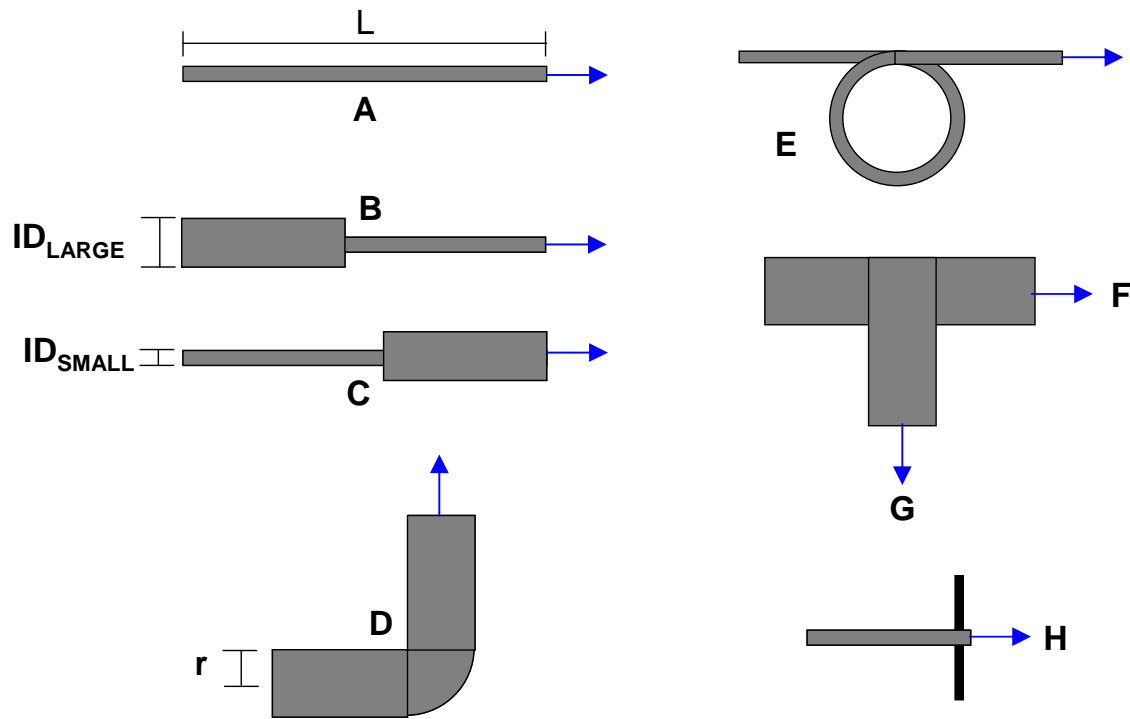
Figure 8: Schematic of different pipe fittings.

A CO_2 mass flow rate $\dot{m} = 0.00136$ kg/s was measured during wind tunnel injection using a single shroud injector at the C-D nozzle. This value can be used to find approximate flow velocities, Reynolds numbers, friction factors, and ultimately resistance values for each section of piping. The Darcy friction factor can be approximated for laminar pipe flow using Eqn (47).

$$f = \frac{64}{Re} \tag{47}$$

If the flow is unstable and transitioning to a turbulent state, the friction factor is indeterminate but will be bounded by the laminar and turbulent f values. For turbulent

pipe flow the friction factor depends on both the Reynolds number and the roughness of the pipe wall (Crane, 1988:1-6). The friction factor is directly proportional to surface roughness and inversely proportional to pipe diameter. In fact, for a given mass flow rate and an assumed fixed friction factor the pressure drop per foot of pipe varies inversely with the fifth power of the pipe diameter (Crane, 1988:1-7). Friction factors as a function of Reynolds number and relative surface roughness (Moody Plots) are presented from Crane in Appendix C.

2. 6 CO_2 Particles

A phase diagram highlighting the phase characteristics and associated properties of carbon dioxide is shown in Figure 9. Carbon dioxide cannot exist as a liquid when the local pressure is less than 5.1 atmospheres, no matter the temperature. It is this property that that makes CO_2 a candidate for clean seeding PIV and which initiates the formation of solid CO_2, also know as dry ice. Dry ice is formed when liquid CO_2 is suddenly exposed to a low-pressure environment causing the top layer of liquid to rapidly evaporate, or *flash*. This evaporation is an endothermic process, where heat energy is absorbed by the gasifying top layer of CO_2 and the surrounding liquid material is rapidly cooled causing it to solidify. After CO_2 has formed into dry ice it will immediately begin to sublimate (gasify from a solid) without becoming liquid, as long as the pressure is kept below 5.1 atm. This flashing process is commonly employed to quickly freeze perishable goods in order to retain high food quality. To do this carbon dioxide is flashed through a

nozzle or orifice creating an approximately 50% snow 50% vapor mixture with properties $T = 195\,\text{K}$ and $P = 1\,\text{atm}$ (Toromont Process Systems).
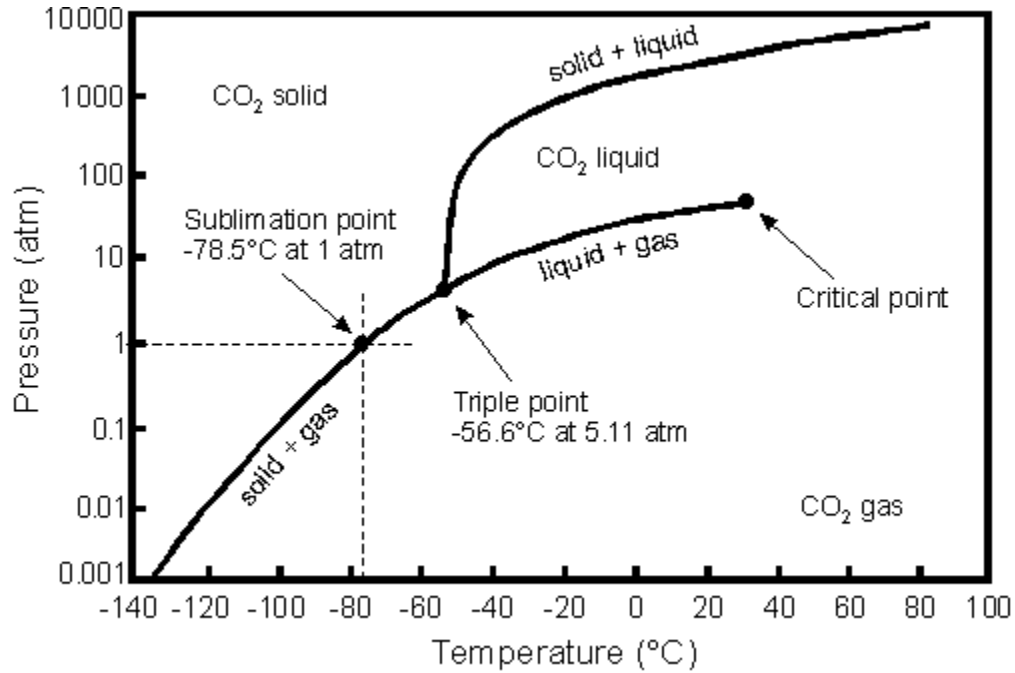
Figure 9:   Carbon dioxide phase diagram.

A similar process can be employed to make CO_2 seed particles for use with PIV. A two-phase snow and gas mixture can be created by flashing high pressure liquid carbon dioxide through an orifice. Furthermore, the findings of DeLapp et al (DeLapp, Reeder, Crafton, 2006) that carbon dioxide particle agglomeration, or clustering, became prevalent in environments with high CO_2 concentrations was utilized by McNiel to design the *shroud injector* (McNiel, 2007). The shroud injector operates in two steps. First a small inner diameter (ID) *feed tube* atomizes liquid CO_2 inside a *shroud tube* which has a significantly larger ID. While ejected into the shroud tube the liquid CO_2,

47

now in an environment at pressures above that required to maintain purely liquid CO_2, is rapidly cooled by evaporation and solid CO_2 particles are formed. Then, as the particle/vapor mixture translates toward the shroud tube exit particle sizes are believed to increase due to agglomeration rates being larger than sublimation rates. This creates porous accumulations resembling snow flakes. Some evidence of this observation is given by DeLapp (DeLapp, 2006). The shroud injector process is illustrated in Figure 10.
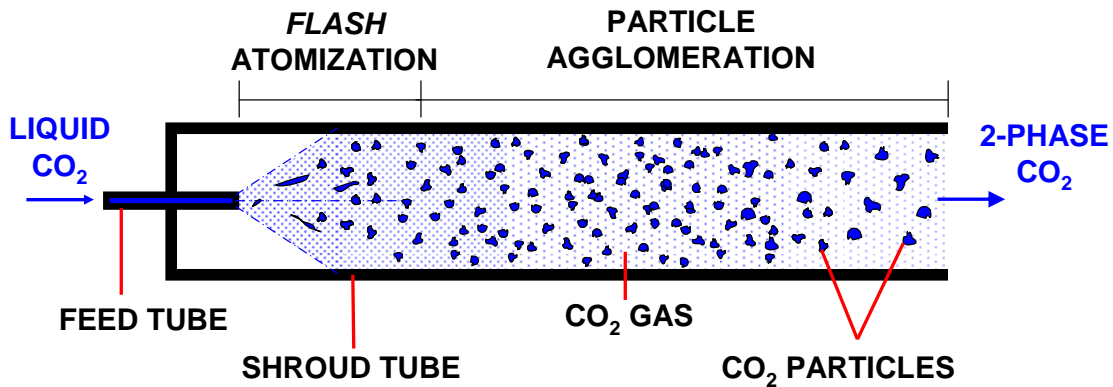
Figure 10: Predicted phase and flow of CO_2 within shroud injector.

To understand the changing environment surrounding the CO_2 particles while they flow through the C-D nozzle and test section, the carbon dioxide phase diagram was marked at three locations of interest: the nozzle injection point, the nozzle throat and the test section entrance, as shown in Figure 11. Then an estimated curve fit line of temperature and pressure intersections was drawn to visualize the changing environment effects on rates of sublimation or deposition. The dry ice pellets would sublime faster as the point of temperature/pressure intersection moved further right of the *solid + gas* two-phase line. Conversely, the dry ice particles would stop sublimating as the

48

temperature/pressure intersection point moved left of the *solid + gas* two-phase line. This is based on the findings of Kochtubajda and Lozowski who concluded "the ambient temperature was found to have the largest effect on the sublimation rate of dry ice pellets…warmer environments accelerated the process" (Kochtubajda and Lozowski, 1985:604).
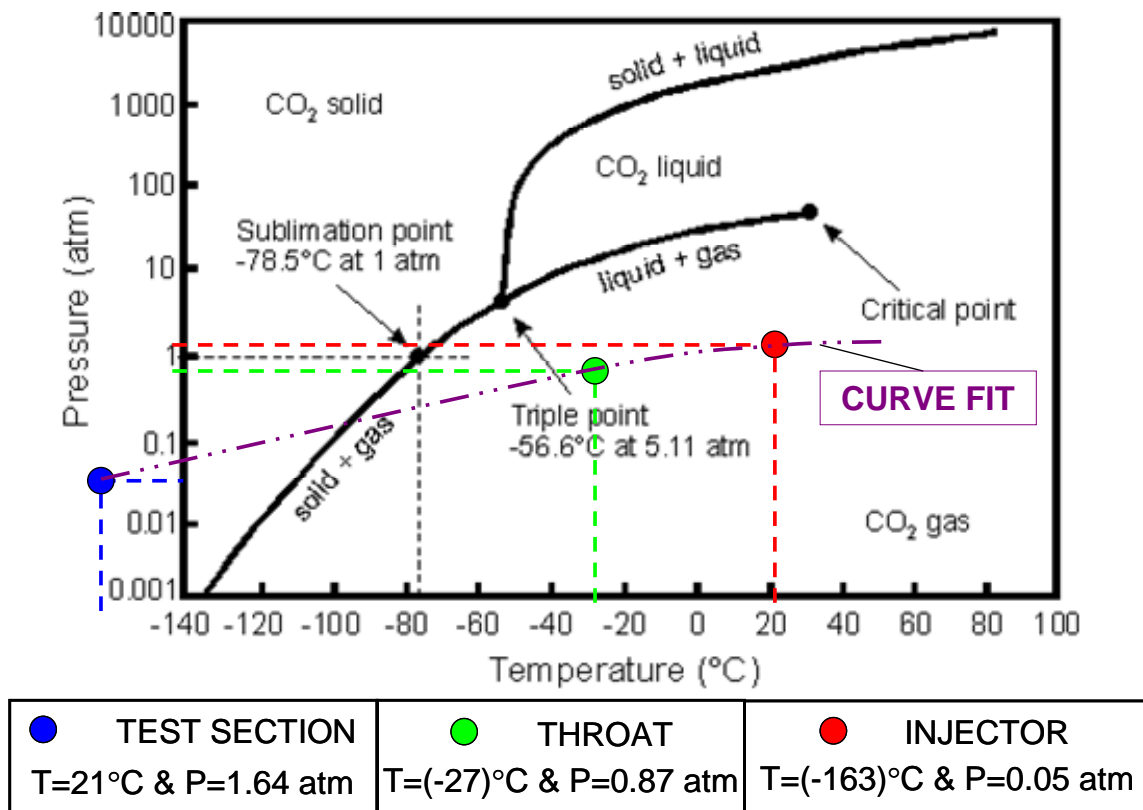
Figure 11: Flow media cooling effects on CO2 particle sublimation rates.

Lastly the potential mixture effects of gaseous CO_2 reducing the effective flow velocity in the test section will be evaluated. Gaseous carbon dioxide has a lower specific heat value than air, and therefore the mixture specific heat is lowered as the concentration of CO_2 increases. This results in a decrease in the specific heat ratio of the

mixture and also a decrease in the local speed of sound, which lowers the local flow velocity. Additionally CO_2 has a cooling effect on the flow decreasing the local flow temperature along with the speed of sound.

2. 7   Transverse Liquid Injection

Liquid jets injected transversely into fluid cross flows are relevant in many fields of research and have been extensively studied. A few engineering examples of liquid injection include boundary layer film cooling and jet engine liquid fuel injection. This experiment involves liquid carbon dioxide (CO_2) injection into both subsonic and supersonic flows. The correlations presented here for normal fluids, liquid at standard temperature and pressure, should still be relevant to this research, even though carbon dioxide has a unique chemical nature causing it to gasify at relatively low temperatures and high pressures, as shown in Figure 11. This is hypothesized because the jet breakup mechanisms discussed are fundamentally based on momentum of the fluidic jet. Thus, even if the liquid jet is converted into a two-phase solid/gas mixture of CO_2, the overall momentum of the jet stream should be conserved. Nevertheless, this section will not delve deeply into the subject of atomization but will merely touch on some of the more important, universally accepted results.

A generic spray plume created by liquid injection into a cross flow can be divided up into three regions: (1) a continuous liquid column core (2) elongated liquid ligaments that are striped away and (3) atomized droplets that rapidly disperse (Fuller, Wu,

Kirkendall and Nejad, 2000:65). Figure 12 is a simple illustration of a generic transverse liquid jet breakup and atomization plume.
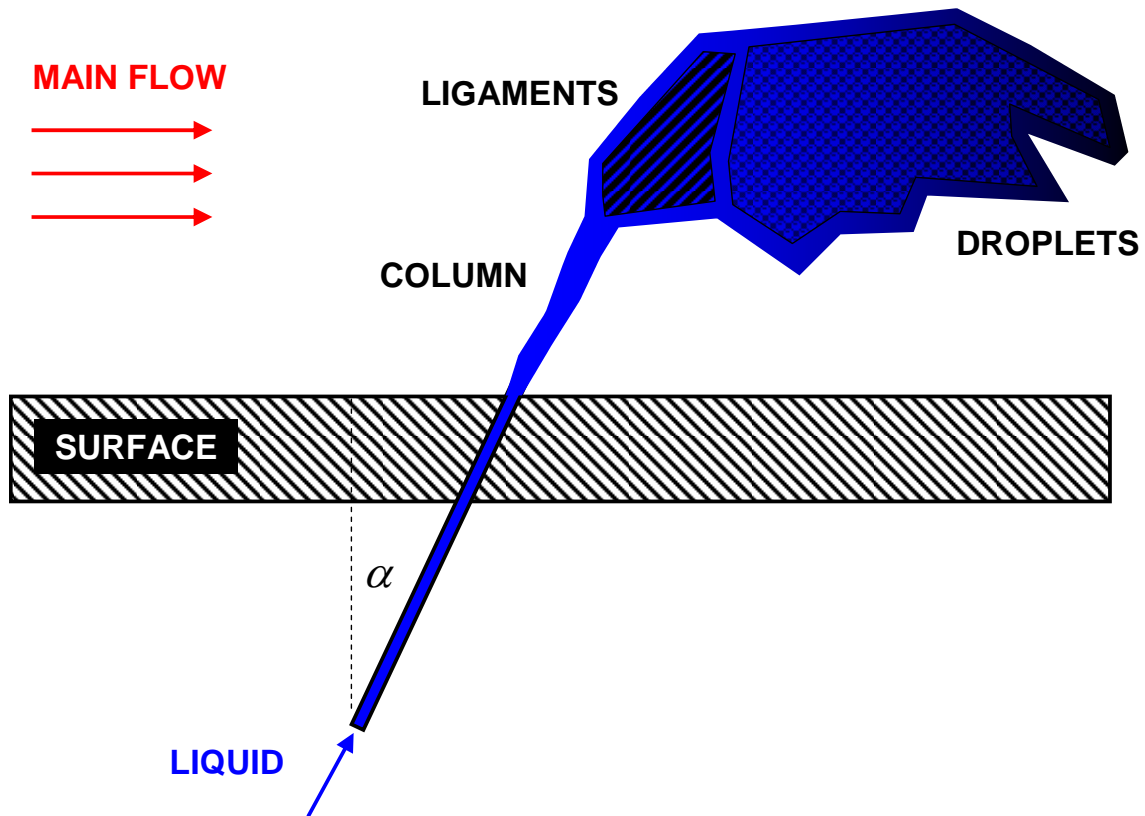
Figure 12: Generic liquid injection atomization plume.

The break up and atomization characteristics of a liquid jet are quite complicated, requiring designers to use empirical databases covering a wide range of injector geometries and operational conditions (Fuller, Wu, Kirkendall and Nejad, 2000:64). Fortunately, the basic characteristics, including penetration distance, atomization profile and jet divergence, have been linked to certain variables such as injection angle α, the ratio of jet to free stream momentum flux $\bar{q}$ (dynamic pressure ratio) and the breakup

regime parameter τ. The following equations define the variables mentioned above where *We* is the liquid Weber number, σ is the liquid surface tension and *ID* is the injector diameter. The subscripts denote *J* for jet values and ∞ for free stream values. It should be noted the jet velocity $\vec{V}_J$ is found using Eqn (39).

$$\bar{q} = \frac{\rho_J \vec{V}_J^2}{\rho_\infty \vec{V}_\infty^2} \tag{48}$$

$$\tau = \frac{3}{2}\sqrt{\frac{\rho_J}{\rho_\infty}}\left(\frac{\vec{V}_J}{\vec{V}_\infty - \vec{V}_J \cos\alpha}\right) We^{-\frac{1}{3}} \tag{49}$$

$$We = \frac{ID\rho_J \vec{V}_J^2}{\sigma} \tag{50}$$

The two major mechanisms affecting jet disintegration are external aerodynamic forces (drag) and internal fluidic forces (surface tension, liquid inertial forces and turbulent instabilities). The weighted contribution of each mechanism has been directly related to Eqn (49):

> When $\tau < 1$ the column breakup is largely dominated by aerodynamic mechanisms. The liquid column exhibits well-defined…surface waves. As $\tau \to 0$ the surface waves become more complex and the atomization process is enhanced. Conversely, when $\tau > 1$ the column breakup is largely dominated by non-aerodynamic mechanisms. As τ increase the liquid column becomes very straight and exhibits large kinks and twists prior to breakup. (Fuller, Wu, Kirkendall and Nejad, 2000:71-72)

52

For a given set of operating conditions the dominant factor in determining jet penetration is $\bar{q}$ (Fuller, Wu, Kirkendall and Nejad, 2000:67) (Chen, Smith, Schommer and Nejad, 1993:6). Additionally, the injection angle α is reported to affect the overall process:

> For a given set of operating conditions, decreasing α causes the liquid column to straighten, the column penetration decreases, the atomization process is inhibited and the column fracture becomes periodic (pulsating) in nature. (Fuller, Wu, Kirkendall and Nejad, 2000:71)

Upon injection into supersonic cross flows, a bow shock will form upstream of the liquid column. This creates a stagnation region in-between the shock and liquid jet. As the main flow media accelerates around the jet, observed to create an elliptical surface, it regains supersonic speed. The jet fractures shortly behind the local sonic point. Additionally, the sonic point on the liquid jet occurs further downstream as $\bar{q}$ increases (Li and Karagozian, 1991: 2-4).

Transverse liquid injection into a high-speed subsonic crossflow was researched by Chen, Smith and Schommer using a laser sheet imaging technique. Besides commenting on injector geometry effects, the paper also noted the presence of two vortices immediately upstream of the injector orifice. Additionally a "rather larger recirculation region, ~20 injector diameters in size, forms in the wake of the jet immediately downstream of the injector" (Chen, Smith, Schommer and Nejad, 1993:5).

2. 8   Test Section Models

2. 6. 1   *Cavity Flow.*

A hollow recess in the wall bounding a fluid flow is termed a cavity. This aerodynamic configuration appears in many applications, from automotive wheel wells to open aircraft weapon bays. Cavity flow is unsteady due to self-sustaining oscillations present in and around the cavity opening (Rockwell and Naudascher, 1978:152). The nature of these oscillations is dependent on many parameters including length, depth, span, and overall shape of a cavity. During supersonic flow cavities may oscillate predominantly along any one of the major axes of the geometry (length, span, width). When the length to depth ratio of the cavity is greater than one, which implies a long shallow cavity, longitudinal oscillations are the dominant feature. Cavity flow oscillation can be described using acoustic feedback. This assumes vortices shed from the leading edge of the cavity propagate downstream and interact with the cavity trailing edge, creating acoustic pulses traveling upstream inside the cavity. These pressure waves cause disturbances within the unstable shear layer and the separating boundary layer driving the process to repeat. A vortex is present in the downstream portion of the cavity and is sustained by mixing with the shear layer and other vortices upstream in the cavity. A separate vortex is generated upstream in the cavity due to flow separation. This causes the flow separation point to vary with time. These vortices within the cavity drive the mass transfer in and out of the cavity. The acoustic waves reflecting back and fourth

within the cavity cause the shear layer to deflect up and down near the trailing edge. This causes high pressures near the downstream cavity face. An increase in cavity length to depth ratio causes the shear layer thickness to grow due to entrainment and the surface pressures along the upstream face and cavity floor to decrease (Zhang and Edwards, 1990:355-362). Figure 13 illustrates the general flow structures predicted during supersonic cavity flow based off the referenced information above and the Schlieren pictures provided by Bjorge et al (Bjorge, Reeder, Subramanian, Crafton, and Fonov, 2005:1470).
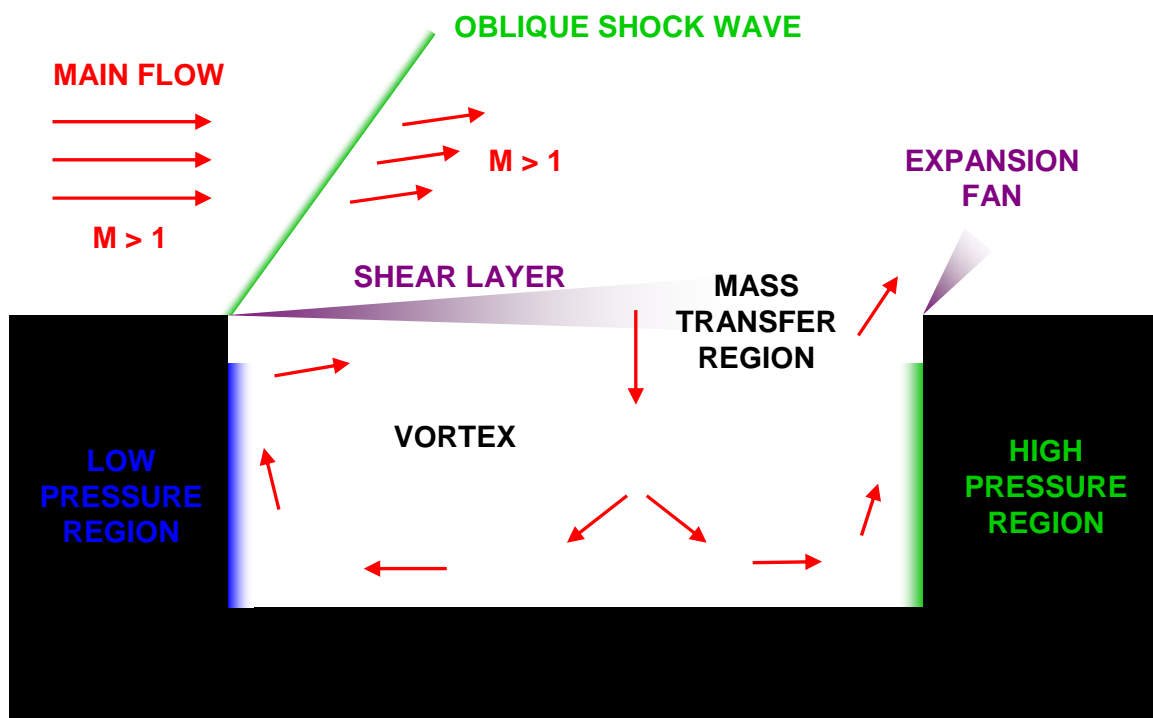
Figure 13: Structures present during supersonic flow over a cavity.

The flow within a cavity is chaotic and the Mach numbers are predicted to be predominantly subsonic. Thus direct injection up through a cavity would be a hybrid of

transverse injection through a low speed fluid initially and then transition to transverse injection through a supersonic fluid as the jet approached the fluctuating shear layer near the cavity entrance.

2. 6. 2   Cone Flow.

The tip of a missile or the conical nose of a high performance jet aircraft can be modeled using a cone. Supersonic flow around a cone has been extensively studied and is well understood. This made it a good candidate for PIV verification using liquid CO_2 injection. A cone at zero angle of attack immersed in a supersonic airflow going left to right is shown in Figure 14 with the significant flow structures and regions labeled (Schlieren picture taken by Author at the W. R. Woolrich Laboratories, Aerospace Engineering Department, The University of Texas at Austin, 2005). The prevalent flow structures seen are the leading conical shock wave emanating from the cone tip, the trailing expansion wave attached to the cone trailing edge, the recirculation region immediately aft of the cone base, and the recompression shock. The most important parameters used to describe conical flow are the cone half angle θ, also equal to the flow deflection angle, and the freestream Mach number. From these values the shock wave angle β can be determined and the flow properties surrounding the cone can be calculated.
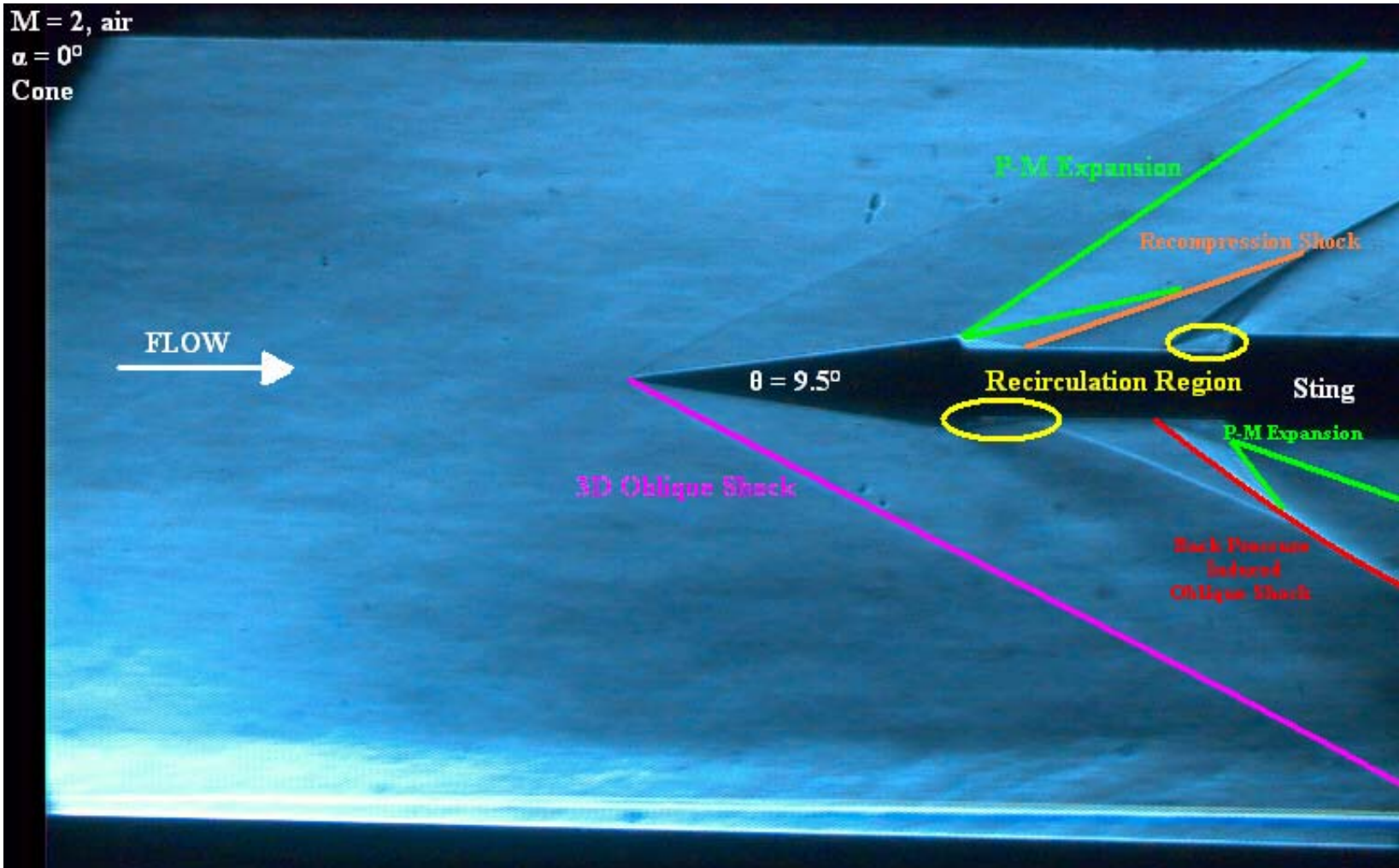
Figure 14: Flow structures present during supersonic flow over a cone.

57

3. Methodology

3.1 Experimental Apparatus and Setup

3.1.1 Wind Tunnel System.

All tests were conducted in the supersonic wind tunnel lab located at the Air Force Institute of Technology (AFIT), Wright-Patterson Air Force Base, OH. An open-circuit blowdown pressure-vacuum wind tunnel with a Mach 2.9 nozzle, a rectangular test section measuring 2.5" x 2.5" x 11" and a variable second throat diffuser was utilized. The main flow media consisted of dry air at a stagnation temperature of 295 K. Figure 15 shows a schematic of the lab and important equipment associated with running the wind tunnel.
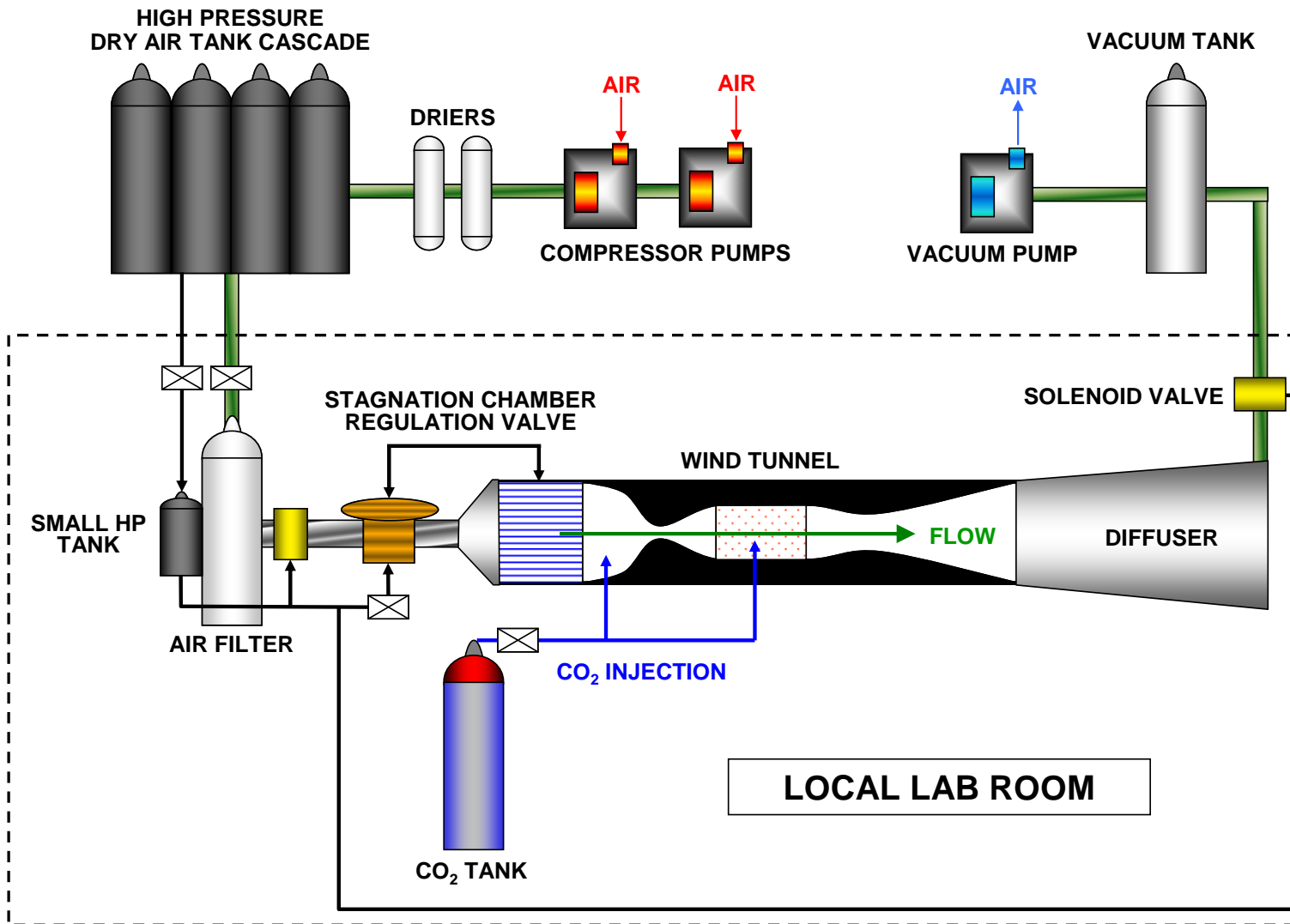
Figure 15: AFIT supersonic wind tunnel lab schematic

59

High-pressure dry air at both 160 psia and 100 psia was fed into the local lab room using two separate piping paths. For safety, both paths passed through separate cutoff valves. The lower pressure path led into a small high-pressure (HP) tank maintained at 100 psia, used to control the wind tunnel solenoid valves. The high-pressure main path flowed through a filter which removed any residual water and contaminates from the air before it flowed through the wind tunnel as the main flow media. The 100 psi air stored in the small HP tank not only actuated the pressure-vacuum solenoid valves but it also provided the control pressure (CP) needed by the Leslie GPK-1 regulator valve to reduce the 160 psi main air down to the required stagnation pressure. Equation (33) was used to calculate the stagnation pressure required to start the empty wind tunnel at Mach 2.9; $P_O = 2.795 * Pvac_{max}$, or approximately three times the maximum expected vacuum pressure (back pressure). The maximum desired vacuum pressure was arbitrarily chosen to be 4.0 psia based on reasonable wait times for the vacuum tank to empty after each run. This dictated the regulator control pressure be set no lower than 12 psia. However, for runs involving test models (which reduced the flow area in the test section), higher stagnation pressures were used ranging from 25 – 39 psia.

The main air leaving the final conditioning filter was first passed through an El-O-Matic EDA 100-A solenoid valve shown at the bottom of Figure 16. The air then flowed through the Leslie reduction valve and the conical stagnation flow straightener, shown in Figure 17, before entering the converging-diverging (C-D) nozzle.
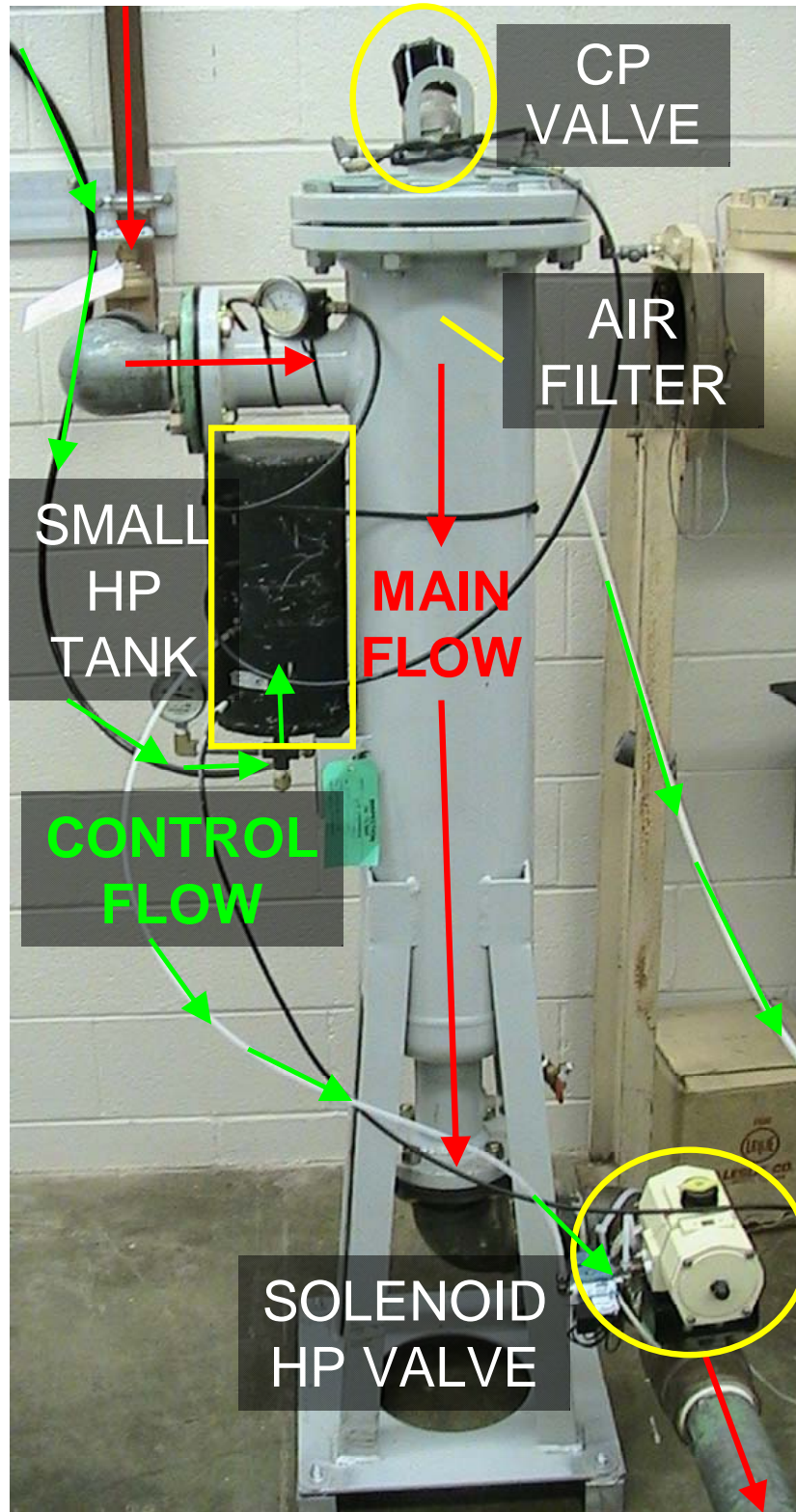
Figure 16: Final main flow filter, control tank and high pressure valve.
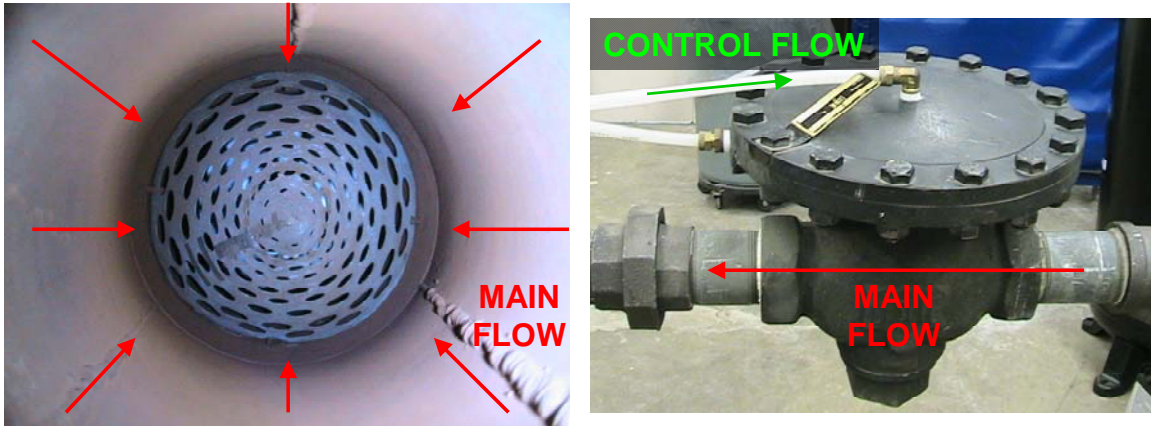
Figure 17: Conical flow straightener (left) and Leslie regulation valve (right).

The C-D nozzle shown in Figure 18 was designed and geometrically shaped to prevent shock formation within the nozzle and to provide a collimated, uniform flow field to the test section at Mach 2.9. Based on the design Mach number and the known test section area, a throat height of 0.65 inches was calculated using isentropic theory Eqn (19).
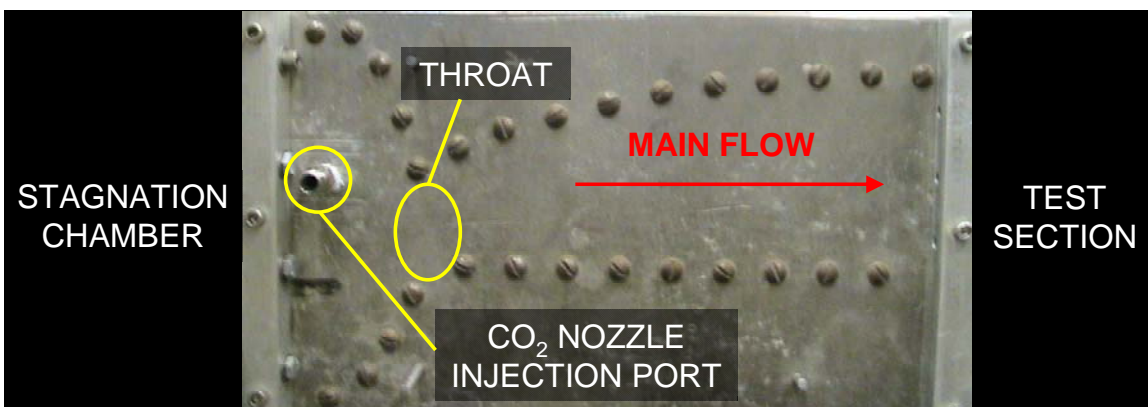
Figure 18: Mach 2.9 converging-diverging nozzle.

Based on estimated nozzle dimensions a nozzle schematic was created which is shown in Figure 19. Using approximated linear changes in flow area and assuming air enters the nozzle at stagnation conditions, the flow properties of dry air ($\gamma = 1.4$) were calculated at every point through the nozzle using Equations (16) through (20) and are included in Figure 19. The values calculated are tabulated in Appendix D.

Implementing Eqn (22) the range of air mass flow rates used can be calculated. From the isentropically calculated throat area $A^* = 1.05E - 3$ m and values $\gamma = 1.4$, $M = 2.9$, $T_O = 295$ K and $R = 287$ J/kg-K the equation becomes $\dot{m} = (2.471E - 6) * P_O$ kg/s. For the stagnation pressure range 25 psia to 39 psia = 1.724E5 Pa to 2.689E5 Pa the air mass flow rate range is calculated to be 0.426 kg/s to 0.664 kg/s.
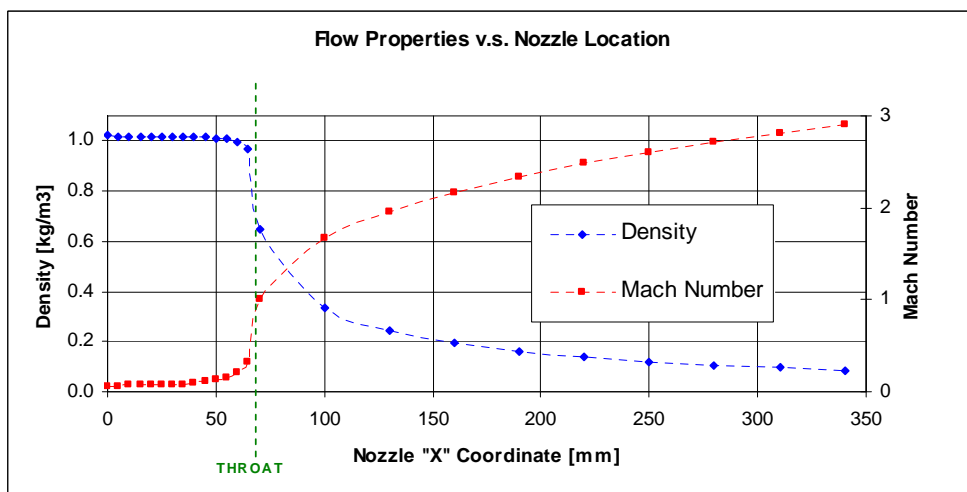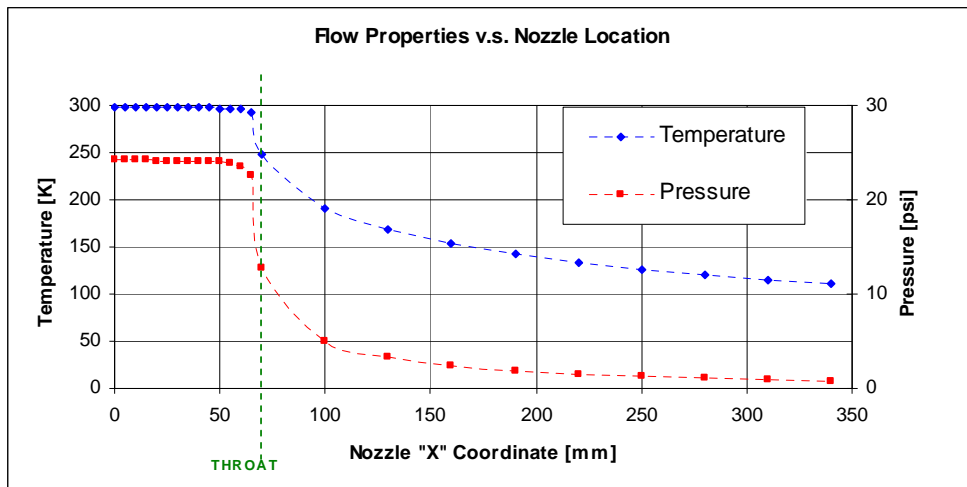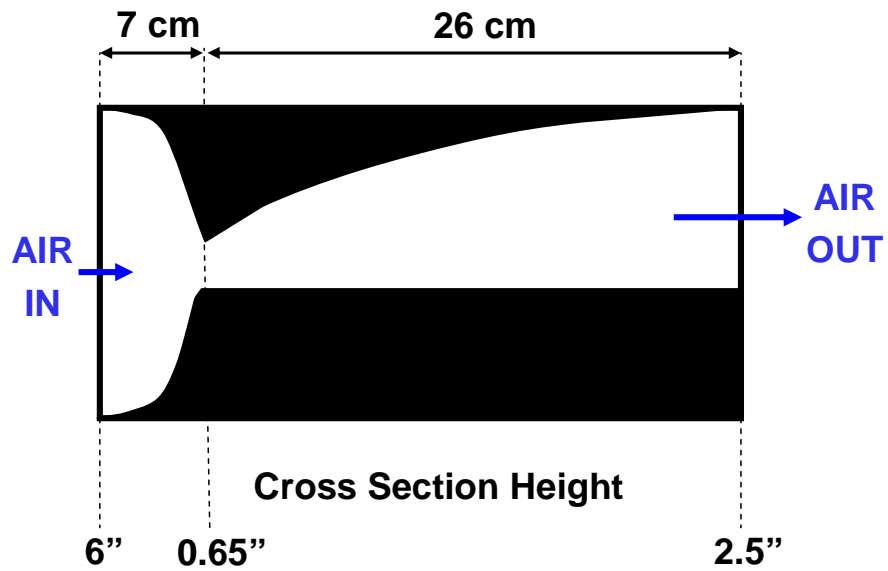
Figure 19: Mach 2.9 nozzle schematic; properties based on quasi-1D analysis.

To accommodate laser diagnostics the test section, shown in Figure 20, had two transparent side walls constructed out of a plastic based material (possibly plexiglass, Lexan or polyvinyl carbonate) and a metal roof containing a small glass inlay.
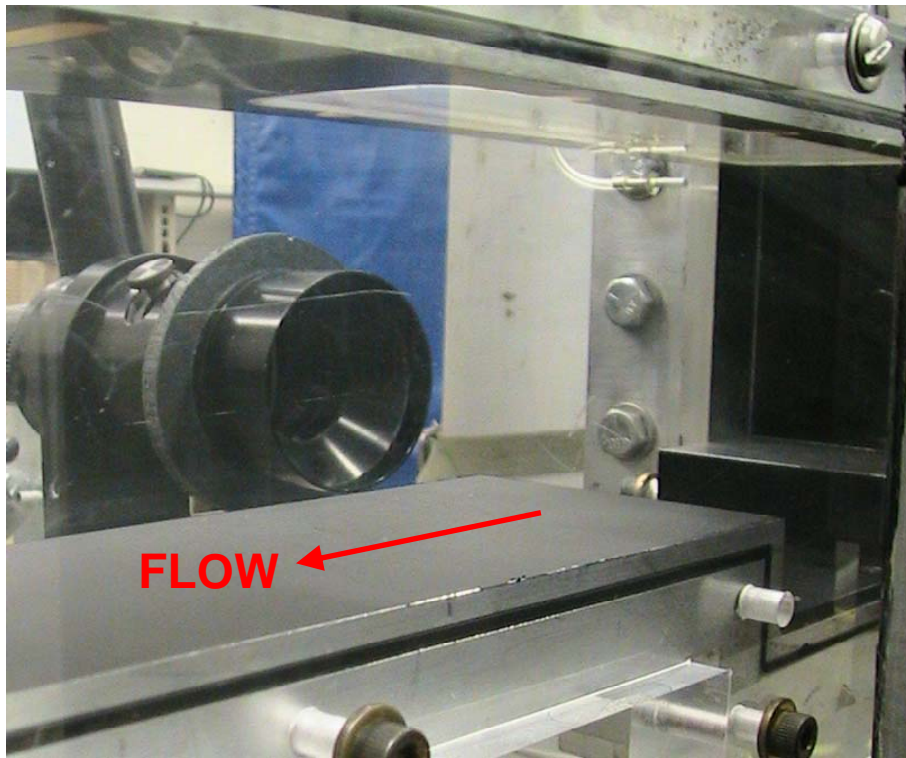
Figure 20: Wind tunnel test section.

After passing through the C-D nozzle and test section the gas mixture, predominately air but now containing slight amounts of CO_2 due to injection, would flow through a variable second throat supersonic diverging diffuser before entering the vacuum tank. A picture of the supersonic diffuser is shown in Figure 21.
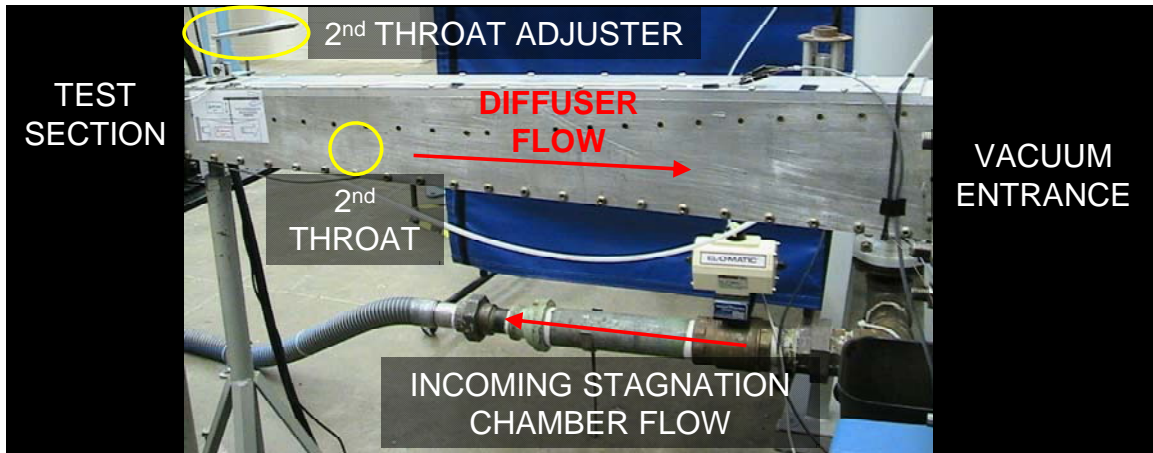
Figure 21: Supersonic wind tunnel diffuser

Using Eqn (34) the minimum second throat required to start the wind tunnel was calculated to be 2.94E-3 m^2, based on the nozzle throat area of 1.05E-3 m^2 estimated from isentropic theory. Though the second throat could be adjusted to a minimum of 1.87E-3 m^2 to maximize flow efficiency during a test, it was left completely open offering an area of 4.29E-3 m^2.

Four Endevco pressure transducers, each paired with a separate Endevco Model 4428A signal conditioning box, were utilized to monitor the flow pressures at specified locations in the wind tunnel. Transducers capable of measuring gage static pressures between 0-50 psig were attached to the control pressure and the stagnation (stilling) chamber. Transducers designed to measure absolute static pressure were attached to the test section and the vacuum piping line. The test section transducer had a measurement range of 0-50 psia, which is too large; a range from 0-15 psia would have been sufficient. The vacuum transducer had a measurement range of 0-15 psia.

National Instruments (NI) LabView software, version 8.0, was used to create a virtual instrument (VI) to control the high-pressure (HP) and vacuum solenoid valves, trigger the Dantec FlowManager software to begin collecting PIV data, record the pressures measured by the wind tunnel transducers during a wind tunnel test and automatically shutdown the wind tunnel at a specified maximum vacuum pressure. A NI BNC-2120 data acquisition (DAQ) board controlled by a NI PXI-1042 computer using a PXI-6070E multifunction I/O module controlled all of the tasks listed above by simultaneously receiving and sending both analog and digital signals. Specifically, the solenoid valves (HP and vacuum) were triggered with an analog signal of 5.0 V and the PIV system was triggered with a positive edge digital square wave of 5.0 V. The NI components are shown in Figure 22. The DAQ board is shown on the left. The computer and I/O module are shown top right and the entire wind tunnel control system is shown bottom right; note the four transducer signal conditioning boxes displaying pressures in red LED digits.
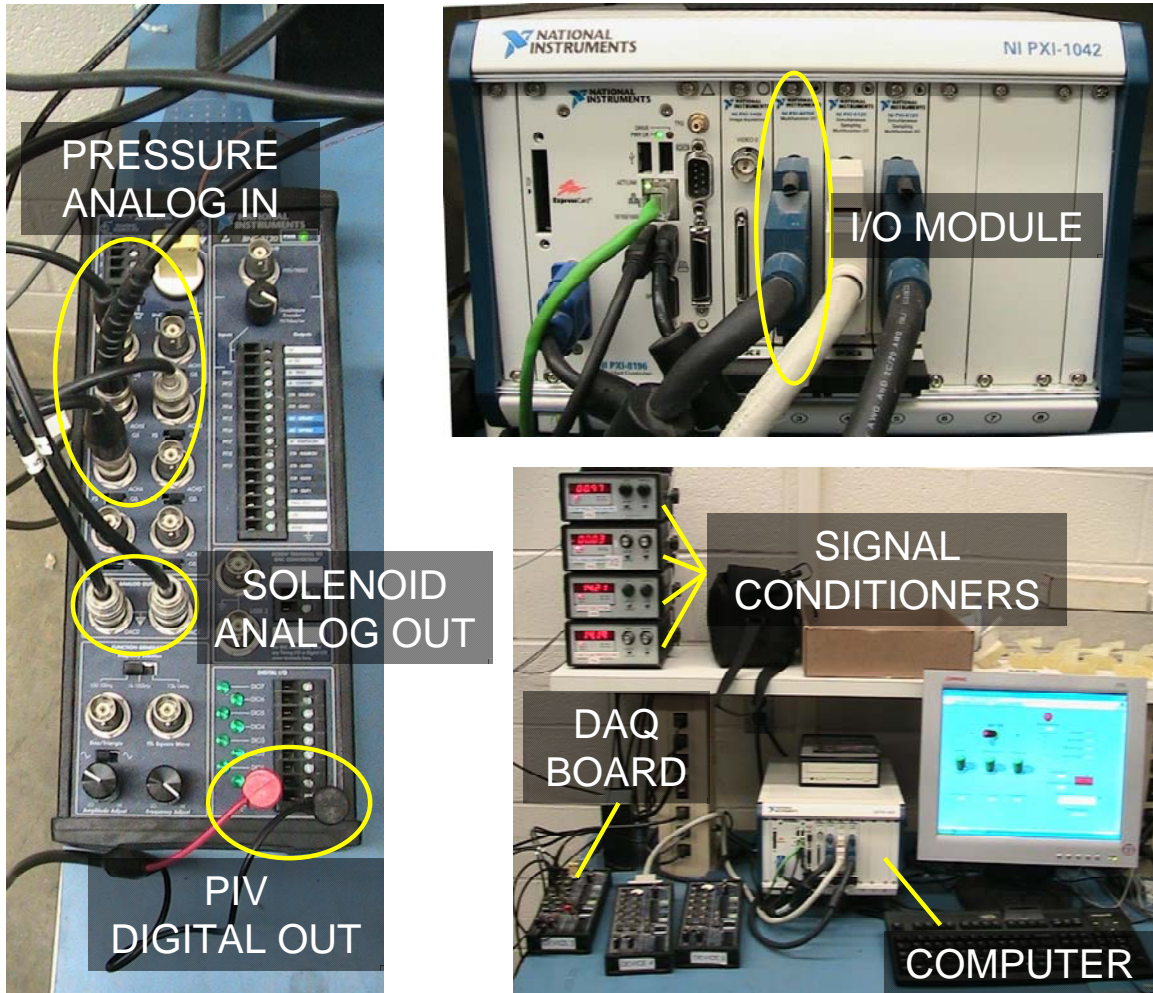
Figure 22: NI hardware used to control and monitor the wind tunnel

3. 1. 2   PIV System.

The Dantec PIV system alluded to in the previous paragraph was used to simultaneously trigger the camera and laser. A personal computer running Dantec FlowManager software, version 4.50.17, was used to setup and control the PIV test variables in addition to performing the PIV post-processing analysis.   The personal computer was connected via ethernet cables to the FlowMap Hub which sent the triggers specified by the FlowManager to the PIV peripherals (laser and camera).

The Dantec PIV system is shown in Figure 23 setup on its new mobile workbench. By grouping the entire PIV system onto a single mobile workbench, the PIV capability can now be easily relocated to any lab at AFIT.
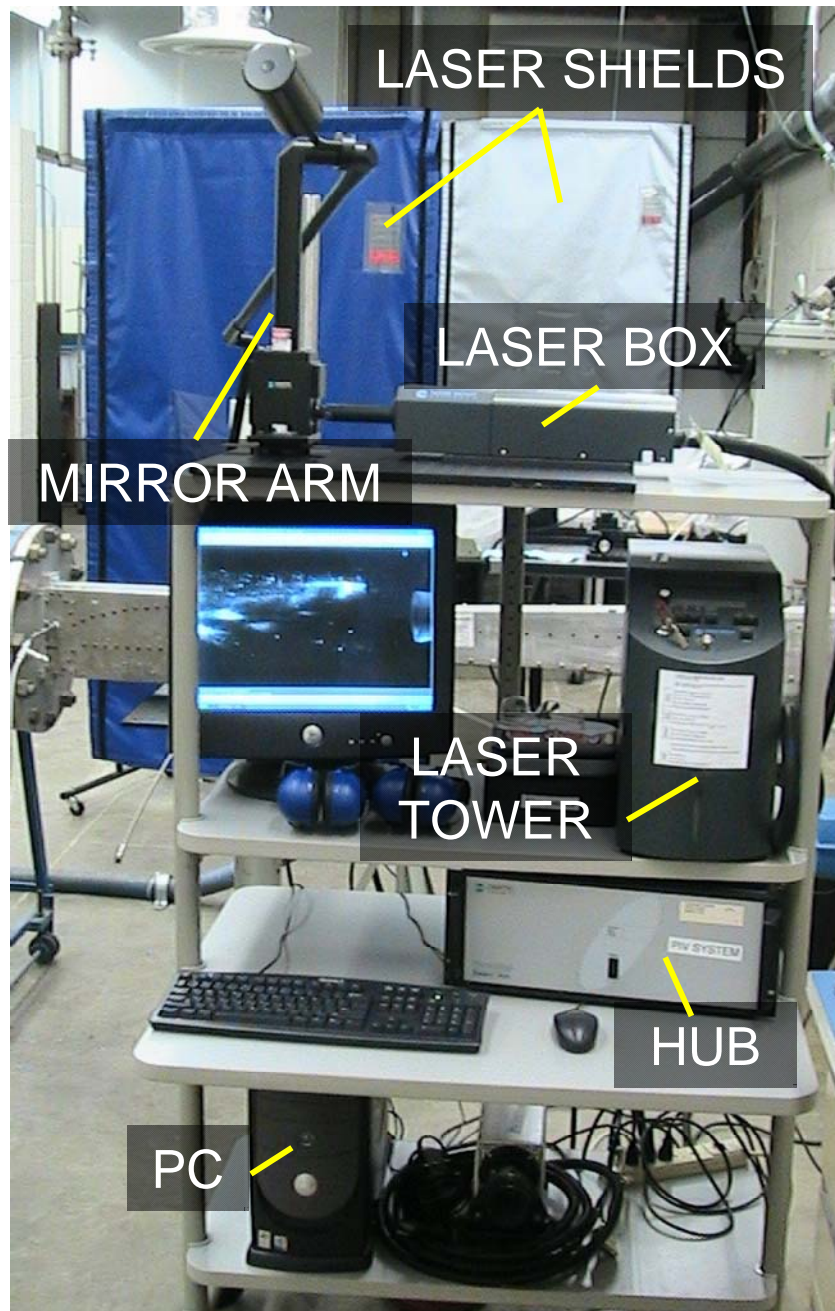
Figure 23: Mobile Dantec PIV system.

The camera/laser synchronization timing was constant for all tests performed. Figure 24 illustrates the synchronization between the laser and camera in order to obtain two IM. For clarification, note the lab room was darkened during each test, thus the particles were only illuminated for 5.0 ns, not the entire exposure integration time. The *TEST* time line at the bottom of the figure shows the time delay before sequential image pairs, or *bursts*, were acquired. The number of bursts (IM pairs) was set between 50 and 75, resulting in test run times of 12.5 to 18.75 seconds, respectively. It should be pointed out even though the time between laser pulses was set to 1 μs, the camera user's manual indicated a minimum *transfer pulse width* of 12 ms. This is the time required to transfer one image from the photo diode array (pixel array) to a storage cell array. If the minimum time is not allowed to clear the charges from the pixel array there could be degradation in image quality. This is discussed more in the error analysis section in connection with pixel bleed over into the storage cells. Appendix E presents screen shots of the Dantec FlowManager acquisition control (timing) and camera field of view (scale factor) setup.

|	Δt [μs]
Pulse Width	0.005
Pulses	1
Delay	26
Transfer	<1
EXP 1	999
EXP 2	64956
Burst	250000
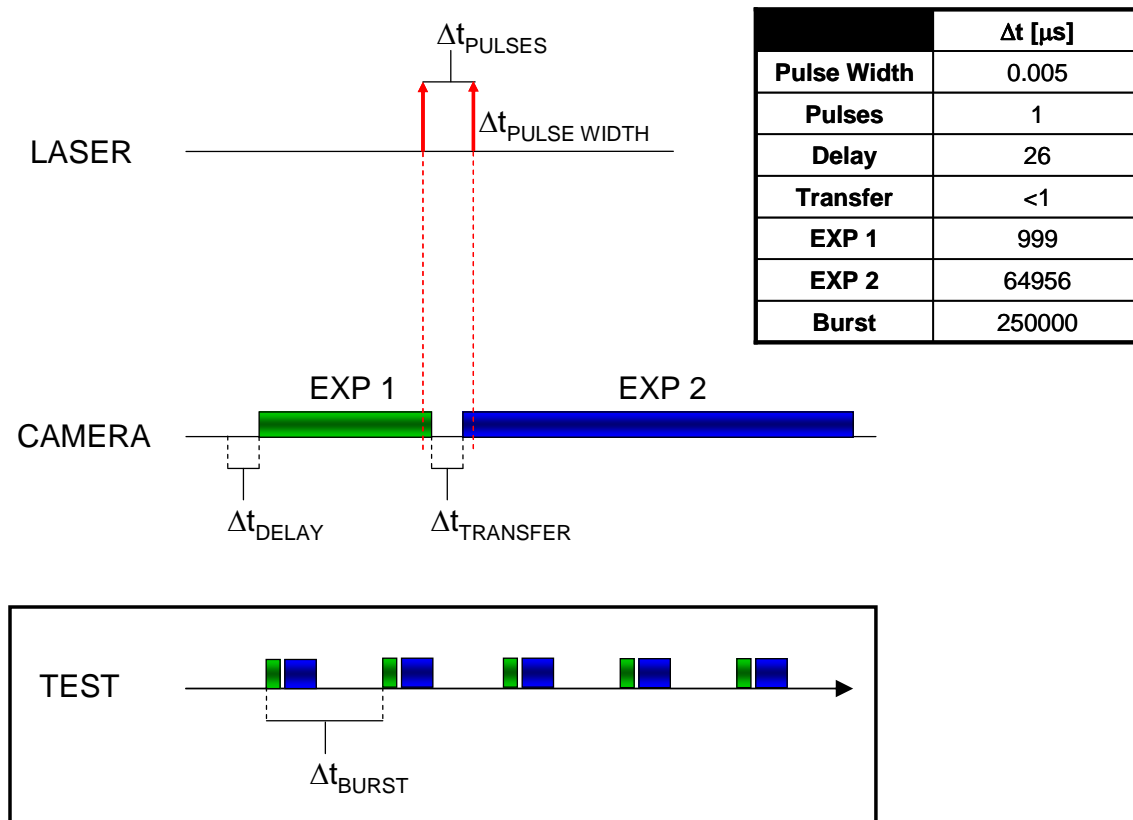
Figure 24: PIV laser, camera, and test timing.

The velocity in the test section based on $M = 2.9$ and $a = 211\,\text{m/s}$ was $\vec{V} = 612\,\text{m/s}$. During a nominal 5.0 ns laser pulse a particle moving at main flow velocity would travel 3.0 μm, which is essentially indiscernible; therefore the flow would appear frozen. However, during the 1.0 μs time between laser pulses the same particle would travel 600 μm, or 0.6 mm, which is significant enough to be detected by the PIV processing software and resolved into a velocity vector. Using Eqn (38) and the average particle displacement of 0.6 mm found above a preliminary scale factor of 3.825E-5 m/pixel was calculated for a given square interrogation region dimension $N = 64\,\text{pixels}$.

A New Wave Research Solo 120 laser system was used to illuminate the seed particles. The laser housing box contained two, class four, pulsed wave, flash lamp pumped, solid crystal Nd:YAG lasers. The laser light was converted from infrared light at a wavelength of 1064 nm to green visible light at a wavelength of 532 nm using harmonic generators (one per laser head) and emitted with 120 mJ of energy per pulse. The 5,0 ns laser pulses were relayed to the test location through a Dantec Dynamics mirror arm. At the test section, the laser energy was spread out into a diverging laser sheet using a Dantec Dynamics 80 x 20 light sheet cylindrical lens which provided the option to manually change the laser sheet focal point and therefore the sheet thickness as well. A laser trap was positioned directly across from the laser lens on the opposite side of the test section. Additionally, large laser shields were placed around the wind tunnel during laser operation to shield against unforeseen laser transmittance. Black laser light absorbing foam was attached to the cylindrical lens and placed at various locations around the test section to attenuate any reflected laser energy. Additionally, all reflective surfaces which would likely be exposed to laser light were painted flat black to reduce reflections. Figure 25 shows the laser system components; (top left) laser box containing two lasers (top right) laser absorbing foam along the test section blocked laser reflections (bottom left) cylindrical laser lens connected to work table via the lens support (bottom right) mirror arm transmits laser beam from laser box to the test section.
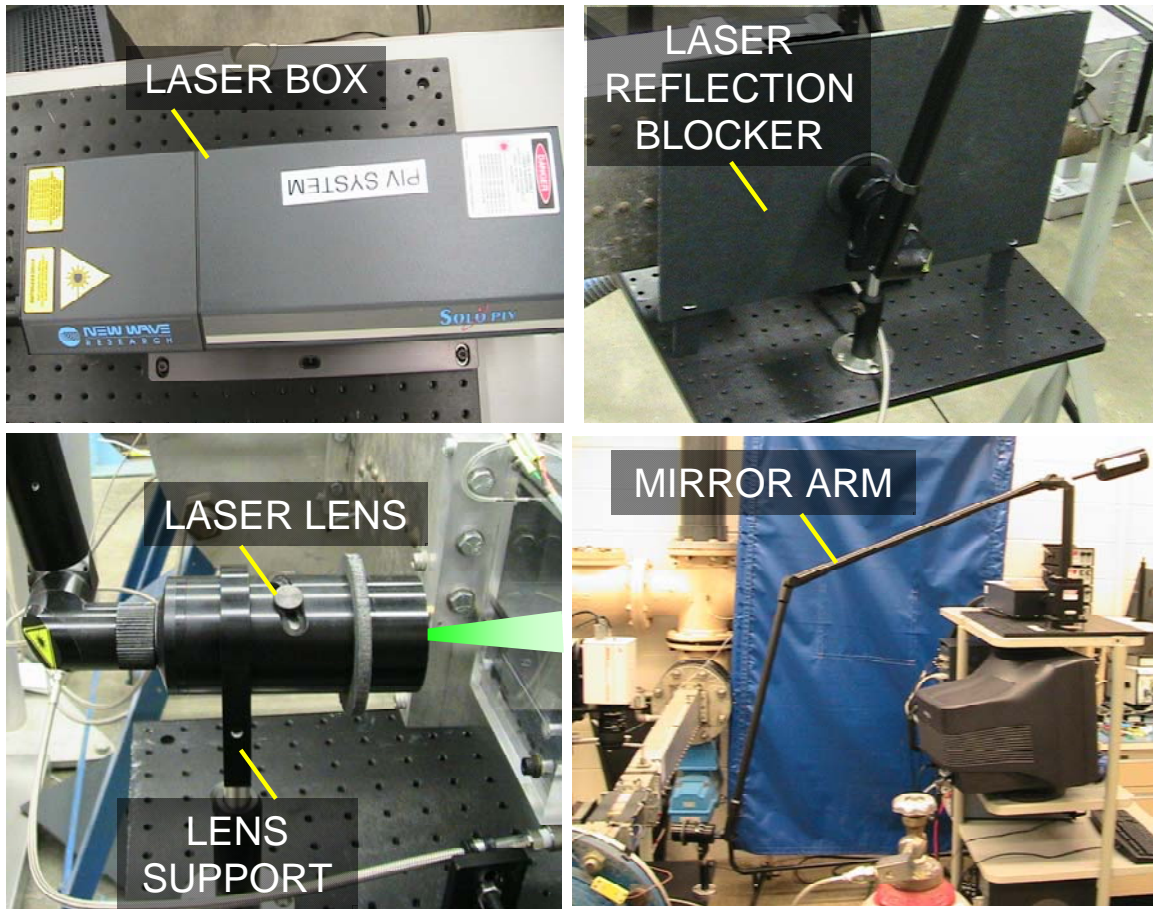
Figure 25: PIV laser system.

A Kodak Redlake MegaPlus Model ES 4.0/E monochromatic CCD digital camera was used in conjunction with a NIKON 60mm AF Micro Nikkor manual lens and a Melles Griot, 50mm light filter to image the CO_2 seed particles. The filter allowed 67.4% transmission at a center wavelength of 509 nm. A filter was used because the images consistently contained overexposed pixels, even after the laser was moved further away from the test section to allow a decrease in the laser intensity. In the end a filter which reduced light at the laser wavelength by 32% was the simplest fix. The camera was positioned above the test section as shown in Figure 26.
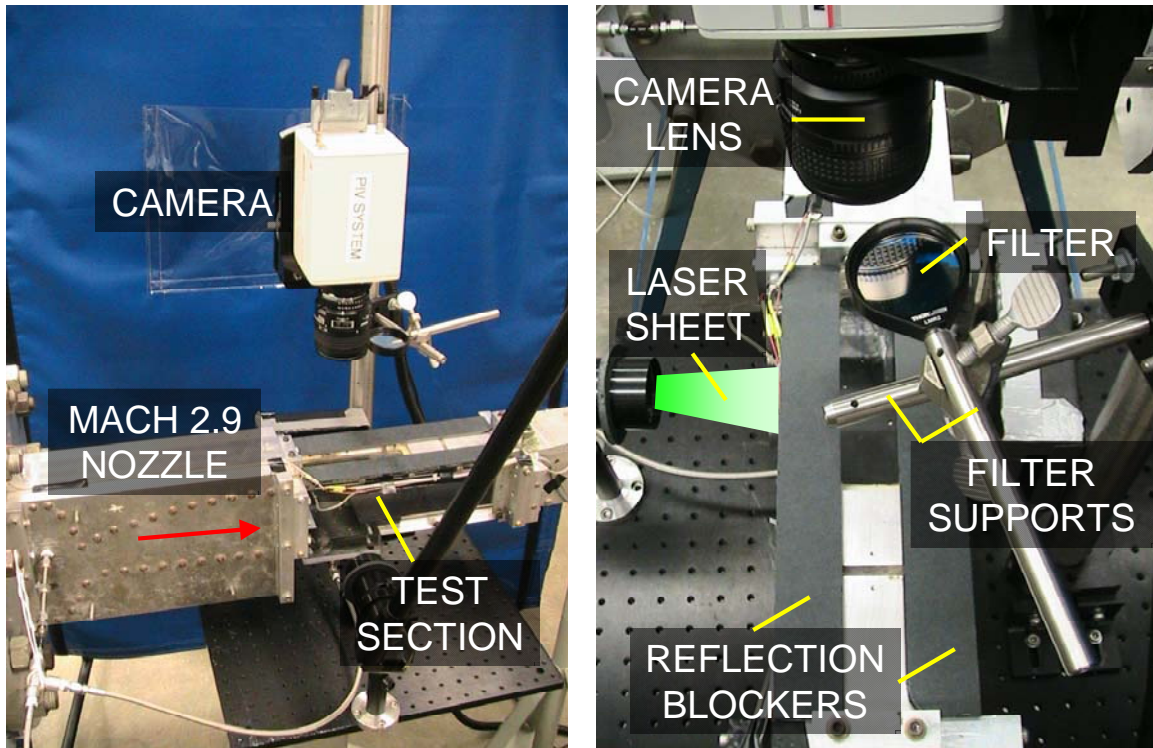
Figure 26: PIV camera setup

As seen in Figure 26, the camera and filter supports were mounted to a vertical pole attached to a worktable. Additionally the laser lens support was also locked down to the worktable. Having these components fixed in position relative to one another facilitated the adjustment of the PIV inspection plane; to study different parallel flow planes, the work table was simply raised or lowered as one single unit, leaving the camera field of view unchanged. Most of the tests were run with a scale factor $S = 3.816$ close to the preliminary value of 3.825 calculated earlier in this section.

3. 1. 3   Carbon Dioxide Injection System.

The carbon dioxide (CO_2) injection system was designed to be as simple as possible. Chemically pure liquefied compressed carbon dioxide was stored in a standard steel tank at a vapor pressure of 845 psia (57.5 atm = 5.826E6 Pa). Atop the tank a wheel valve equipped with a long eductor tube extracted liquid CO2 and fed it into Swagelok metal braided hosing with an outer diameter (OD) of 1/4 inch and an inner diameter (ID) of 1/8 inch. For some of the tests, the CO_2 flow was split using a 1/4 inch ID T-junction pipe fitting to provide simultaneous dual injection at both the nozzle injection point and the test section injection point. For all other tests a single line was run from the tank to the nozzle injection point to provide independent injection upstream of the test section. No CO_2 mass flow regulator was available so Small Parts, Inc. 316 S/S annealed cap tube STR micro-tubing was employed to choke the amount of CO_2 delivered to the injectors. Figure 27 shows the CO_2 piping setup; CO_2 tanks used one at a time (left), CO_2 flow from tank to injection points (top right) and T-junction used to divide CO_2 during dual injection (lower right).
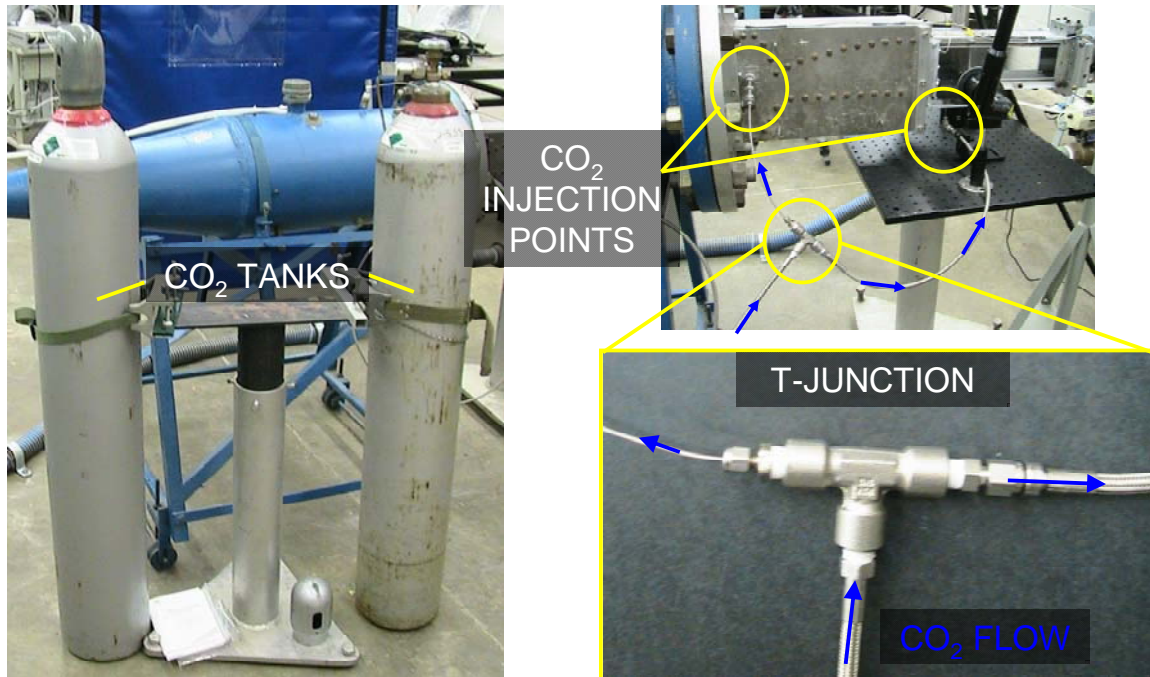
Figure 27: Carbon dioxide piping system.

Shroud type injectors were used for all tests based on previous successes by McNiel (2007). However, other injector designs were considered and are presented in Appendix E. Figure 28 shows a typical shroud injector along with feed tubes having different inner diameters (ID). A feed tube effectively limited the CO_2 mass flow rate. All of the feed tubes had a 1/16 inch OD but the ID variations included 30/1000 inch, 20/1000 inch and 10/1000 inch (left to right in Figure 28). However, the 10/1000 inch ID feed tube was the limiting case and emitted no CO_2. Trial tests proved the 20/1000 inch ID feed tube offered the best CO_2 mass flow rate for PIV. All shroud type injectors used throughout the tests had a constant 10 mm feed tube to shroud tube overlap distance. Figure 29 shows injector plumes with the 30/1000 inch emitting much more CO_2 than the 20/1000 inch.
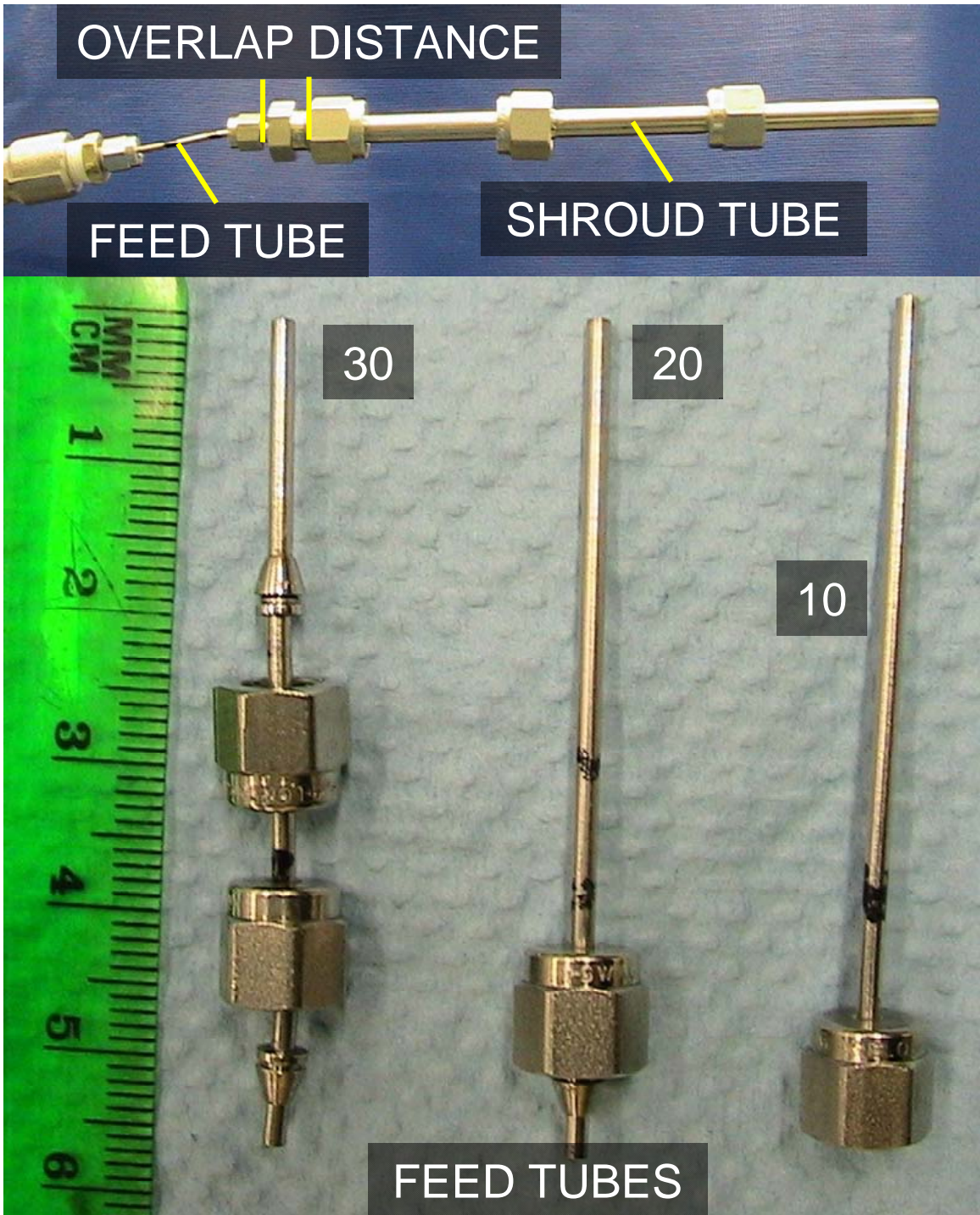
Figure 28: Shroud injector (top) feed tube variations (bottom)
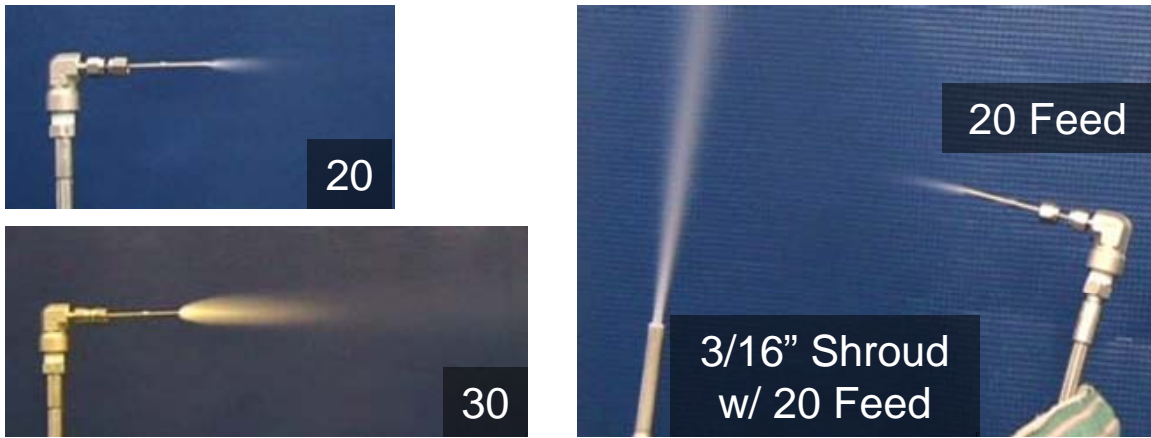
Figure 29: Injector plumes: (left) independent feed tubes (right) dual shroud/feed.

For the final test the stagnation chamber injection location was used. It was predicted this method would produce smaller particles, but it was hoped the location would introduce less flow intrusion than the nozzle location. For all other tests, the nozzle injection location was used. The nozzle injection location was upstream of the C-D nozzle throat. It is hoped the rapidly accelerating, converging nature of the flow at this point would mitigate any major flow disturbances caused by the injector shroud protruding into the flow. Figure 30 shows a schematic of the nozzle injection setup.

It was hypothesized the sparse particle distribution densities obtained with independent nozzle injection would not support accurate PIV measurements inside a cavity. One proposal to mitigate this problem was to provide additional seed particles to the area of interest utilizing a second local injector. The first series of tests inspected supersonic flow over a long shallow cavity containing a transverse CO_2 jet injected at 90 degrees, normal to the floor in the center of the cavity. For inspection of the cavity flow field two tests variations were performed. For the first test, the flow above the cavity (as shown by the upper laser plane line in Figure 31) was illuminated during dual

nozzle/cavity CO_2 injection. In the second test, the flow down in the cavity (as shown by the lower laser plane line in Figure 31) was illuminated during dual nozzle/cavity CO_2 injection. Figure 32 shows the actual cavity test section setup. Additionally, Figure 33 shows the dual nozzle/cavity injection with the wind tunnel not running (no air flow). The jet stream shows noticeable divergence and a high injection velocity allowing it to easily reach the top of the test section. However, such jet penetration is not likely when supersonic air is flowing.
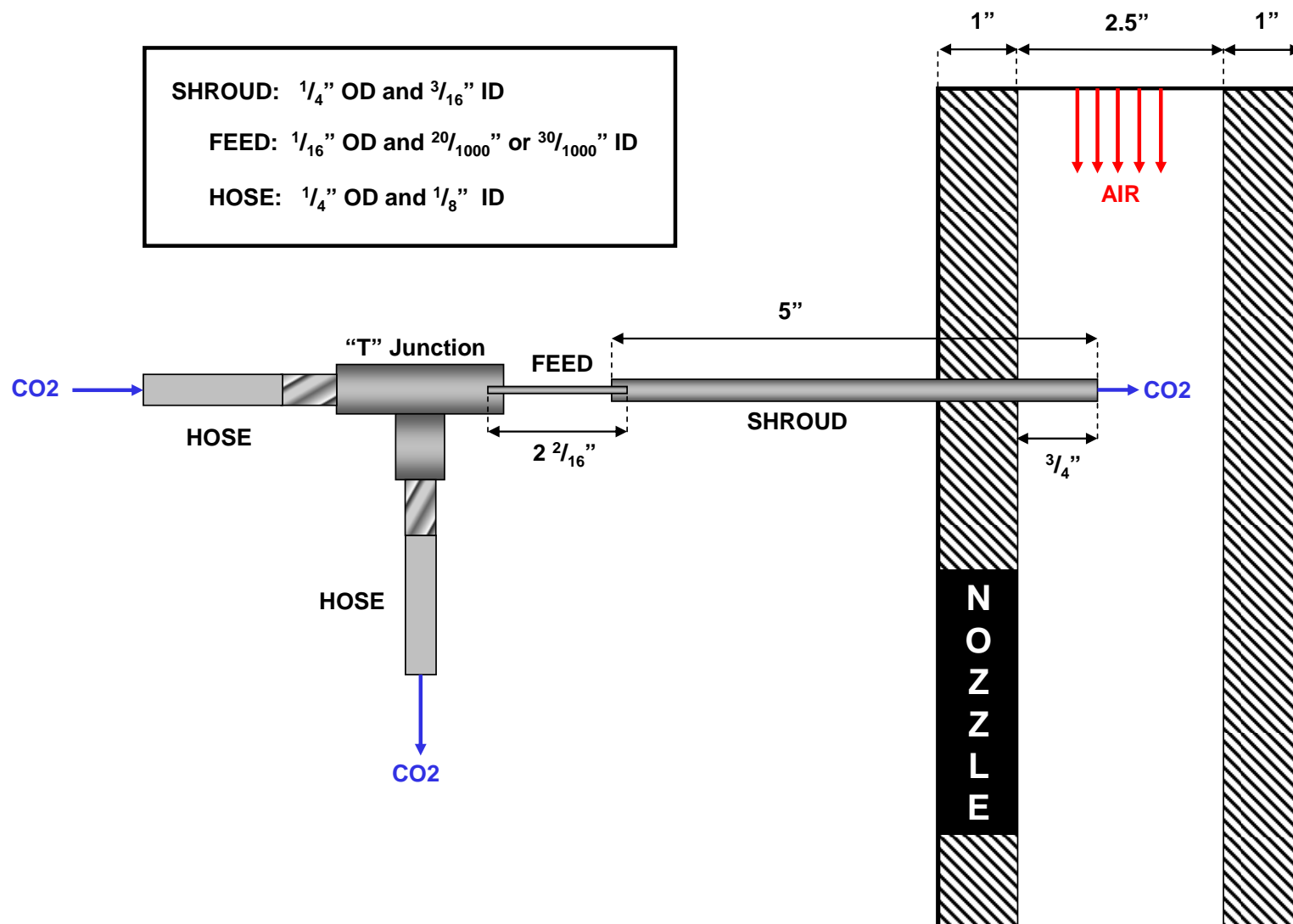
Figure 30: Nozzle injection setup; optional T-fitting for dual injection.
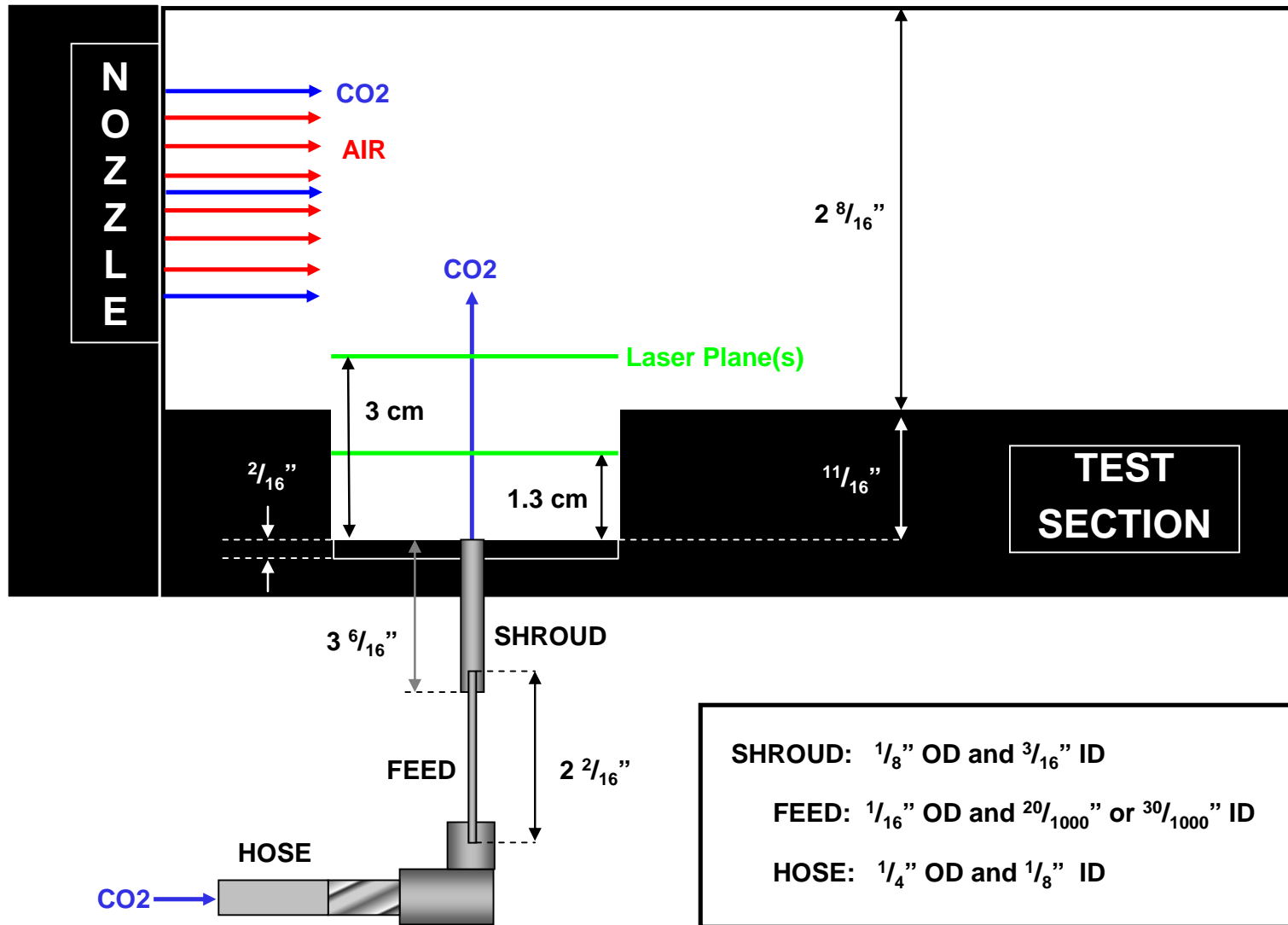
Figure 31: Test section injection setup during cavity PIV inspection.
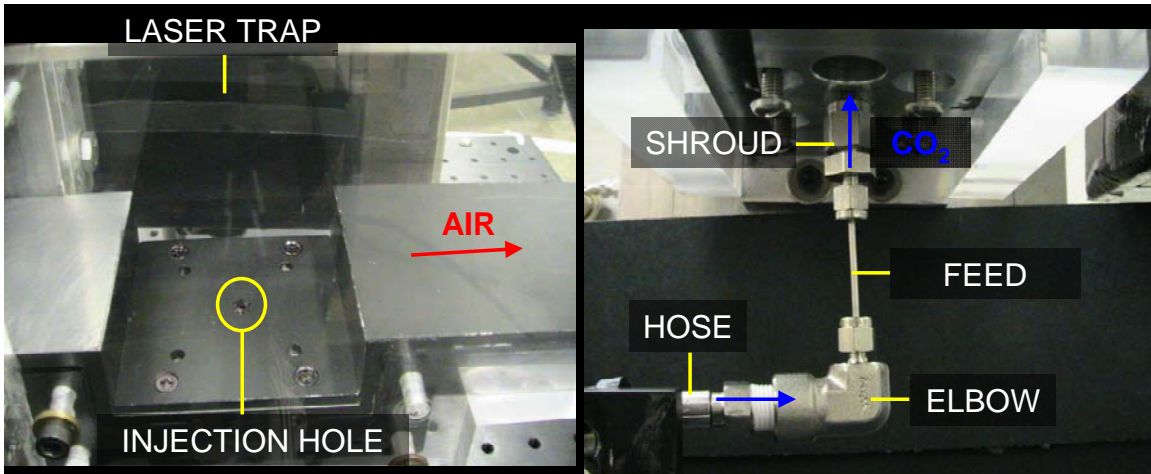
Figure 32: Cavity setup: (left) test section view (right) below test section view

Figure 33: Dual nozzle/cavity CO_2 injection with the wind tunnel off.

The second series of tests inspected supersonic flow immediately downstream of a hollow cone supported from below by a sting with a narrow diamond cross section. Two different sting designs were considered but both offered a hollow chamber through the sting to provide injection out the back of the cone. Figure 36 shows a solid model side view of the two cones used: (a) forward swept sting flushes main flow away from cone surface and (b) combination sting allows flow to remain straight or turn exactly with conical shock wave. Both cones had a cone half angle of approximately 10°. The flow aft of the cone was inspected at two different planes; first the mid-cone plane and second a plane below the cone but above the test section floor.

A theoretical shockwave angle of $\beta = 23°$ was found using a $\theta - \beta - M$ chart for cone flow with a deflection angle of ten degrees at Mach 2.9 (Ames, 1953:48). Similarly, the Mach number at the surface of the cone was found to be 2.6 (Ames, 1953:52). A Prandtl-Meyer function table yields an $\upsilon(M = 2.6) = 41.41°$ upstream of the cone base; using Eqn (32) and a deflection angle $\theta = 10°$ the Mach number downstream of the cone is calculated from isentropic theory to be $M = 3.1$. Next, to solve for the local flow velocity the local speed of sound was needed. Using a measured stagnation temperature $T_{O2} = 293\,\mathrm{K}$ Eqn (16) yields a static temperature downstream of the conical shock of $T_2 = 102.7\,\mathrm{K}$ for $\gamma = 1.385$. The local speed of sound was calculated to be $a = 201.8\,\mathrm{m/s}$ using Eqn (23). Therefore using Eqn (1) the local flow velocity downstream of the cone base was calculated to be $\bar{V}_2 = 625.5\,\mathrm{m/s}$. Figure 34 presents a schematic of the test section during the cone tests and Figure 35 shows the actual setup. Cone dimensions and 3-D views are available in Appendix G.

The last tests performed where verification tests done on an empty test section. This was to gain a baseline measurement of the undisturbed flow field using carbon dioxide seeds. Independent injection into the nozzle and then into the stagnation chamber was employed in two separate tests.
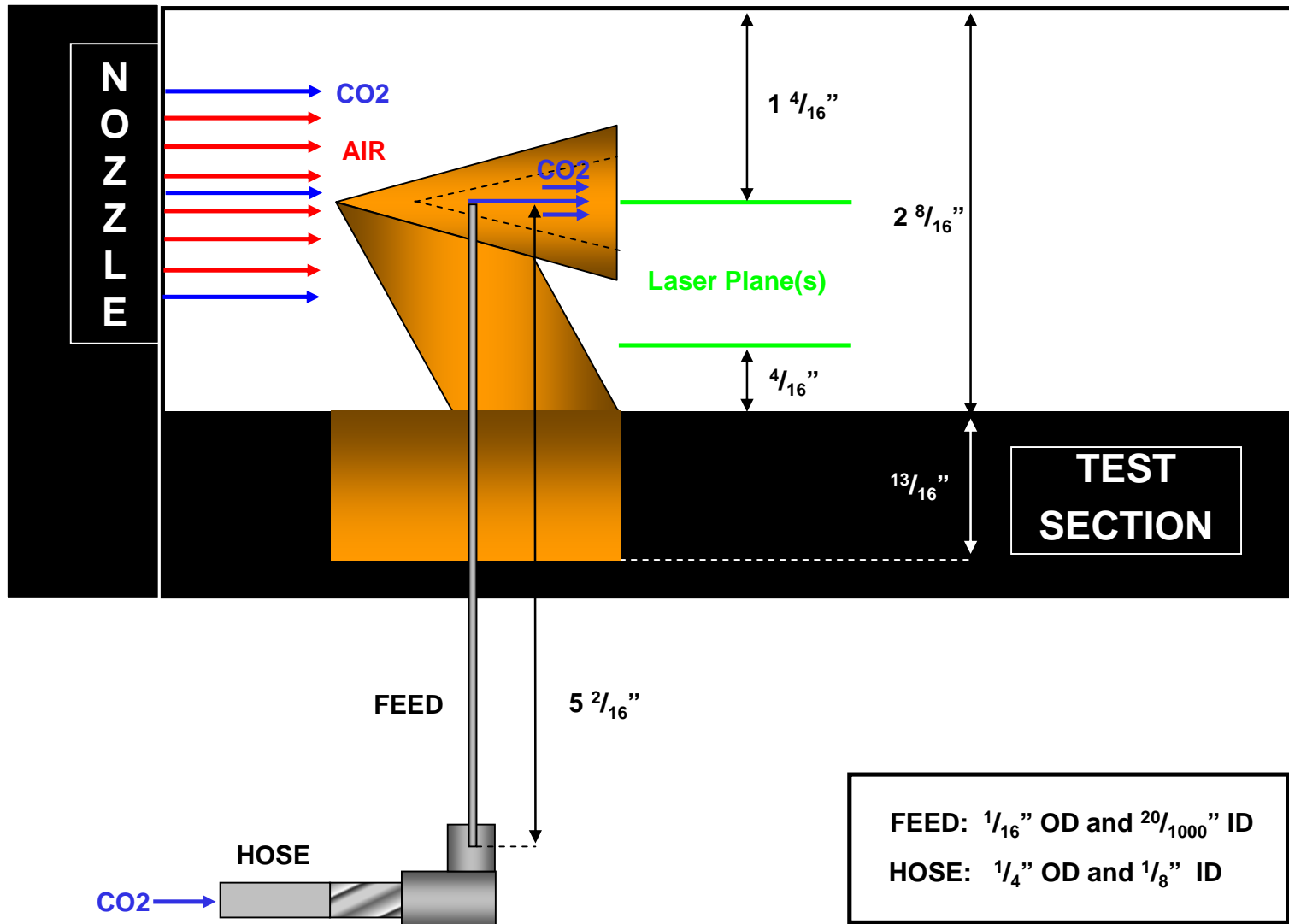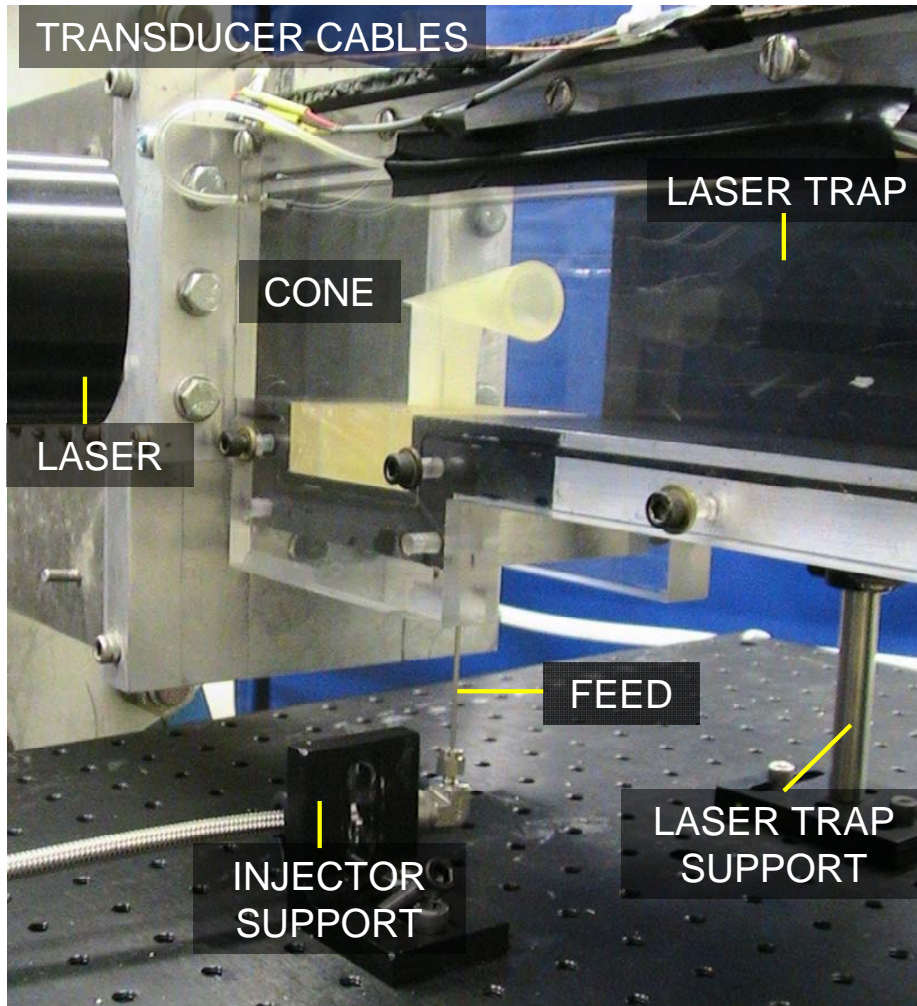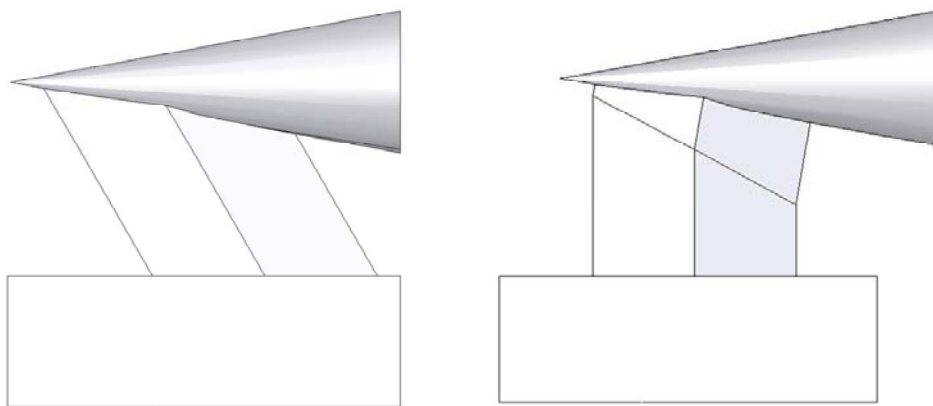
Figure 34: Test section setup during cone PIV inspection.

Figure 35: Cone setup shown with combination sting model.

Figure 36: Cone variations: (left) forward swept sting (right) combination sting.

3. 1. 4   Piping Pressure Drop Analysis.

The complete carbon dioxide piping system will be quickly analyzed to show the effects of piping on the liquid CO_2. A simplified schematic of the CO_2 piping system is shown in Figure 37.
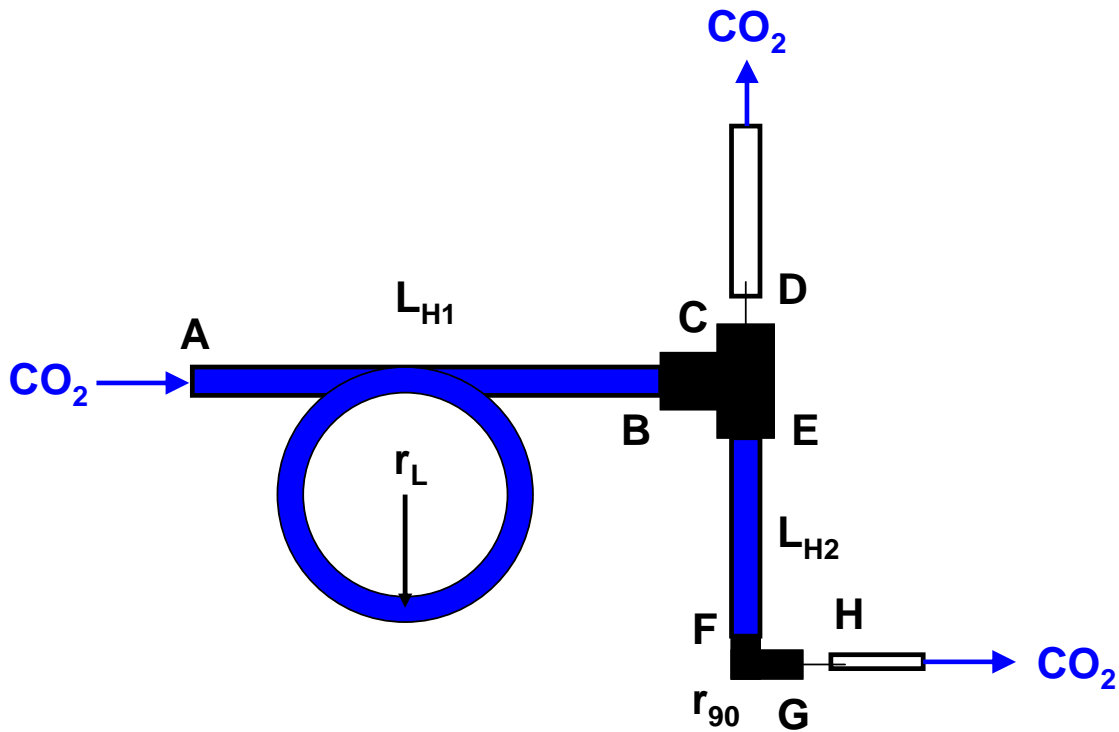
Figure 37: Simplified schematic of the dual CO_2 injection piping system.

One hose fed by the CO_2 tank was split using a T-fitting allowing simultaneous dual injection to both the C-D nozzle and test section. For some tests, only independent nozzle injection was used. Feed tubes with $ID = 20/1000$ inch were primarily used at both injection locations, so that case will be considered. Additionally, it will be assumed the CO_2 mass flow rate through each branch is equal to half the total flow rate. Values

relevant to this analysis are presented in Table 4 with subscript *AVG* for average, *T* for T-fitting, *H* for hose, *90* for elbow, *L* for hose loop and *F* for feed.

r_L

Table 4:   Relevant values used to compute pressure drop through piping.

COMPONENT	VALUE
ρ_{AVG}	1000 kg/m^3
μ	1.19E-4 kg/m-s
$\dot{m}_{TOTAL}$	0.00136 kg/s
$\dot{m}_{BRANCH}$	0.00068 kg/s
ID_{HOSE}	1/8 inch = 3.175E-3 m
ID_{FEED}	20/1000 inch = 5.08E-4 m
$ID_T = ID_{90}$	1/4 inch = 6.35E-3 m
r_L	6 inches = 0.1524 m
r_{90}	2*IDT = 12.7E-3 m
L_{H1}	36 inches = 0.9144 m
L_{H2}	18 inches = 0.4572 m
L_F	0.055 m

Using the conservation of mass equation, the velocity through each section can be found and related to the Reynolds number using Eqn (40). Starting with Eqn (39) the average pipe velocity $\vec{V}$ can be solved using internal diameter ID instead of circular pipe area.

$$\vec{V} = \frac{4\dot{m}}{\rho \pi ID^2} \tag{51}$$

The following values of average pipe velocity and Reynolds number were computed for the two hose sections, the T-fitting and the feed tubes. The flow state was based off the limits given in section 2. 5 and the friction factors were calculated using Eqn (47) for laminar pipe sections. For the turbulent pipe section the friction factor was taken from the Crane chart (Crane, 1988:A-24); Table 5 summarizes the findings.

Table 5:   Computed parameters for piping components.

VELOCITY	VALUE	Re	STATE	f
$\vec{V}_{H1}$	0.17178 m/s	4583	Turbulent	0.04
$\vec{V}_{H2}$	8.588E-2 m/s	2292	Unstable	0.028
$\vec{V}_{T}$	2.147E-2 m/s	1146	Laminar	0.056
$\vec{V}_{F}$	3.355 m/s	1432	Laminar	0.045

Next, the resistance coefficients were found for each component and related back to the conditions at the tank feed off hose using the set of equations below. In the following equations, variables with only an alpha subscript correspond to the piping components, using the nomenclature above Table 4. If the variable has both a subscript and a superscript, then the subscript corresponds to the stations in Figure 37 and the superscripts corresponds to the piping component.

$$K_{AB}^H = \left(\frac{f_H L_{H1}}{ID_H}\right) + (4-1)\left(0.25 f_H \pi \frac{r_H}{ID_H} + 0.5 K_{90}^L\right) + K_{90}^L$$

$$K_{BC}^T = (60 f_T) + \frac{0.5(1 - \varepsilon_{TF}^2)}{\varepsilon_{TF}^4} \text{ where } \varepsilon_{TF} = \frac{ID_F}{ID_T} \text{ and } K_{BC}^H = \frac{K_{BC}^T}{\phi_{TH}^4} \text{ with } \phi_{TH} = \frac{ID_T}{ID_H}$$

$$K_{CD}^F = \left(\frac{f_F L_F}{ID_F}\right) + 1 \text{ and } K_{CD}^H = \frac{K_{CD}^F}{\phi_{FH}^4} \text{ with } \phi_{FH} = \frac{ID_F}{ID_H}$$

$$K_{BE}^T = (60 f_T) \text{ and } K_{BE}^H = \frac{K_{BE}^T}{\phi_{TH}^4} \text{ with } \phi_{TH} = \frac{ID_T}{ID_H}$$

$$K_{EF}^H = \left(\frac{f_H L_{H2}}{ID_H}\right)$$

$$K_{FG}^{90} = (K_{90}) + \frac{0.5(1 - \varepsilon_{TF}^2)}{\varepsilon_{TF}^4} \text{ where } \varepsilon_{TF} = \frac{ID_F}{ID_T} \text{ and } K_{FG}^H = \frac{K_{FG}^{90}}{\phi_{TH}^4} \text{ with } \phi_{TH} = \frac{ID_T}{ID_H}$$

$$K_{GH}^F = \left(\frac{f_F L_F}{ID_F}\right) + 1 \text{ and } K_{GH}^H = \frac{K_{GH}^F}{\phi_{FH}^4} \text{ with } \phi_{FH} = \frac{ID_F}{ID_H}$$

The non-dimensional diameter ratios were calculated to be $\varepsilon_{TF} = 0.08$, $\phi_{TH} = 2$, and $\phi_{FH} = 0.16$. From the Crane schematics (Crane, 1988:A-29), the values are $K_{90} = 12 f_T$ for the elbow and $K_{90}^L \approx 50 f_H$ for the hose loop. Table 6 summarizes the local, reference and total resistance coefficients K_T for each branch and branch section of the piping system.

Table 6:   Effective resistance coefficients for each piping branch.

C-D NOZZLE BRANCH

LOCAL K	REFERENCE K
-	$K_{AB}^{H} = 21.044$
$K_{BC}^{T} = 12132.27 \longrightarrow$	$K_{BC}^{H} = 758.27$
$K_{CD}^{F} = 5.872 \longrightarrow$	$K_{CD}^{H} = 8960$
TOTAL K	$K_{T} = 9739.31$

C-D NOZZLE BRANCH

LOCAL K	REFERENCE K
$K_{BE}^{T} = 3.36$	$K_{BE}^{H} = 0.21$
-	$K_{EF}^{H} = 5.76$
$K_{FG}^{90} = 12130 \longrightarrow$	$K_{FG}^{H} = 758.1$
$K_{GH}^{F} = 5.87 \longrightarrow$	$K_{GH}^{H} = 8960$
TOTAL K	$K_{T} = 9724.07$

Combining Eqn (44) and Eqn (45) the pressure drop across each piping branch can be calculated based on the average velocity of the reference pipe $\vec{V}_{H1} = 0.17178$ m/s and the two total resistance coefficients. The pressure drop across the nozzle branch is $\Delta P = 143695.57$ Pa and across the test-section branch is $\Delta P = 143470.72$ Pa.   These equate to 1.418 atm and 1.416 atm respectively. Since the liquid CO_2 is stored at over 57 atm, and the pressure drops are relatively small, liquid CO_2 is indeed issuing from the feed tubes as a liquid and then flashing to create dry ice particles.

Using Eqn (48) and the test section injection velocity and density of $\vec{V}_J = 3\,\text{m/s}$ and $\rho_J \cong 1000\,\text{kg/m}^3$ and the freestream velocity and density of $\vec{V}_\infty = 612\,\text{m/s}$ and $\rho_\infty \cong 0.0866\,\text{kg/m}^3$ the momentum flux ratio of the local test section cavity injector was calculated to be $\bar{q} = 0.277$. Compared with $\bar{q} \sim 30$, which is on the order of values typically associated with transverse jet injection, it was expected the jet would not penetrate very far into the supersonic freestream (above the cavity).

3. 1. 5   Experiment Variable Identification.

To conclude this chapter, Table 7 presents a summary of all test variables present during the experimentation along with the associated parameters affected by each variable. This is followed by Table 8 presenting all parameter intervals tested throughout all of the tests.

Table 7: Identified experiment variables and associated parameters affected.

SYSTEM	VARIABLE	AFFECTS
Wind Tunnel Air	stagnation pressure	air mass flow, particle sublimation rate & dispersion
CO_2 Piping	piping ID	flow state (laminar vs turbulent)
	piping length	pressure drop, flow state
	piping layout	CO_2 distribution, flow state
Shroud Injectors	feed tube ID	CO_2 mass flow
	feed tube length	pressure drop
	shroud tube ID	agglomeration rate, injection velocity & distance
	shroud tube length	agglomeration time
	shroud tube orifice	particle dispersion, injection distance
	feed/shroud overlap	shroud tube effective length
	penetration length	intrusiveness, injection distance
	tube material	heat transfer to CO_2
Intra-Cone Injector	cone cavity volume	agglomeration rate
Camera	height above laser plane	field of view, spatial resolution, scale factor
	f-stop	light intensity
	filter	light intensity
	camera timing	image quality
Laser	pulse separation	apparent particle distance traveled
	distance from TS wall	light intensity
	sheet thickness	light intensity, out of plane motion correction
	sheet orientation	light intensity

93

Table 8:   Variable intervals tested.

VARIABLES	TESTS INTERVAL
Stagnation Pressure	25 psia to 39 psia
Air Mass Flow Rate	0.426 kg/s to 0.664 kg/s
CO_2 Mass Flow Rate	0.00136 kg/s
Shroud Injectors	
Feed Tube ID	0.01 in. to 0.03 in.
Feed Tube Length	55 mm to 130 mm
Shroud Tube ID	1/16 in. and 3/16 in.
Shroud Tube Length	35 mm and 190 mm
Feed/Shroud Overlap	10 mm
Penetration Length	3/4 in.
Camera	
f-stop	4 to 8
Scale Factor	3.652 to 4.170
Laser	
Pulse Separation	1 μs
Distance from Test Section	4 cm to 11 cm
Sheet thickness	1 mm to 3 mm

3. 2   Experimental Procedure

3. 2. 1   *PIV Testing.*

Each supersonic wind tunnel test that was performed followed the same procedure regardless of the test model being examined or the number of injectors employed. The three major components of each test were: (1) running the wind tunnel, (2) injecting the carbon dioxide, and (3) capturing the PIV data. After each test the collected image pairs were analyzed. This consisted of evaluating the image maps to determine there usability with the PIV technique and, where appropriate, applying PIV correlations to good data sets to produce vector maps representative of the flow observed.

Running the wind tunnel involved preparing the main air supply, the control air supply, the PIV equipment, and the wind tunnel equipment. A detailed user's manual for the AFIT supersonic wind tunnel is contained in Appendix H.   Preparing the CO_2 injection system included setting up the piping scheme before each run to get the injectant from the high-pressure tank to the wind tunnel. The injection system was kept simple so generally only minor adjustments were necessary. Capturing good PIV data required a good test sequence and proper planning. Proper planning refers to taking appropriate measures to prevent excessive laser reflections off the test models and reflective surfaces; also proper alignment of the laser sheet in the camera object plane.

The best timing sequence was found to be starting the wind tunnel using the LabView virtual instrument (VI) shown in Figure 38 while simultaneously opening the CO_2 tank valve manually.
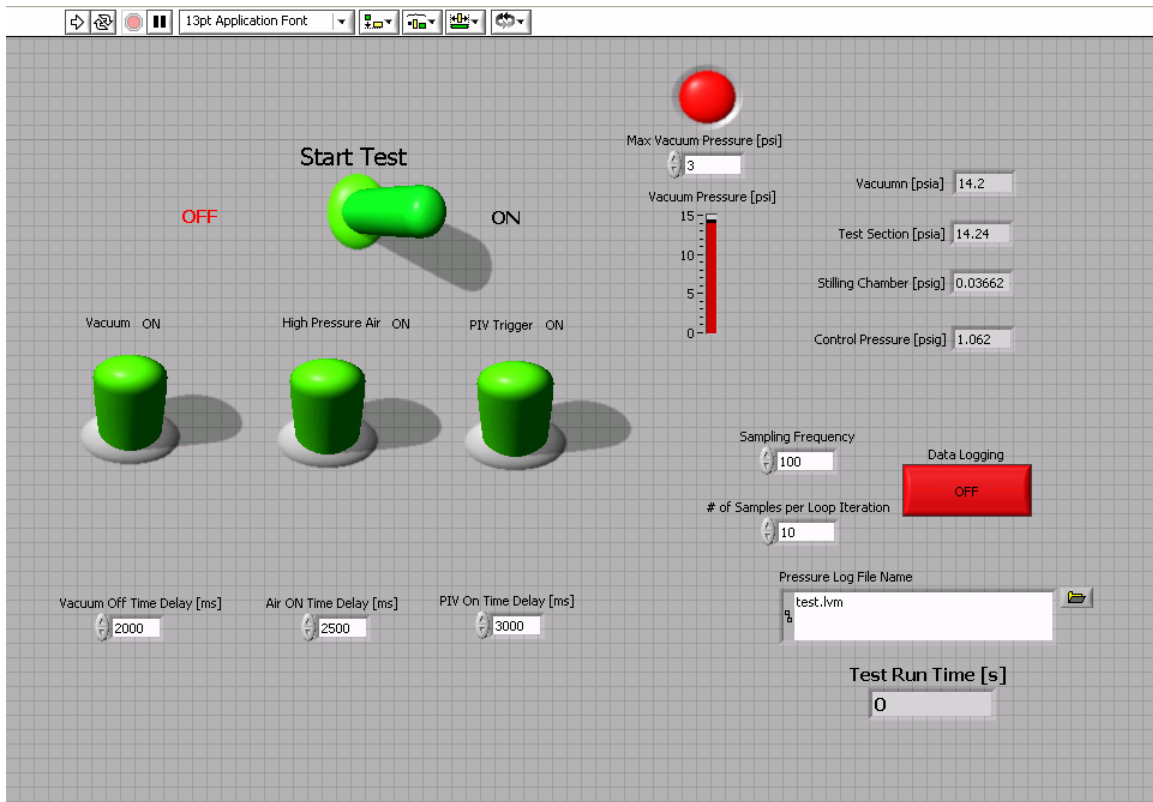
Figure 38: LabView virtual instrument used to run tests.

The air flow and CO_2 flow we simultaneously started and allowed to reach steady state, which required approximately seven seconds. After a preprogrammed time delay of seven seconds (adjustable in the VI) the LabView VI would then automatically trigger the Dantec FlowManager Hub to begin collecting data (firing the laser and camera). Additionally, the VI was programmed to output and record the pressures being measured by all transducers associated with the wind tunnel for later reference. The VI would then

stop the wind tunnel when a specified maximum vacuum pressure was reached. All the LabView graphical code used to control the wind tunnel is contained in Appendix I. This system was found to be very robust except for the abnormal pressure fluctuations would occur within the control pressure lines. For no apparent reason the control pressure (which regulated the stagnation pressure) would begin to drop, effectively un-starting the wind tunnel.

Many PIV tests were performed but only the best runs will be discussed in the next chapter. However, the motivations behind each successive test parameter change and the results achieved or knowledge built from each tests performed is presented for comparison in Table 9.

Table 9:   Tests objectives, parameters, and successive setup changes.

TEST	MODEL	OBJECTIVES	C.P.	INJECTION	LASER ORIENTATION		F-STOP	RESULTS
					From TS Wall	**Model Location**		
28-Feb	cavity	perform first test, learn the system	38 psia	20 NZ + 20 TS	4 cm	3 cm above cavity floor	4	laser intensity too high; 20 good image map (IM) pairs
21-Mar	cavity	see effect of larger feed tube, back off laser to reduce laser intensity	38 psia	30 NZ + 20 TS	11 cm	3 cm above cavity floor	4	test section is overexposed; 20 good IM
27-Mar	cavity	reduce overexposure in TS using smaller feed tube	38 psia	20 NZ + 10 TS	11 cm	3 cm above cavity floor	4	can't use 10/1000"; 20 good IM
3-Apr	cavity	try new sequence of events to get more usable IM	38 psia	20 NZ + 20 TS	11 cm	3 cm above cavity floor	4	56 good IM
3-Apr	cavity	inspect flow down in cavity	38 psia	20 NZ + 20 TS	11 cm	1.3 cm above cavity floor	4	compressor problems reduce run time; 19 good IM
4-Apr	forward cone	attempt cone injection and longer run time (more data)	25 psia	20 NZ + 20 TS	11 cm	mid-cone	4	cone plume is overexposed; 60 IM
4-Apr	forward cone	reduce overexposed plume with higher f-stop	25 psia	20 NZ + 20 TS	11 cm	mid-cone	11	cone plume better but still overexposed; 60 good IM
4-Apr	forward cone	reduce overexposed plume with higher air mass flow rate	37 psia	20 NZ + 20 TS	11 cm	mid-cone	4	cone plume thinned out but still overexposed; CP phenomena reduces run time; 36 IM

NOTE: TS = Test Section   10 = 10/1000" feed tube

NZ = Nozzle   20 = 20/1000" feed tube

SC = Stagnation Chamber   30 = 30/1000" feed tube

IM = Image Map Pair

CP = Control Pressure

Table 9   (continued)

TEST	MODEL	OBJECTIVES	C.P.	INJECTION	LASER ORIENTATION		F-STOP	RESULTS
					From TS Wall	Model Location		
4-Apr	forward cone	use single NZ injection to visualize cone flow	25 psia	20 NZ	11 cm	mid-cone	4	60 good IM
10-Apr	combination cone	first test performed with new lab partner; practice run.	29 psia	20 NZ	11 cm	below cone	4	need to practice sequence; 37 IM
10-Apr	combination cone	perform better test	27 psia	20 NZ	11 cm	below cone	4	75 good IM
10-Apr	combination cone	inspect flow at mid-cone	27 psia	20 NZ	11 cm	mid-cone	4	75 IM
10-Apr	combination cone	perform better test	27 psia	20 NZ	11 cm	mid-cone	4	75 good IM
11-May	Empty Test Section	gather baseline data	25 psia	20 NZ	11 cm	mid-plane	8	75 IM
11-May	Empty Test Section	gather baseline data	25 psia	20 NZ	11 cm	mid-plane	8	75 IM
11-May	Empty Test Section	attempt stagnation chamber injection	25 psia	20 SC	11 cm	mid-plane	5.6	75 IM

NOTE: TS = Test Section   10 = 10/1000" feed tube
NZ = Nozzle   20 = 20/1000" feed tube
SC = Stagnation Chamber   30 = 30/1000" feed tube
IM = Image Map Pair
CP = Control Pressure

99

3. 2. 2   Post Processing.

Quality images were analyzed using the PIV correlations described in section 2. 4. 5. To reduce computation time and prevent velocity calculations for areas obviously out of the flow field, portions of the image maps containing wind tunnel side walls were not considered and labeled as inactive image map regions. Additionally, pieces of the test models captured in the images were *masked* out, or neglected, by manually cordoning off regions of the image map (IM). Once the images were prepared for processing, four different PIV correlation schemes were applied to each IM pair for comparison. These correlations included two different cross correlations, an average correlation and an adaptive correlation. All of the correlations employed a 50% IR overlap. Due to the long processing times, an initial interrogation region (IR) size of 256x256 was utilized for the adaptive technique except for the best PIV image map pairs, which were processed using an initial IR size of 512x512. For each correlation chain, a moving average validation was performed on each raw vector map produced. This was followed by a range validation to create a final vector map for each IM pair. Though this range validation was not entirely necessary, it was the only way to discard the vector place holders (dots) from the vector maps. Figure 39 shows this validation sequence for the best test run, which is discussed in section 4. 3. 4. All tests were analyzed following identical procedures.

Raw Adaptive Vector Map   **Moving Average Validation**
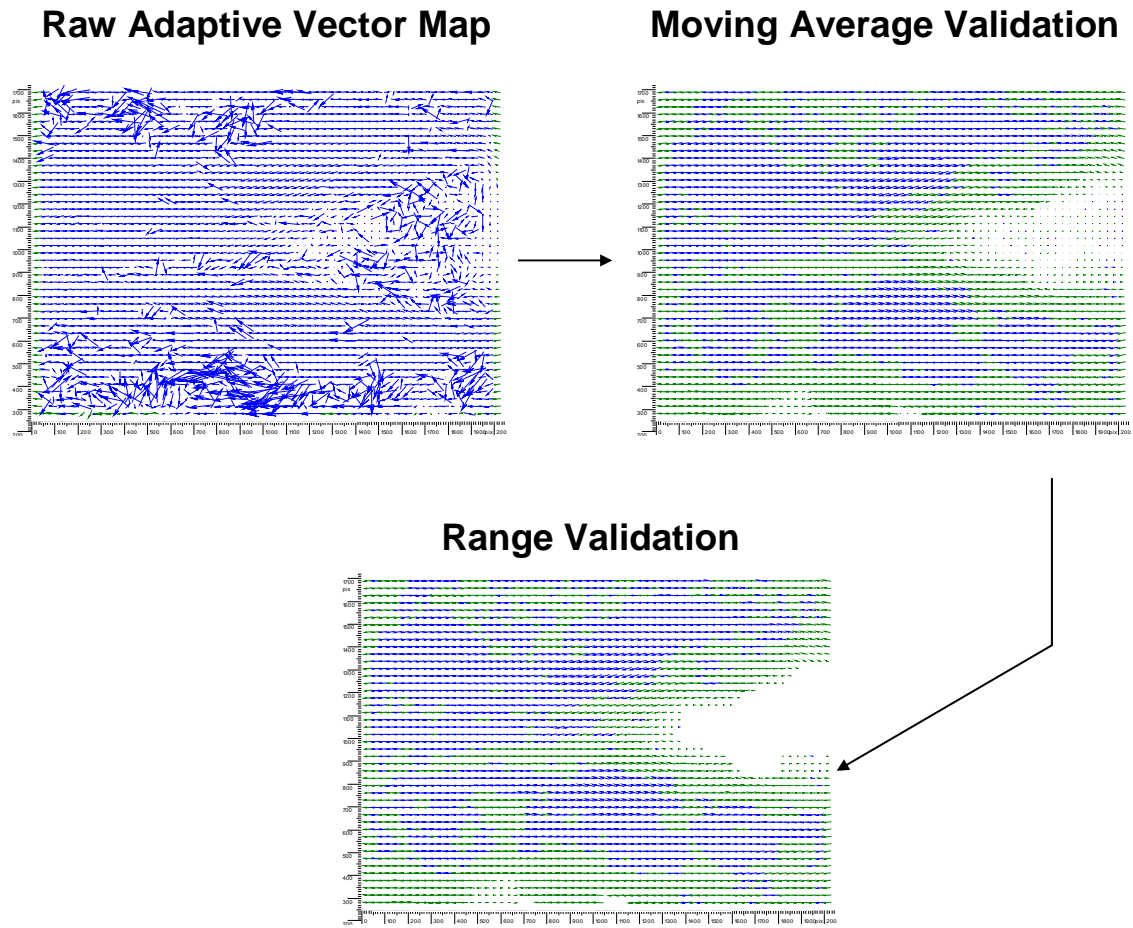
Range Validation

Figure 39: Raw vector map validation sequence.

Lastly, statistical averages were computed for the cross and adaptive correlations using every range validated vector map in the test run. At the end of this process there were four final vector maps for each test run. Once the final four vector maps were obtained (cross 64 statistic, cross 128 statistic, adaptive statistic and average statistic) they were compared. The adaptive post-processing recipe produced the best vector map, based on corresponding flow features revealed by the vector map matching up agreeably with theory. Figure 40 shows all four final vector maps for the best test run (section 4. 3. 4).

CROSS 128

CROSS 64

ADAPTIVE

AVERAGE
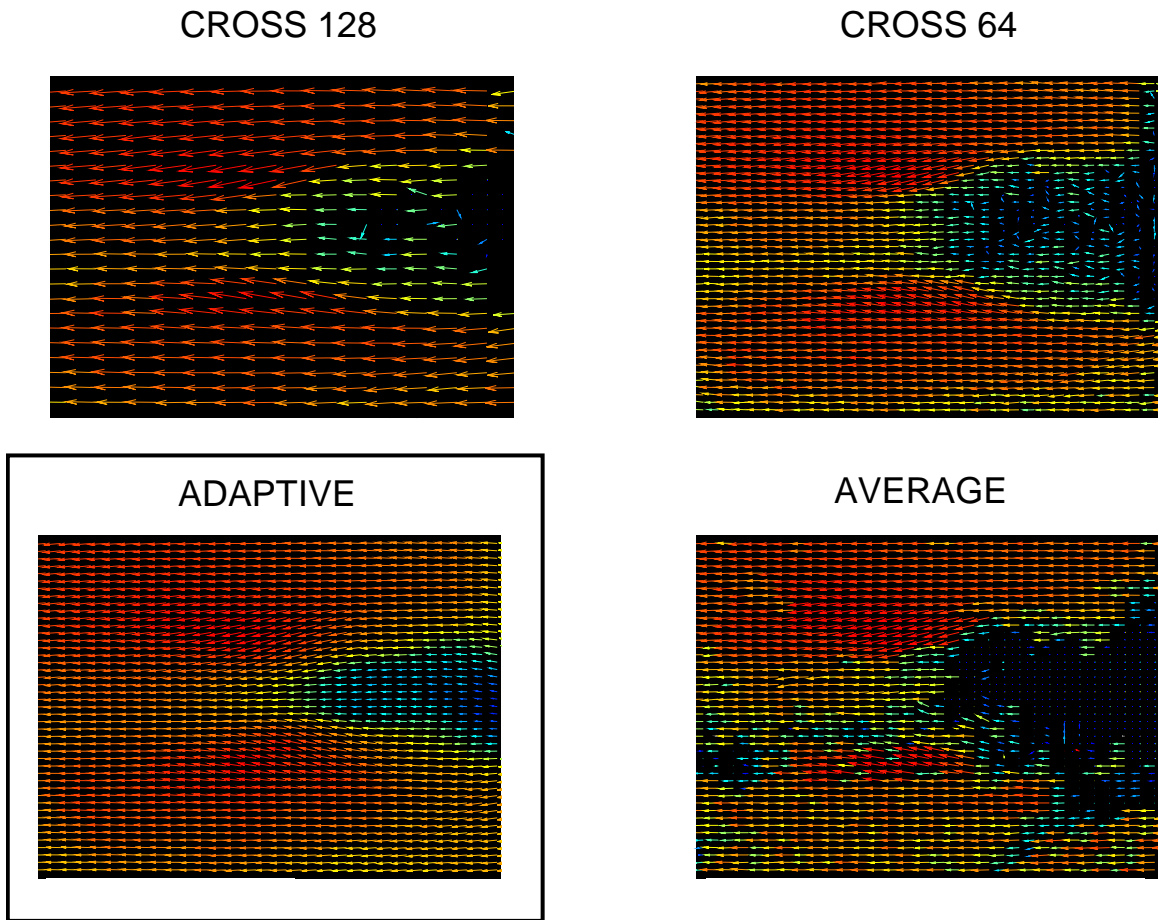
Figure 40: Final vector map comparison.

Table 10 provides the recipe used for each PIV correlation mentioned above. Graphical

reference screen shots showing the post-processing steps are included in Appendix J.

Table 10:   Dantec FlowManager PIV correlation recipes.

Correlation	Initial IR	Final IR	Overlap
cross	128	128	50%
cross	64	64	50%
adaptive	256 or 512	64	50%
average	64	64	50%

NOTE: for adaptive, 2 passes/step
        average performed on all IM at once

Moving Average	Averaging Area	Acceptance	Iterations
cross 128	5x5	0.1	5
cross 64	5x5	0.1	5
adaptive	7x7	0.01	5
average	7x7	0.2	1

NOTE: substitute invalidated vectors
        validate along boundary

Range Validation	Type	Min	Max
cavity	length	10	800
cone	length	100	800

3. 2. 3   Vector Map Development and Presentation.

To display the final vector maps effectively, two different styles of data presentation were developed to convey the information embedded within the image as clearly as possible. The first figure is called a *vector map overlay* and consist of a feather plot (Dantec, 2002:8-63) overlaid atop the best image of the seed particle distribution. To create this type of figure find the best image for a particular run. Then right click the image and display the *List of Layers* window. Now click and drag the statistical vector map you wish to overlay from the setup branch into the list of layers. Next select the *Display Options* for the overlaid vector map and choose the following: (1) an auto-scaling factor of 40 and an arrow head size of 7 from the *Scaling* tab (2) the rainbow color scheme under *color vectors* from the *Colors* tab (3) tail point alignment and show every 6 (x) and 1 (y) vector from the *Advanced* tab.

The second figure style is called a *vectored color map* and consists of a vector map overlaid atop a color contour map. To create this type of figure choose the best final vector map and create a color map from it (new dataset – plots – color map) shaded with the rainbow color scheme. Follow the steps in the paragraph above to layer the same vector map atop the color map. Next select the *Display Options* for the overlaid vector map and choose the following: (1) auto-scaling factor of 20 (2) hide all vectors but normal and substituted under the *Colors* tab and change the vector color to black (3) tail point alignment and show every 3 (x) and 1 (y) vector from the *Advanced* tab. For graphical reference, screen shots showing the steps for post-processing correlation and data presentation are included in Appendix K.

4. Results and Analysis

4. 1 Test Section Characterization

The first series of tests provided an experimental baseline. Using the shroud injector described in section 3. 1. 3, single injection flow was imaged at the empty test section mid-plane in two separate tests. For the first test CO_2 particles were introduced into the flow at the nozzle injection point. In the second test, the CO_2 particles were introduced into the flow at the stagnation chamber, upstream of the nozzle entrance. The particle distribution densities for the first test were better than those from the second test. This was expected because the particles introduced into the flow at the stagnation chamber had more time to sublimate. As seen in Figure 42, this also accounts for the greater amounts of CO_2 condensate, or vapor; stream tubes of vapor are created as the particles partially sublime along their flow path through the test section.

Good image map pairs from both runs are presented in Figure 41 and Figure 42, with the airflow going from right to left at Mach 2.9. The brightness dissimilarity between Figure 41 and Figure 42 is not representative of any error; manually increasing the grey level brightness merely helped to accentuate the vapor streams in the second image pair. Additionally the higher intensity of the second laser pulse can be seen in the second frame of Figure 41 and Figure 42. Seventy-five image pairs were correlated for each test and are presented as vectored color maps in Figure 43 and Figure 44. Erroneous regions of low velocities are seen at the bottom of Figure 43. These regions correspond

to screw reflections. Due to the averaging validation these noisy areas of low velocities may have scaled down all of the velocities lower in the image. This may have contributed to the skewed velocity profile from top to bottom.
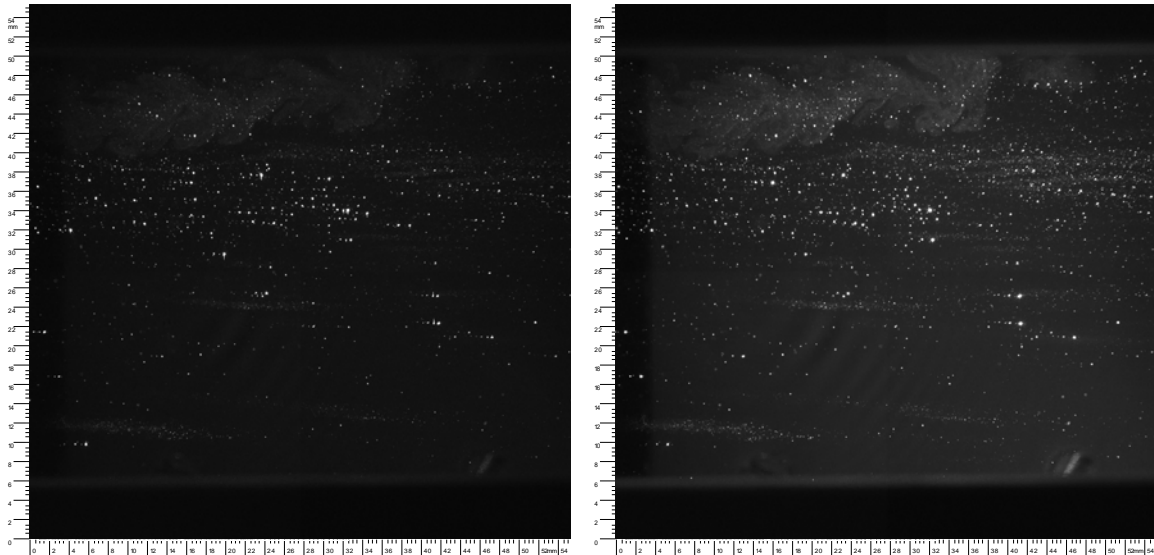
Figure 41: Nozzle injection imaged mid-test section.
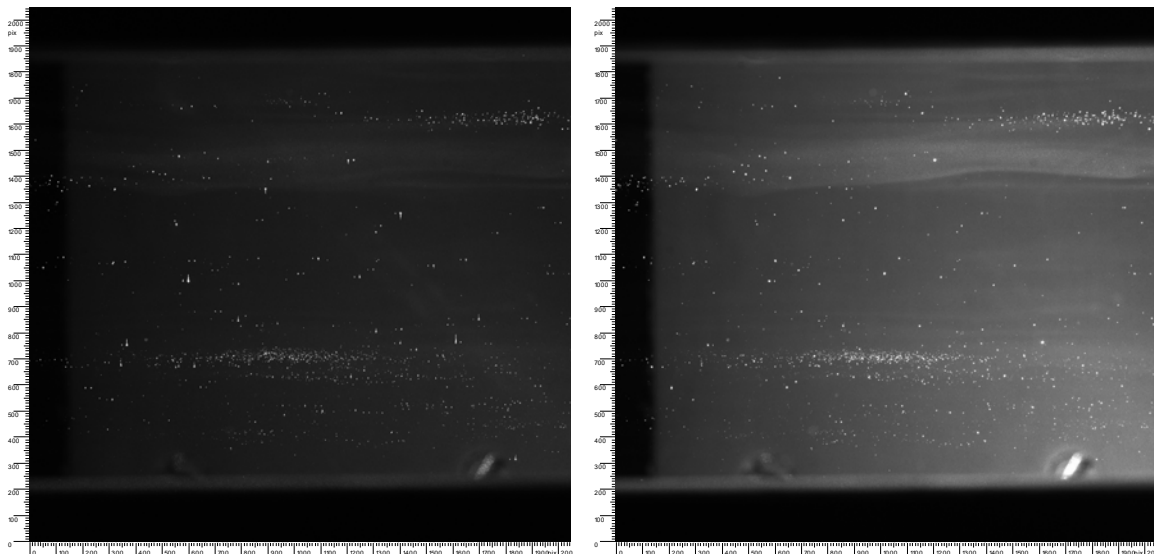
Figure 42: Stagnation chamber injection imaged mid-test section.

Table 11: Values for nozzle injection imaged mid-test section.

Test Date	11-May (tst1)	Rejected Vectors	0
Setup	empty	Substituted Vectors	905
Injection	20/N	Total Vectors	3087
IM Pairs Correlated	75	Average Velocity	501 m/s
Scale Factor	3.652	Standard Deviation	79 m/s
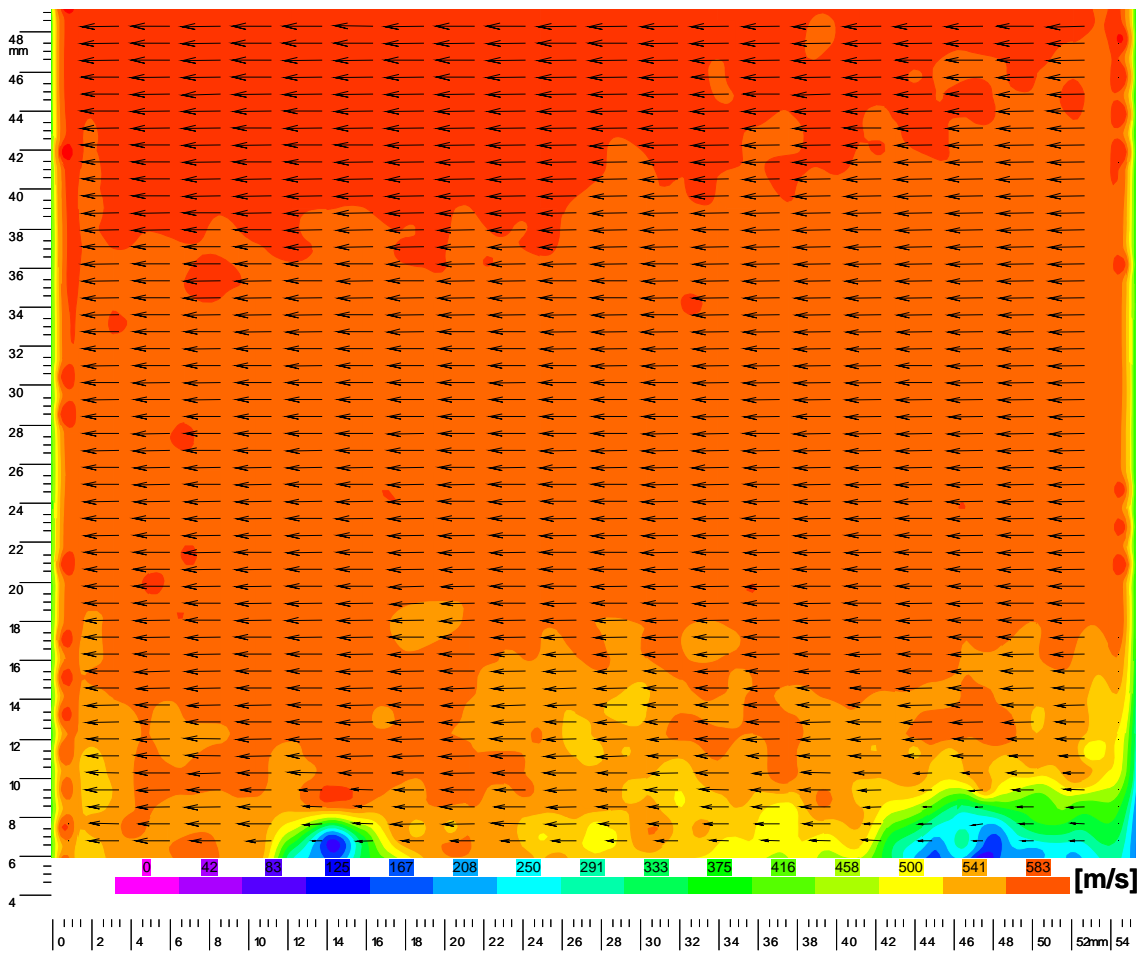
Figure 43: Vectored color map for nozzle injection imaged mid-test.

Table 12: Values for stagnation chamber injection imaged mid-test section.

Test Date	11-May (tst2)	**Rejected Vectors**	0
Setup	empty	**Substituted Vectors**	1511
Injection	20/S	**Total Vectors**	3087
IM Pairs Correlated	75	**Average Velocity**	306 m/s
Scale Factor	3.652	**Standard Deviation**	122 m/s
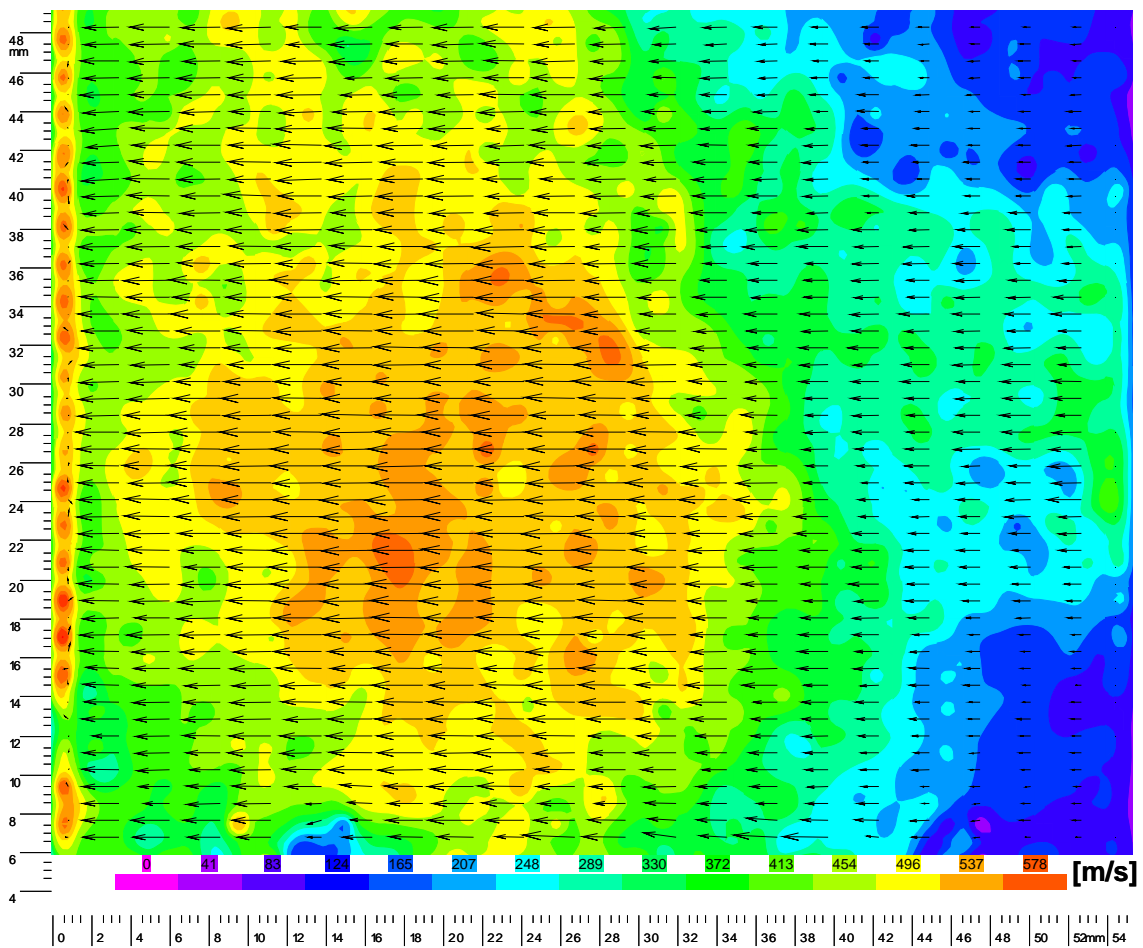
Figure 44: Vectored color map for stagnation injection imaged mid-test.

Figure 43 shows a relatively one dimensional flow field with a majority of the velocities near 583 m/s, which are within 5% of the theoretically calculated freestream velocity of 610 m/s. This marks a trend seen throughout the results obtained in this paper. Most of the measured velocities fall short of those predicted by theory. Additionally the measured velocities are noticeable higher at the top edge of the vector field and decrease steadily towards the bottom of the vector images. Lastly, by tracing the dark regions in the upper and lower portions of the images in Figure 41 and Figure 42, which are the edges of the test section, it is seen that the images are not perfectly aligned with the horizontal direction. Most of the images captured will have some bias based on the angle between the camera horizontal and the streamwise flow direction. This has no effect on the measured velocity magnitudes, merely on the *u* (stream wise) and *v* (span wise) components of velocity.

The stream wise velocity profile (x-velocity) and span wise velocity profile (y-component) were plotted versus the span wise direction (y-direction) at the x = 20 mm station seen in Figure 43. The stream wise velocity component steadily drops from 585 m/s in the upper field to 400 m/s in the lower field as shown in Figure 45. Likewise, the span wise velocity component is observed to be everywhere negative, signifying the camera was at a slight angle to the test section causing the flow in the raw image maps to have a left downward bias. Moving from the top of the vector field to the bottom the span wise velocity fluctuations appear to amplify in magnitude, as seen in Figure 45.
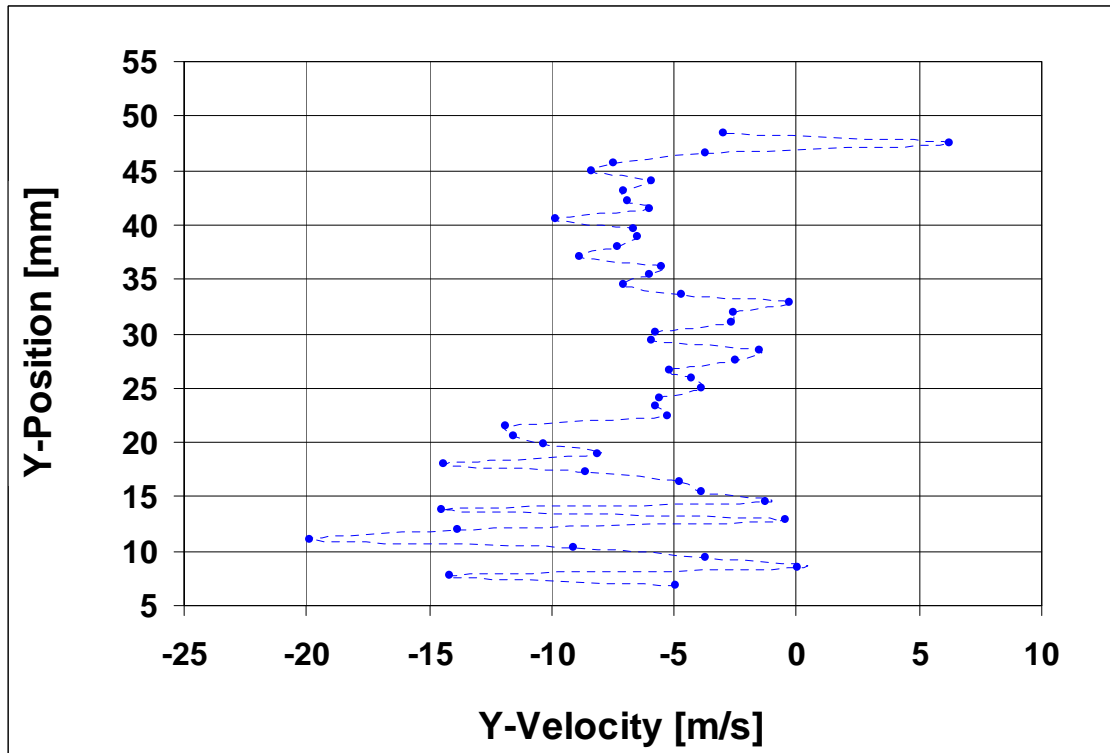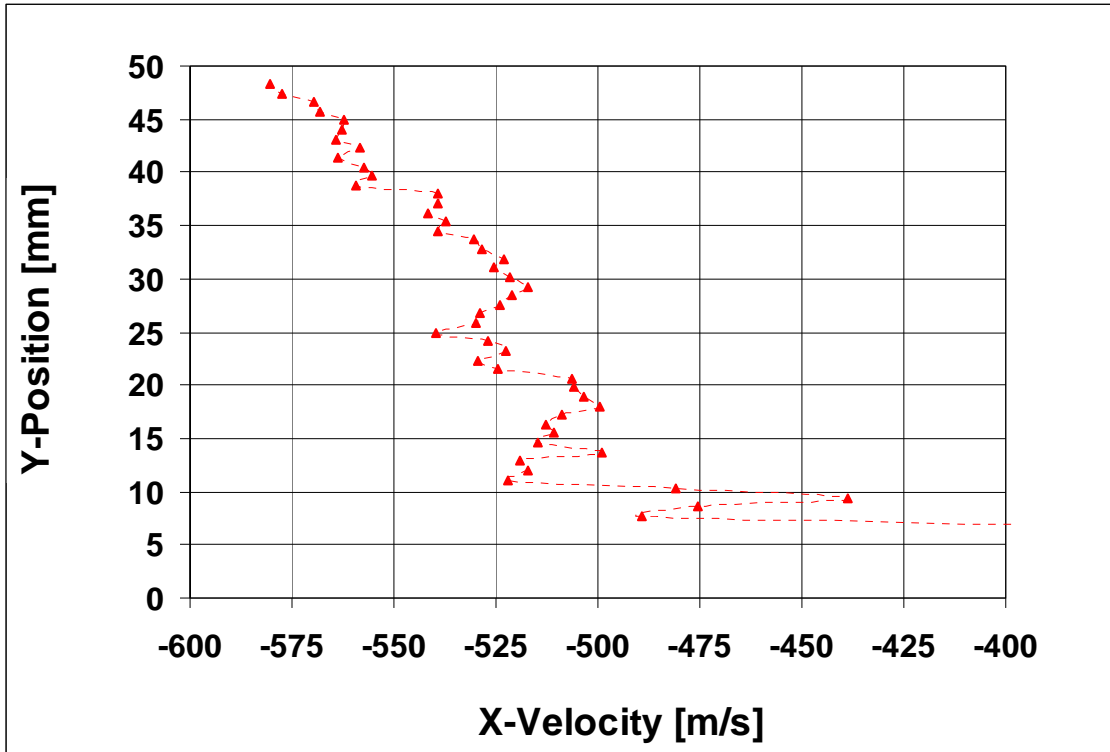
Figure 45: Velocity profiles across the empty test section.

Figure 44 shows a one-dimensional flow of non-uniform velocities inconsistent with the flow field predicted from compressible gas flow theory and with the data in Figure 43. A plausible explanation is the increased background light levels caused by low intensity Rayleigh scattering from CO_2 condensate and rarified particle densities may have prevented proper correlation. Additional filtering may have improved the vector map fidelity but it was desired to keep a consistent correlation recipe for all results in this paper.

Lastly, the actual image maps obtained using stagnation chamber injection appear more suitable for PIV correlation than those obtained by McNiel (2007). This could possibly be due to the longer effective shroud tube employed and a lower air mass flow rate.

4. 2   Sources of Error

Many unavoidable sources of error are introduced during experimentation, and the impact of each source on the results must be assessed. It is difficult to numerically quantify all sources of error present during a wind tunnel experiment. Nonetheless, all identifiable sources of error should be considered to qualify confidence in the results presented.

One important source of error is particle bleed over from image 1 to image 2. This is noticeable when extremely bright particles in one image are seen in the same location on both images. This false particle duplication lowers the measured velocities because some particles appear stationary and contributes to apparent particle drop out. As mentioned earlier, this may have been caused by not allowing the full 12 ms transfer time recommended by Redlake between frame 1 and frame 2.

Systematic improvements could be made by making the laser sheet profile, which resembled a long triangle rather than a narrow slit, more uniform. Also, reducing differences in laser pulse intensity between laser pulse 1 and pulse 2 would help. This problem is clearly seen by the overall higher intensity in the second image frame when compared to the first frame in the following sections. These two errors may contribute to the apparent velocity decrease from top to bottom of the vector maps as well as increasing particle drop out due to out of plane motion.

The camera scale factor, which has a direct influence on measured velocities, is very sensitive to laser sheet location. The camera scale factor was measured at one distance from the lens (the intended illumination plane). However the actual light sheet had a finite thickness of ~3 mm. Additionally the laser sheet uncertainties described above could have slightly offset the actual plane of illumination. These disconnects could have shifted the measured velocities by a small amount.

Stray laser energy reflected by lab equipment had a minor influence due to proper preventative steps taken during the experimental setup. However, some reflection errors are present in the results. For example, reflective screw heads were clearly connected to circular regions of noise in the previous section. Furthermore, large dry ice pellets and dense groups of CO_2 particles had the same affect as the reflective screw heads, causing localized overexposures. Additionally, stream tubes containing high concentrations of CO_2 condensate reduced the local signal to noise ratio in some regions by increasing the local brightness of the image background.

Some facility shortfalls have a small influence on flow properties. The final air filter was saturated with rust colored water, which would accumulate and had to be drained prior to each set of runs. Additionally, after approximately 15 seconds the control pressure would decrease rapidly during each test. A typical pressure drop ranged from 25psia to 20psia over a time span of 5 seconds, or 1psia per second. This would cause the stagnation pressure to vary, which in turn would cause the mass flow rate and wind tunnel pressures to shift, making the flow unsteady. Fortunately, the stagnation temperature, Mach number, and therefore the flow velocity were not affected.

113

Some assumptions must be made to employ the isentropic, shock wave and expansion equations used to compute velocity values for comparison. The flow throughout a wind tunnel is neither isentropic nor adiabatic due to viscosity, heat transfer, shock waves and wind tunnel surface irregularities.

The small level of intrusiveness caused by introducing CO_2 is predicted below. The overall influence of increasing CO_2 concentrations in the media mixture is to reduce the local speed of sound by two mechanisms. The first is a reduction in the specific heat ratio and the second is a reduction in local flow temperature. Both of these effects combine to reduce the local flow velocity. The stagnation temperature was measured at the nozzle injection point both with and without CO_2 injection. Then a mixture specific heat ratio was calculated assuming all of the CO_2 introduced was in gaseous form. The calculations below indicate the introduction of carbon dioxide into the flow reduces the predicted freestream velocity by 1 m/s. This statement reassures using carbon dioxide to seed a supersonic flow has little effect on the flow parameters. Even though solid CO_2 is present and does have a higher specific heat, its effect on the main media velocity would most certainly be insignificant.

<u>Wind Tunnel Run - Air Only</u>

Initially assuming $\gamma = 1.4$ a test section $T = 110\,\text{K}$ was calculated from a $T_O = 295\,\text{K}$

$C_p = 1030\,\text{J/kg-K}$ for air near 100 K

$\hat{m}_{air} = 29$

$R = 286.7\,\text{J/kg-K}$ for air [Eqn (3)]

$\gamma = 1.387$ for air near 100 K [Eqn (7)]

$T_O/T = 2.627$ at Mach 2.9 [Eqn (16)]

Using the measured stagnation temperature during air only flow,

$T_O = 293.71\,\text{K}$ (no injection)

$T = 111.8\,\text{K}$

$a = 210.8\,\text{m/s}$ [Eqn (23)]

The empty test section freestream velocity on the air is predicted,

$\vec{V} = 611.5\,\text{m/s}$ [Eqn (1)]

Wind Tunnel Run - Air with CO_2 Injected

Using mass flow rates to find the mass fractions of the constituents,

$\dot{m}_{CO_2} = 0.00136\,\text{kg/s}$

$\dot{m}_{air} = 0.426\,\text{kg/s}$

$\dot{m}_{ttotal} = 0.42736\,\text{kg/s}$

$\dot{m}_{CO_2}/\dot{m}_{total} = 0.3\%$

$\dot{m}_{air}/\dot{m}_{total} = 99.7\%$

The mixture properties can be found,

$\hat{m}_{mixture} = 29.05$ [Eqn (8)]

$R_{mixture} = 286.21\,\text{J/kg-K}$ for air/CO_2 mixture [Eqn (3)]

$C_p = 650\,\text{J/kg-K}$ for CO_2 near 100 K

$C_{p,mixture} = 1028.8$ J/kg-K for air/CO_2 mixture near 100 K [Eqn (9)]

$\gamma = 1.3854$ for air/CO_2 mixture near 100 K [Eqn (7)]

$T_O/T = 2.6206$ at Mach 2.9 [Eqn (16)]

Using the measured stagnation temperature during injection,

$T_O = 292.87$ K (with injection)

$T = 111.75\,\text{K}$

$a = 210.5\,\text{m/s}$ [Eqn (23)]

The empty test section freestream velocity on the air/CO_2 mixture is predicted,

$\bar{V} = 610.46\,\text{m/s}$ [Eqn (1)]

4. 3   Generated Vector Maps and Associated Data

The size of the carbon dioxide particles passing through the test section were not directly measured during any of the wind tunnel tests. However, visual inspection of the image maps using a pixel count and the metric rulers attached to the picture frame indicated an upper limit on particle size of approximately 500 μm. Auspiciously a majority of the particles present (≈95%) were much smaller, which is desirable.

As mentioned in section 3. 2. 2 the adaptive correlation produced the highest quality vector maps. All of the final results presented below utilized the adaptive correlation with a final interrogation region area of 64 x 64 pixels and an overlap of 50%. Only one of the tests was correlated using an initial IR area of 512 x 512 pixels (section 4. 3. 4), all others used an initial IR of 256 x 256 pixels.

A table will be presented for each test run giving important values. To minimize duplication, other values of interest not included locally can be found in Table 9 on page 98. Additionally, refer to section 3. 1. 3 to see the experimental setup for each test.

It is important to note the average and standard deviation velocities presented for each case are for the entire vector field. Vectors within unreliable areas of the vector maps are included in these values and tended to decrease the values significantly.

4. 3. 1   Above Cavity, Dual Injection.

For the second set of tests, the CO_2 particles were illuminated 3.0 cm above the cavity floor (1.25 cm above the test section floor) during dual cavity/nozzle injection. The local seed distribution is seen highly concentrated around the cavity injection port with a free stream seed distribution that is more spread out. Although Figure 46 does not clearly show particles present in the free stream, there was indeed a significant number of particles present in most images, mostly appearing in the top of the image pairs collected.
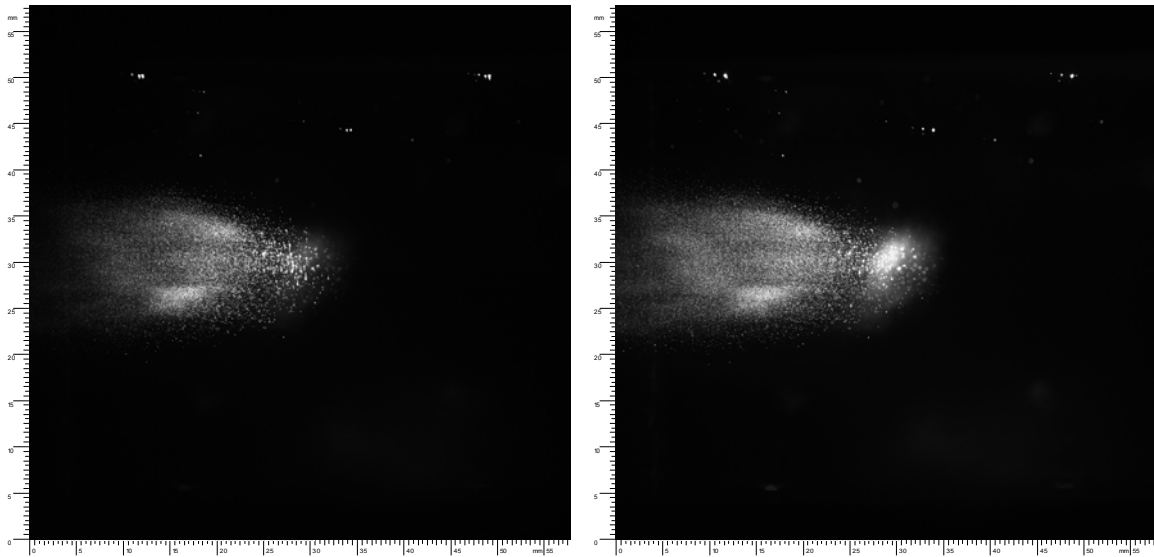
Figure 46: Dual injection imaged 3 cm above cavity floor.

The high free stream particle location suggest a shallow CO_2 jet penetration distance in the nozzle, leaving a majority of the particles introduced upstream close to the inner nozzle wall. Additionally, because particles injected through the cavity are clearly seen in the images it can be stated the CO_2 jet penetrated at least up to the illumination plane. This is supported by Figure 47 taken during an experimental setup run.

118
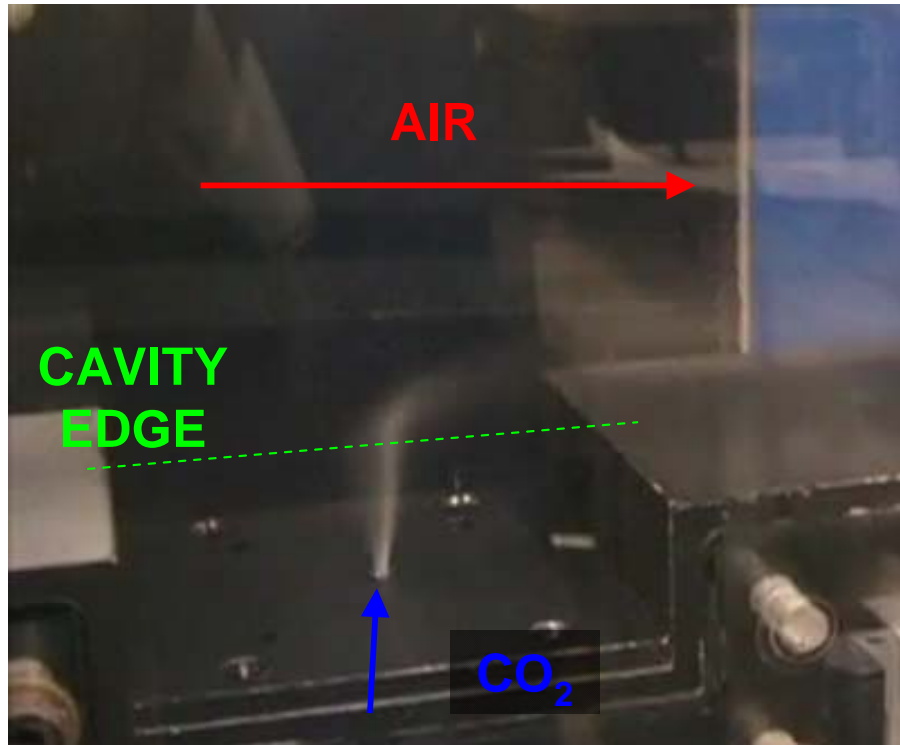
Figure 47: Cavity injection penetrating into supersonic cross flow.

Figure 48 is the vectored color map produced to display the results of this section. In the center of the figure the color map displays zero velocity because the jet is issuing directly out of the paper (and the images were overexposed due to high particle concentration). Moving left of center, the ligament and droplet regions of the jet plume are seen accelerating from 0 m/s to velocities of 533 m/s over a distance of 32 mm. The particles most likely equalized with the higher velocity freestream flow further downstream. The jet plume boundary is easily identified and is observed to be slightly expanding in width. The apparently random velocity perturbations, signified by circular dots of low velocities (spotted tie-dye pattern), may be created by the highly unsteady cavity flow. Pressure waves reflecting back and forth in the cavity transmit disturbances through the cavity shear layer, which would cause velocity fluctuations.

Table 13: Values for dual injection imaged 3 cm above cavity.

Test Date	3-Apr (tst1)	Rejected Vectors	1972
Setup	above cavity	Substituted Vectors	2451
Injection	20/N + 20/T	Total Vectors	3276
IM Pairs Correlated	56	Average Velocity	428 m/s
Scale Factor	3.816	Standard Deviation	109 m/s
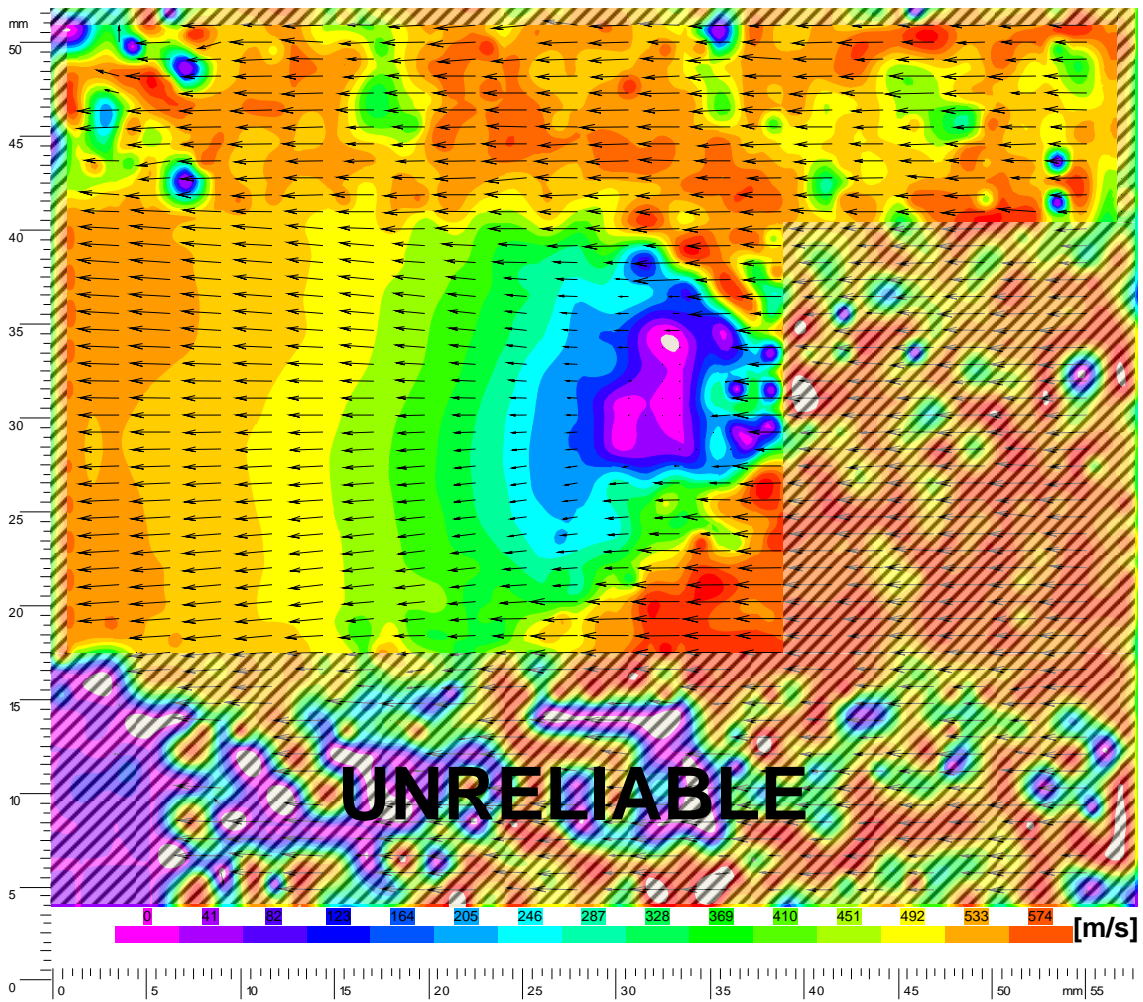
Figure 48: Vectored color map for dual injection imaged 3 cm above cavity.

Along the figure boundaries and in regions of the flow field with consistently sparse particle numbers (directly upstream of the transverse injection port and lower in the picture) the velocities computed most likely did not originate from actual particles, but instead are probably interpolated substitutions obtained by averaging adjacent interrogation regions. Therefore these areas have been cordoned off and marked as *UNRELIABLE*, signifying the high probability the information contained there is incorrect. For future work, it would be helpful if a particle density distribution function was used to yield a confidence level for different portions of the vector map.

4. 3. 2   Lower Cavity, Dual Injection.

For the final cavity test CO_2 particles were illuminated 1.3 cm above the cavity floor during dual cavity/nozzle injection. The particle distribution was similar to the second test, as seen in Figure 49; however, due to recirculation a few particles did find their way upstream of the transverse injection port. The jet plume is quite wide and separated into two distinct branches. A vortex is predicted to exist downstream of the jet by both cavity flow theory and transverse injection theory. This vortex may have enhanced the flow bifurcation and dispersion. Finally, laser light reflecting off the black screw heads introduced error into the PIV correlations. Additionally the circular saturated region in the center of the images was masked out during processing (neglected) to prevent velocity biasing during the moving average validation. In addition to the vectored color map shown in Figure 50, a vector map overlay is also shown in Figure 51 to help highlight the flow field motion.
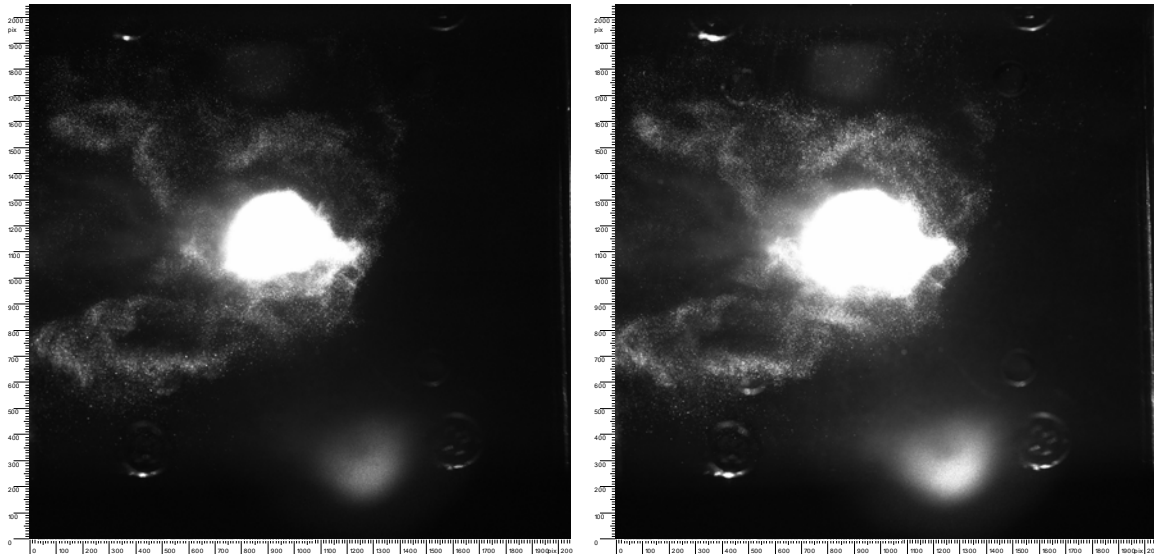
Figure 49: Dual injection imaged 1.3 cm above cavity floor.

Table 14: Values for dual injection imaged 1.3 cm above cavity floor.

Test Date	3-Apr (tst2)	Rejected Vectors	694
Setup	lower cavity	Substituted Vectors	1680
Injection	20/N + 20/T	Total Vectors	3528
IM Pairs Correlated	19	Average Velocity	55 m/s
Scale Factor	3.979	Standard Deviation	44 m/s
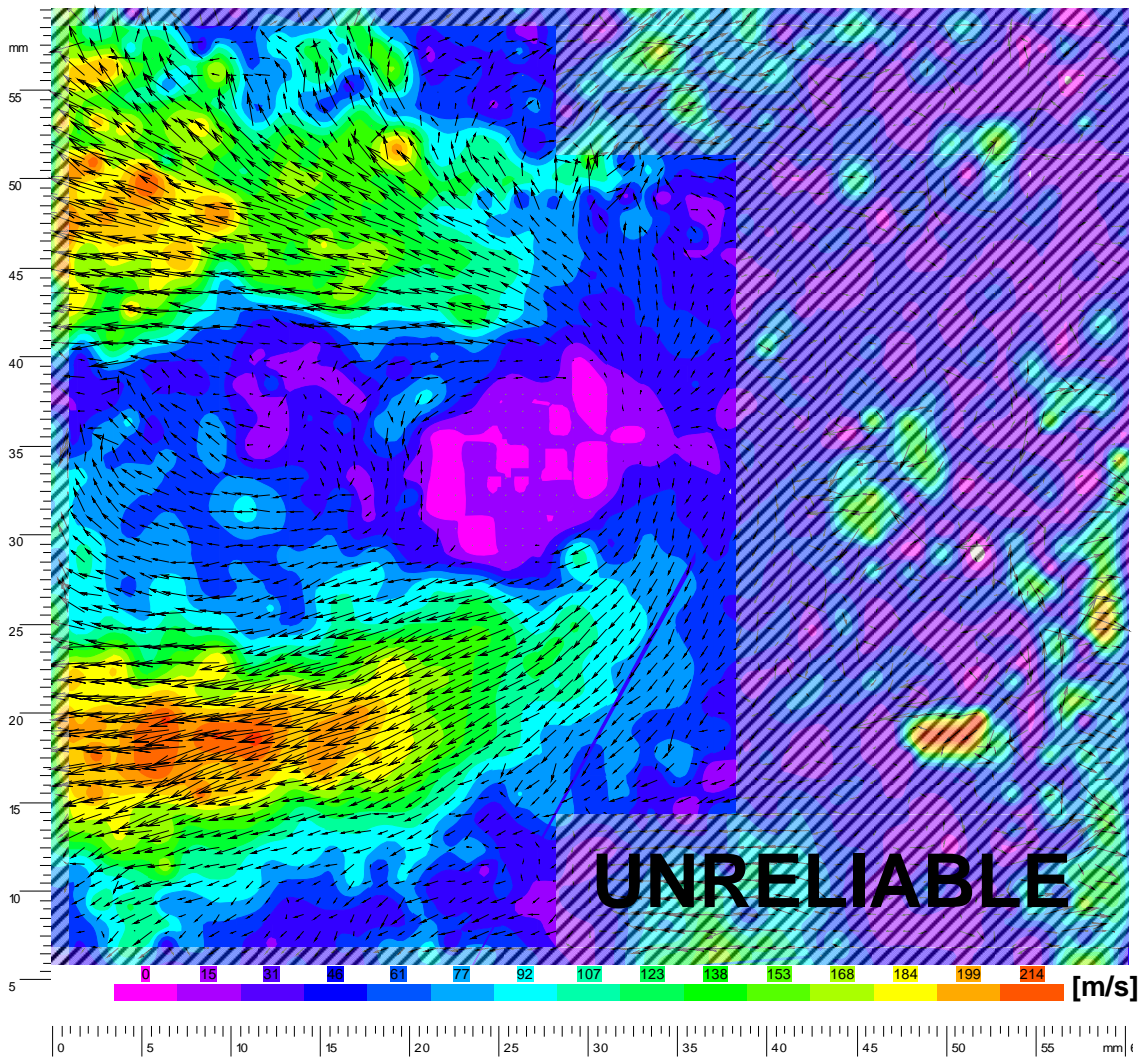
Figure 50: Vectored color map for dual injection imaged 1.3 cm above cavity floor.
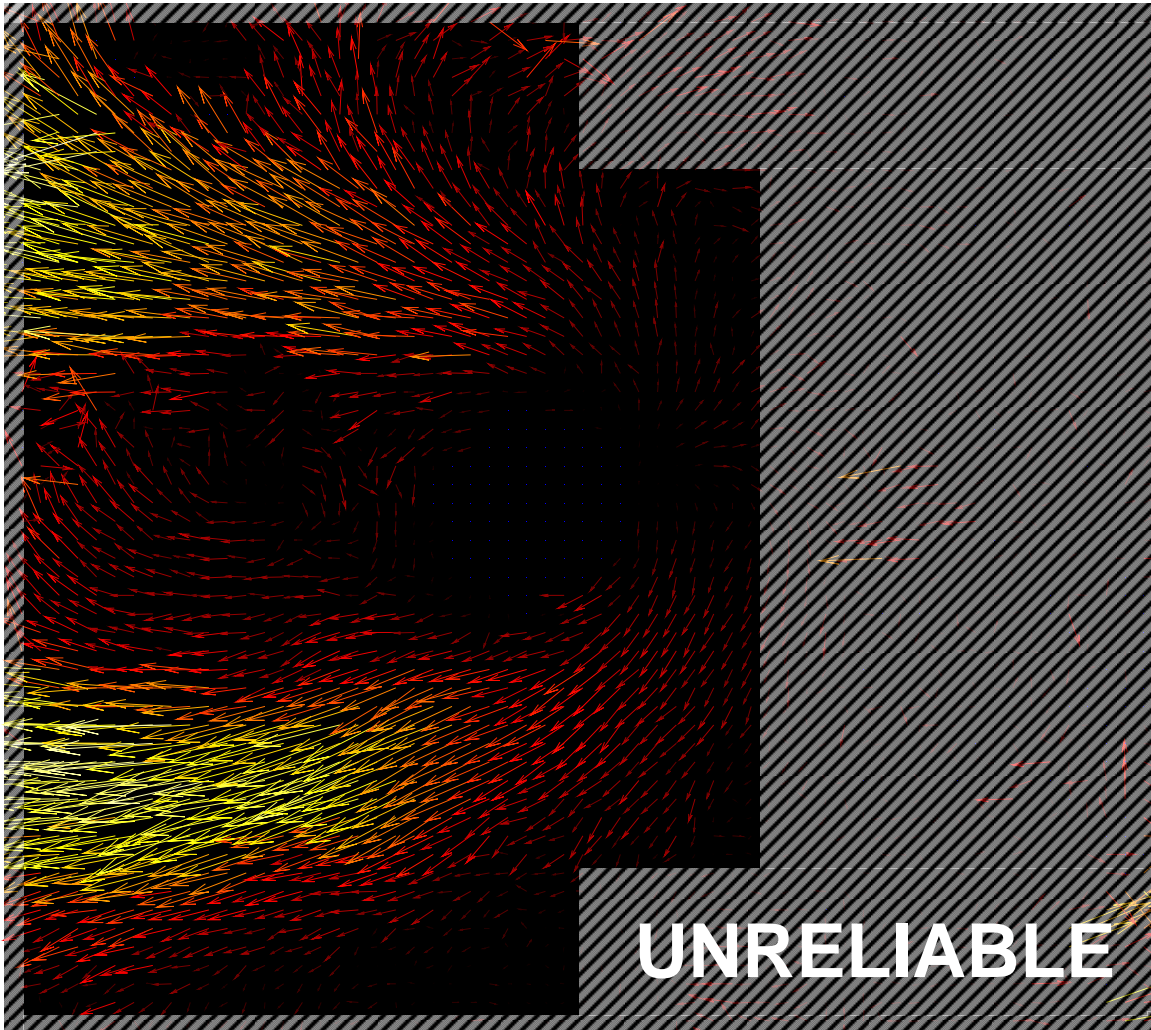
Figure 51: Vector map overlay for dual injection imaged in lower cavity.

The jet plume branches are seen accelerating up to 214 m/s. The downstream cavity wall was located left of the image border in Figure 51. Some streamline curvature due to the aft wall can be detected, but the stagnation region is apparently out of view. Additionally the complex flow pattern predicted in the aft portion of the cavity most likely contributed to the diverging and swirling motion seen throughout the figures above. Lastly, regarding the validity of certain vectors, the warning given in the preceding section also applies to results presented in this section.

4. 3. 3   Mid-Cone on Forward Swept Sting, Dual Injection.

The first cone test utilized dual nozzle/intra-cone injection and the flow was imaged directly aft of the cone base at mid-cone level, approximately 1.25 inches above the test section floor. Previous CO_2 PIV tests analyzing conical flow experienced no success introducing CO_2 particles into the recirculation region directly aft of the base surface. It was hypothesized that injecting through a hollow cone might provide the desired particles to the recirculation region with minimal intrusiveness. Unfortunately this did not work in a manner producing high quality PIV images due to excessively high intra-cone injection rates which created a fluctuating stream of highly concentrated CO_2 vapor exiting the cone as shown in Figure 52. The inner diameter of the intra-cone injection feed tube was reduced from 20/1000 inch to 10/1000 inch in an attempt to reduce the CO_2 mass flow rate. However, as previously stated, it was observed that no significant amounts of CO_2 could pass through such a small constriction.
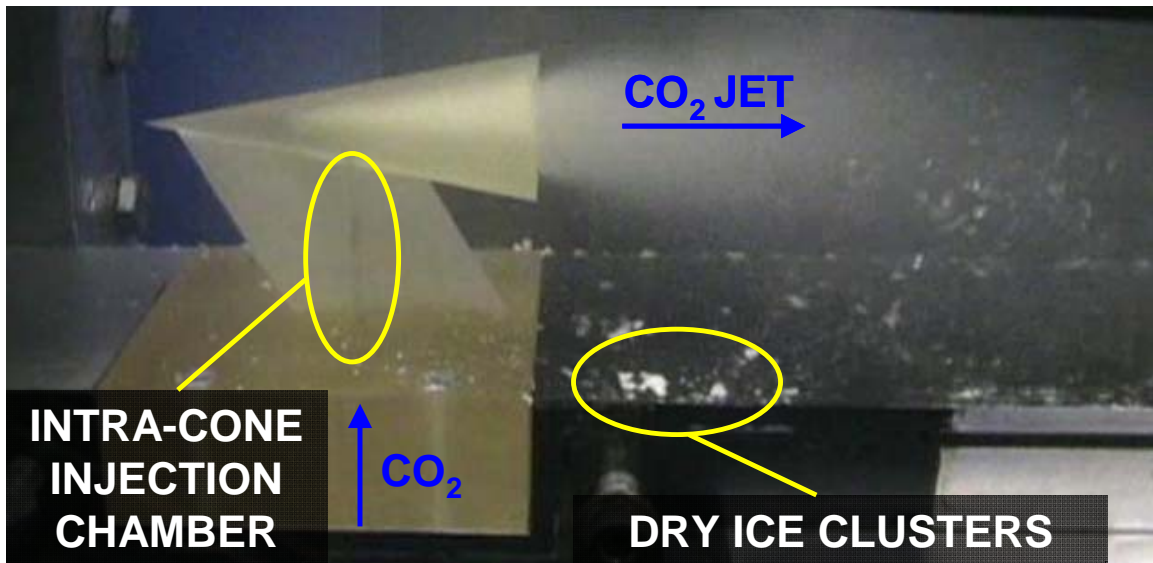
Figure 52: Intra-cone injection with no main air flowing.

Dry ice was visually observed building up on the inner cone cavity surface before breaking off in large chunks and shooting out the back of the cone. However, the particle distribution was decent both above and below the overexposed CO_2 jet plume, as shown in Figure 53. A laser blocker was used to try and alleviate some of the laser reflections off the cone surface. This is seen in Figure 53 as the shadow cast span wise across the right side of the images, covering up the aft end of the cone. The reflected light intensity from the intra-cone injection jet stream was so intense that it bled over into the shadow region, especially in the second frame.
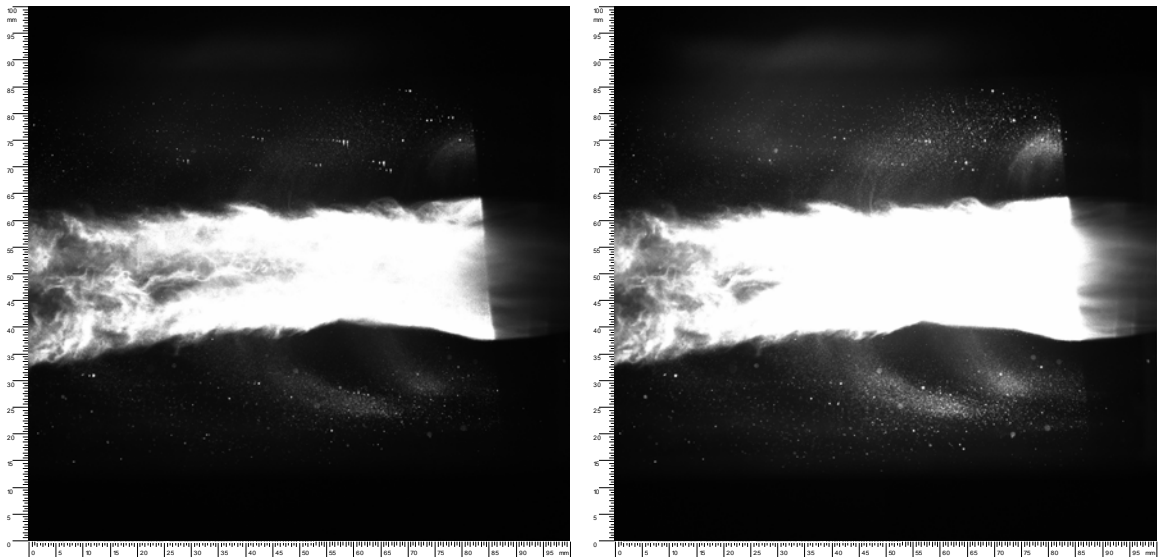
Figure 53: Dual injection imaged mid-cone (forward swept).

The vectored color map, Figure 54, shows slight curvature as the flow expanded around the corners of the cone. The flow was predominantly uniform at a measured velocity of 566 m/s throughout the upper and lower flow regions, within 9% of the predicted velocity of 625 m/s aft of the cone expansion.

126

Table 15: Values for dual injection imaged mid-cone (forward sting).

Test Date	4-Apr (tst1)	Rejected Vectors	152
Setup	forward mid cone	Substituted Vectors	1218
Injection	20/N + 20/T	Total Vectors	2288
IM Pairs Correlated	60	Average Velocity	467 m/s
Scale Factor	4.023	Standard Deviation	78 m/s
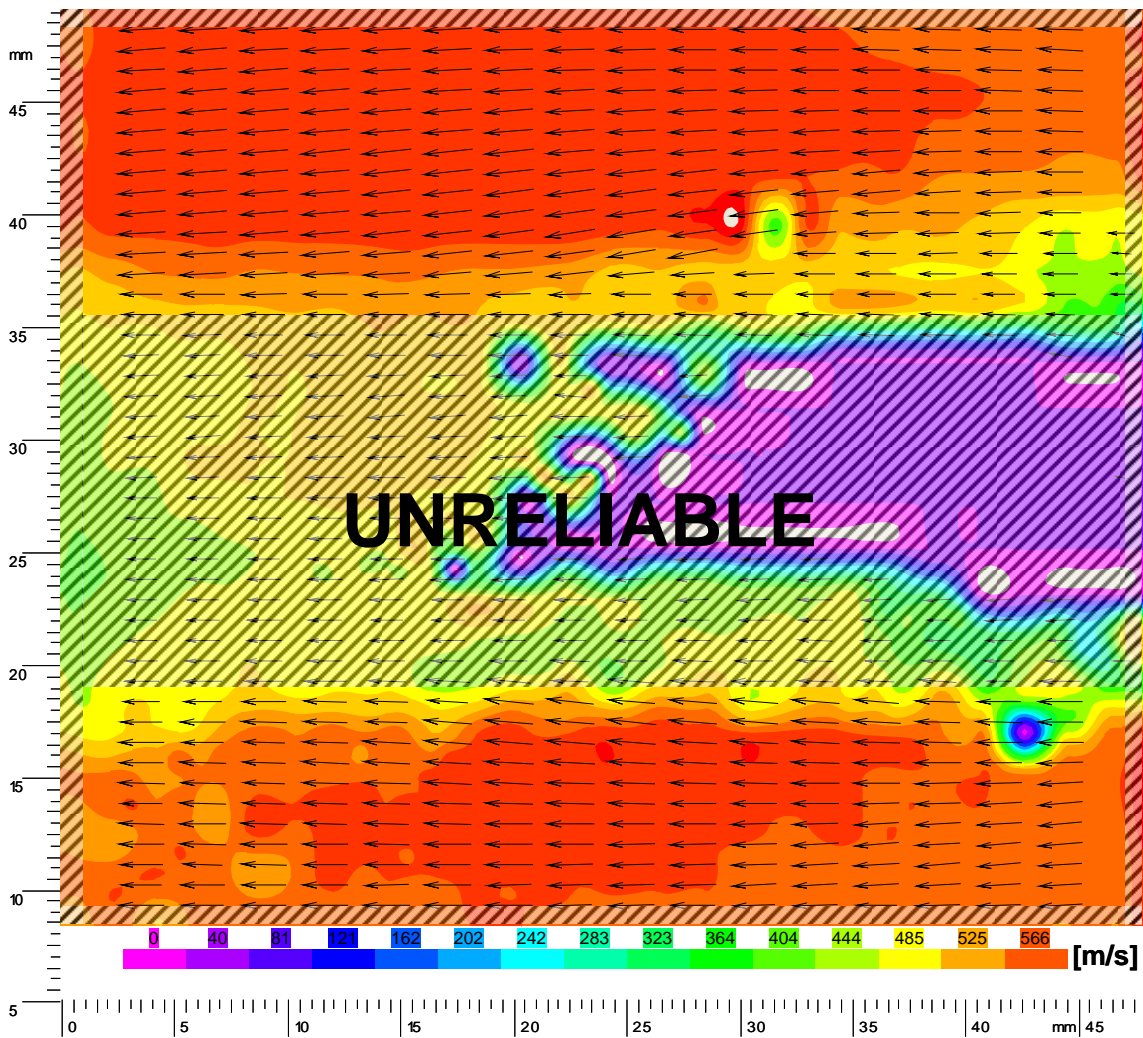
Figure 54: Vectored color map for dual injection imaged mid-cone (forward sting).

4. 3. 4   Mid-Cone on Forward Swept Sting, Single Injection.

The second test performed with the forward swept sting cone model imaged single nozzle injection at the mid-cone plane. The characteristic conical flow field was observed as shown in Figure 55. Distinct flow structures can be identified including the converging flow streams aft of the cone, the convergence point near the center of the frames and the flow straightening recompression region downstream of the convergence point. The particle distribution is reasonable across the entire flow field, apart from a few saturated particle groups and the dark base region within approximately one cone base diameter downstream of the cone, which promises high fidelity flow traces from this dataset. All of the raw image maps presented in this chapter are displayed at custom brightness levels that help the human eye to make out the particles; the actual images are much dimmer.
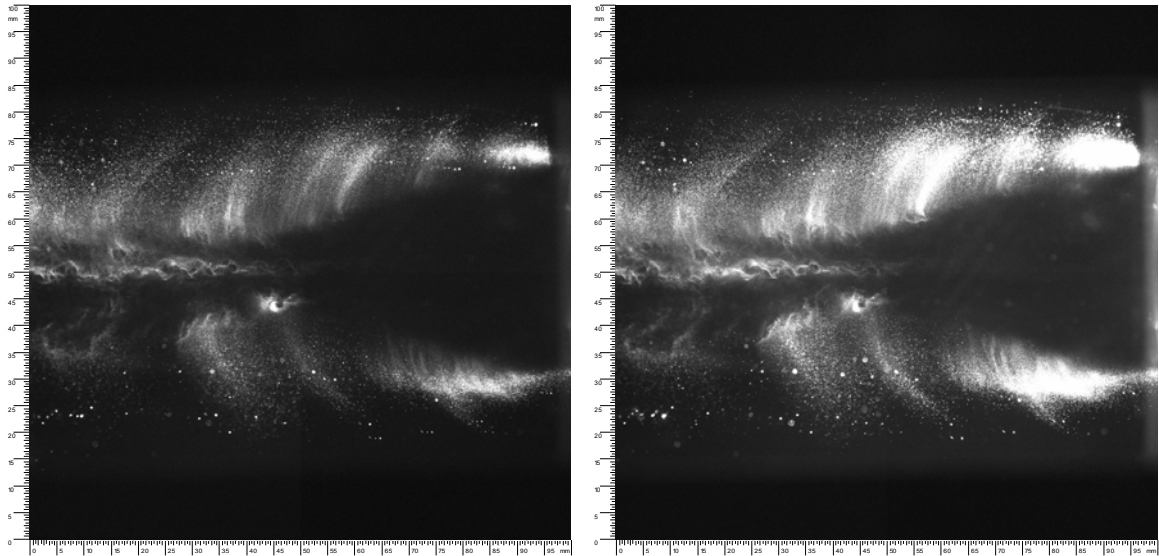
Figure 55: Nozzle injection imaged mid-cone (forward sting).

Table 16: Values for nozzle injection imaged mid-cone (forward sting).

Test Date	4-Apr (tst4)	Rejected Vectors	194
Setup	forward mid cone	Substituted Vectors	1471
Injection	20/N	Total Vectors	2835
IM Pairs Correlated	60	Average Velocity	529 m/s
Scale Factor	4.023	Standard Deviation	68 m/s
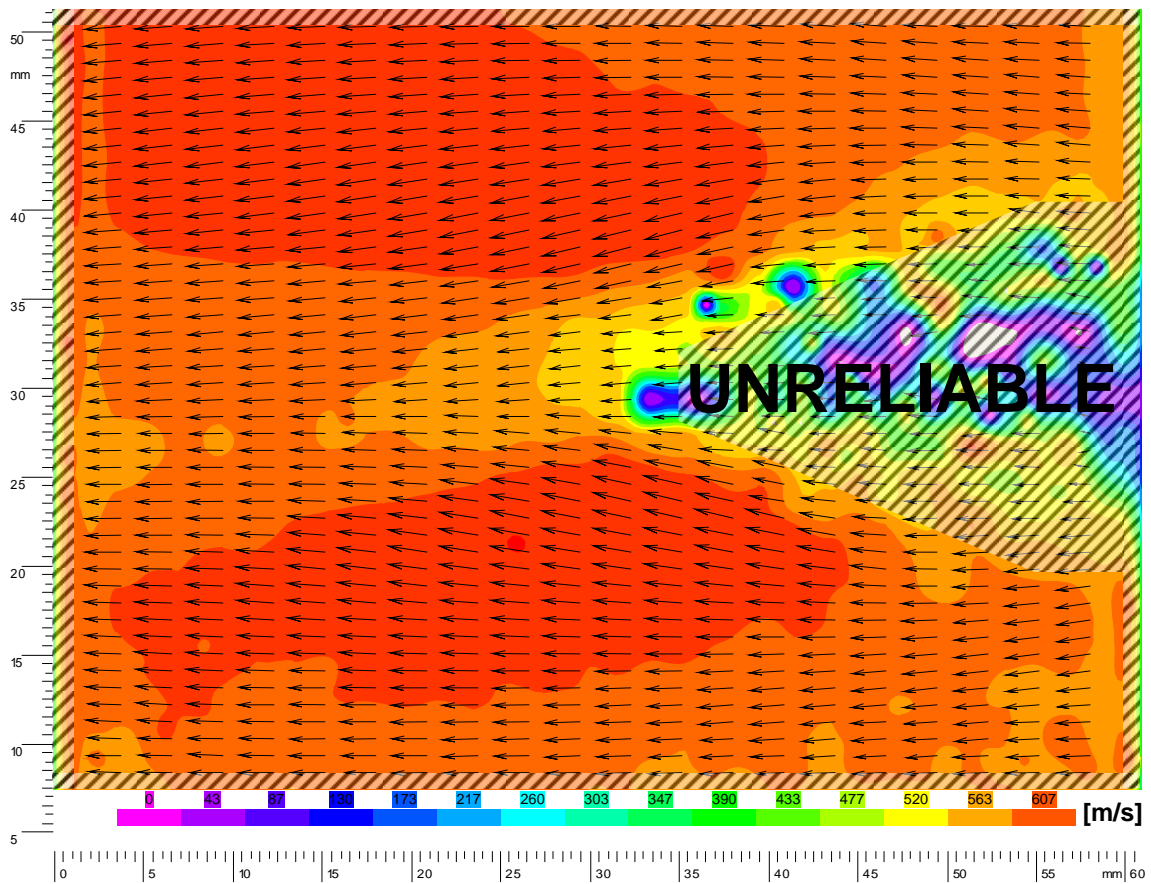
Figure 56: Vectored color map for nozzle injection imaged mid-cone (forward).
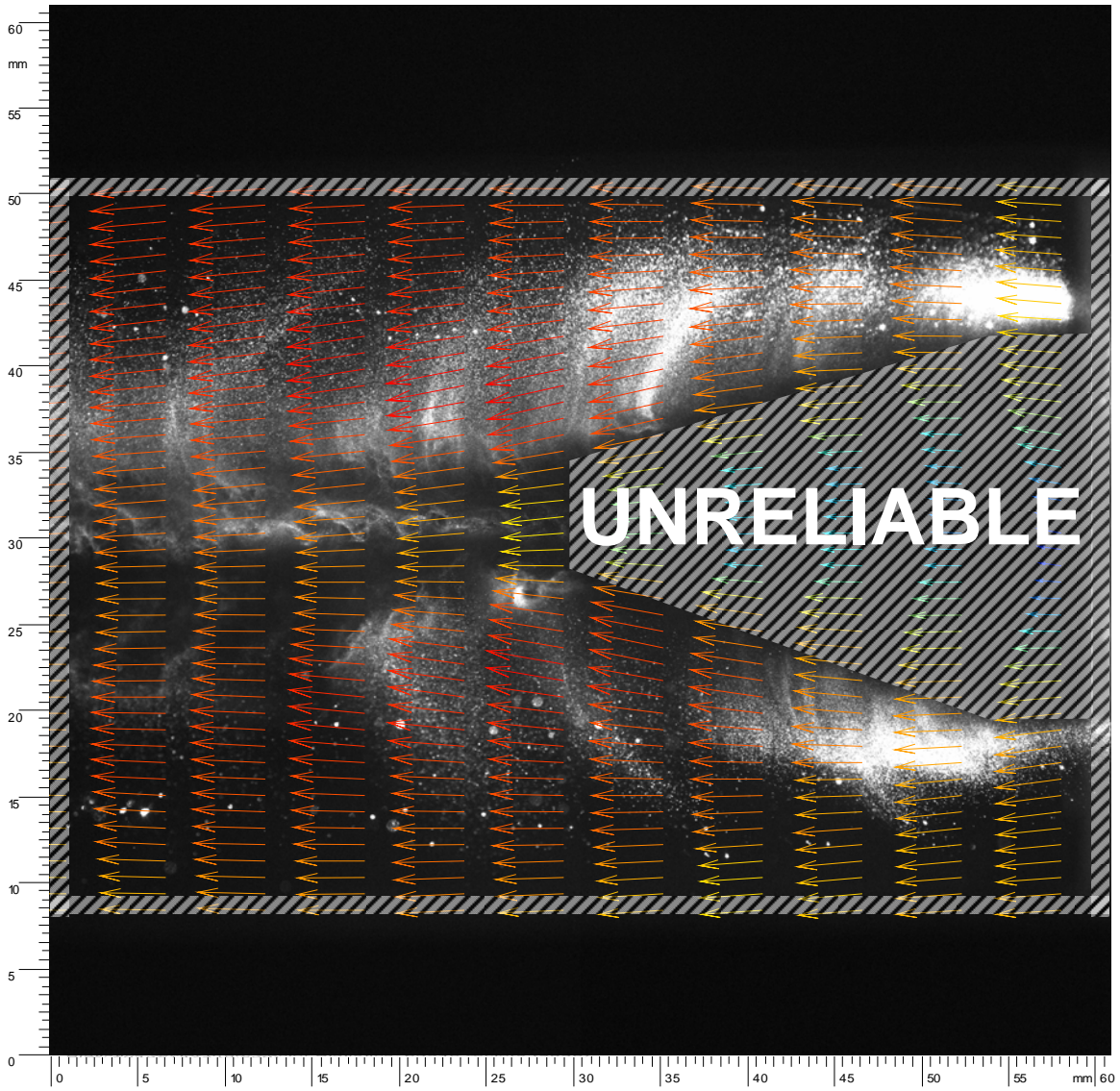
Figure 57: Vector map overlay for nozzle injection imaged mid-cone (forward).

The flow is observed turning around the trailing edge of the cone and converging while accelerating from 560 m/s up to 607 m/s, within 3% of the predicted flow velocity downstream of the cone expansion. As expected, almost no particles are seen in the separated flow region immediately aft of the cone base, which creates unreliable noise. However, the flow is observed decelerating from the converging separated shear layers to the cone centerline located at 30 mm along the span wise (vertical) axis. Although the vectors shown in the near wake region (within approximately one cone base diameter) are merely interpolations based on actual vectors flowing around the cone, the fact that they are symmetric about the cone centerline and decelerating towards the recirculation region holds promise. Counter-rotating vortex flow is expected in the recirculation region behind a cone (Scarano and van Oudheusden, 2003). The subsonic vortices should be enveloped by a symmetrically converging high-speed flow which slightly decelerates towards the separated mixing layers.

The separated shear layers merge at the reattachment point readily identified in the center of Figure 56 at the 30 mm point along the stream wise (horizontal) axis. Both the expansion region about the cone base and the symmetric recompression shock are easily identified in the velocity maps. The velocity vectors are seen deflecting along this interfacing compression line, especially in the lower half of the picture, to redirect the wake flow in the downstream direction with the 1-D uniform freestream at a velocity of approximately 590 m/s.

Lastly, an interesting flow structure is seen translating downstream from the wake reattachment point. A turbulent stream tube of CO_2 condensate containing small eddies is shown clearly in both frames of Figure 55 dividing the upper and lower image regions.

131

Thus, it is likely groups of particles, rather than individual particles, dominate the PIV signal in the central wake region.

To get a feel for the changing flow conditions in the far wake region, stream wise velocity profiles (x-velocity) and span wise velocity profiles (y-component) were plotted versus the span wise direction (y-direction) at different stations downstream of the separated flow region. The velocity profiles shown in Figure 58 follow the expected pattern.
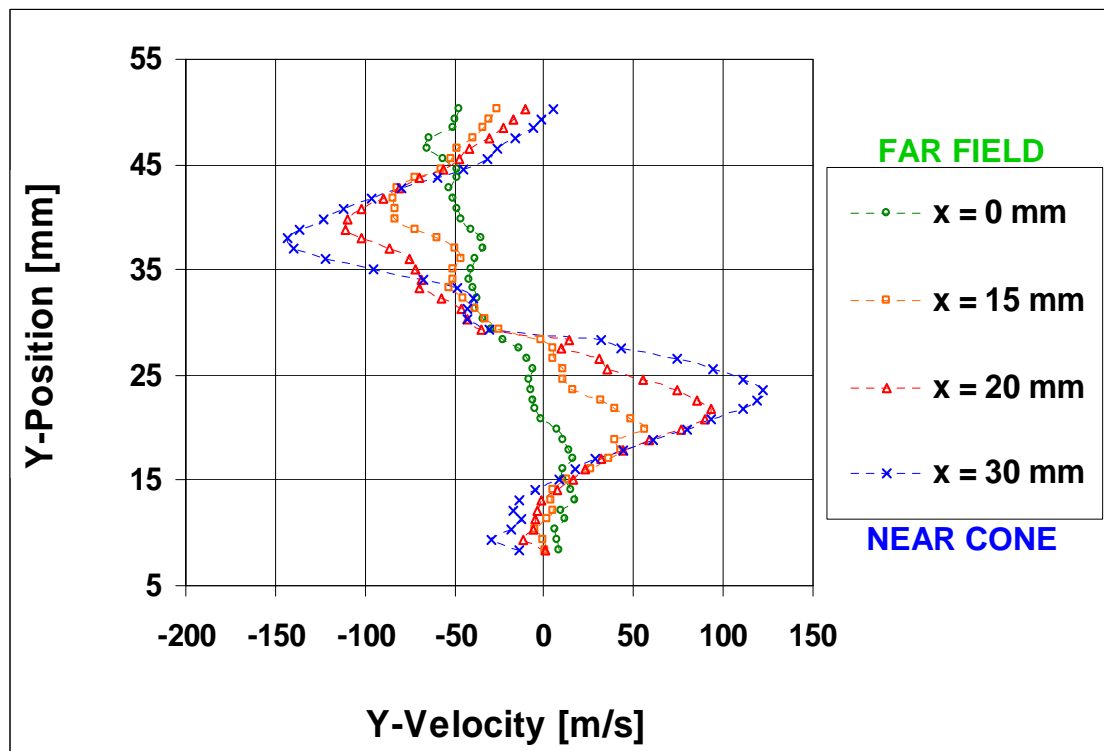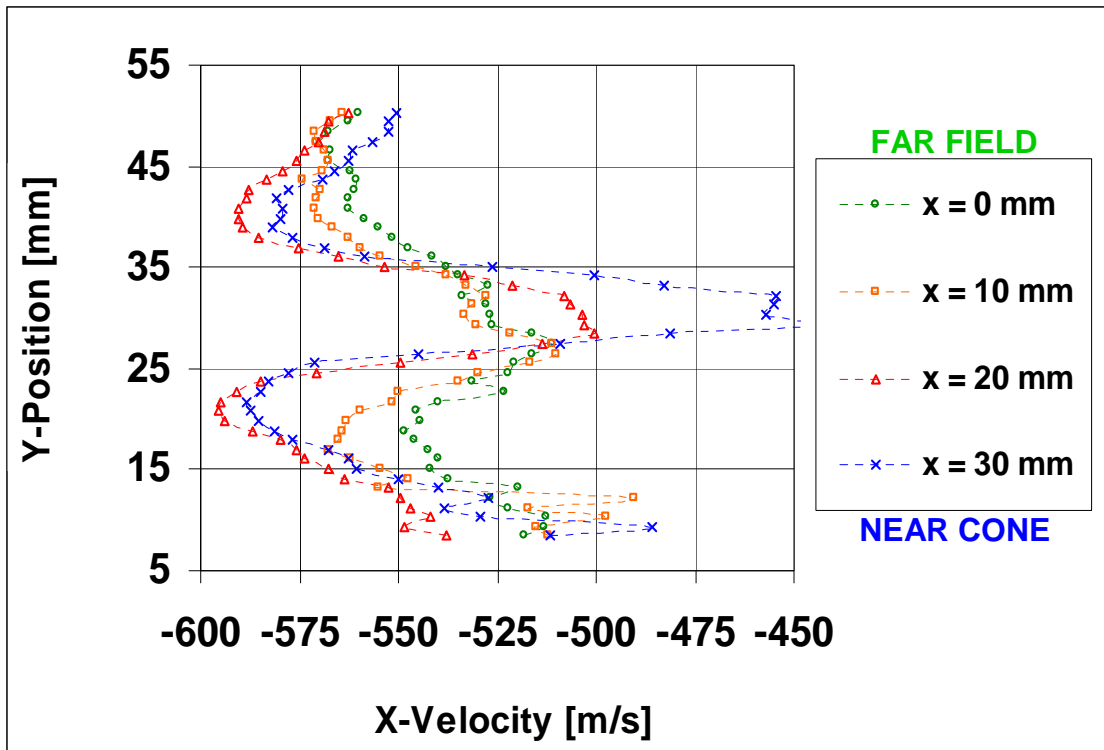
Figure 58: Velocity profiles in the far wake region of a circular cone.

133

4. 3. 5   Below Cone on Combination Sting, Single Injection.

The next series of cone tests employed the combination sting model. The first run imaged independent nozzle injection approximately 1.0 cm above the test section floor. The thought behind the combination sting design is the lower portion of the sting, perpendicular to the flow, offers a slender diamond cross section designed to minimally perturb the fluid flowing underneath the cone in order to minimize interference to the conical flow pattern. The upper portion of the sting is shaped to follow the conical shock wave angle predicted by Taylor-Maccoll theory in an attempt to further minimize interference to the conical flow pattern.
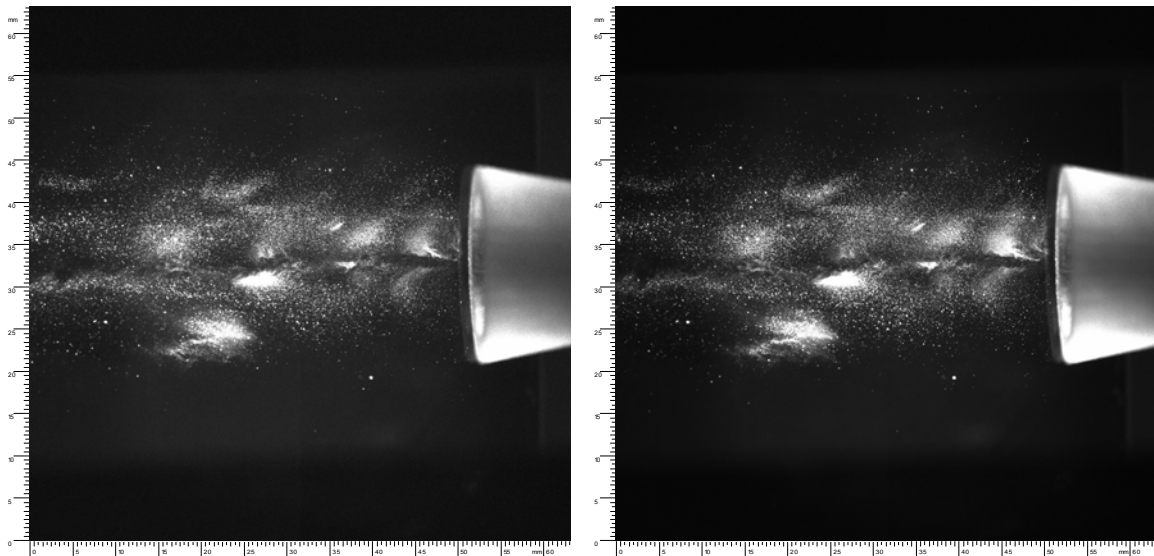
Figure 59: Nozzle injection imaged below cone (combination sting).

A distinct dark region line is seen running down the center of both IM frames in Figure 59. Even though the plane of illumination is close to the test section floor, the particle dispersion density is good; this reflects positively upon the current injection

134

system's ability to seed the entire flow field in the transverse direction. Unfortunately, low particle distribution densities in the upper and lower image regions prevented accurate PIV correlation in these outer regions. Figure 60 shows fairly uniform 1-D flow slightly slowed after the sting but accelerating to 594 m/s, within 3% of the predicted freestream velocity of 610 m/s. The centerline flow slightly perturbed around the sting is seen converging downstream.

Table 17: Values for nozzle injection imaged below cone (combination sting).

Test Date	10-Apr (tst2)	Rejected Vectors	814
Setup	combination below cone	Substituted Vectors	1562
Injection	20/N	Total Vectors	2772
IM Pairs Correlated	75	Average Velocity	445 m/s
Scale Factor	4.17	Standard Deviation	131 m/s
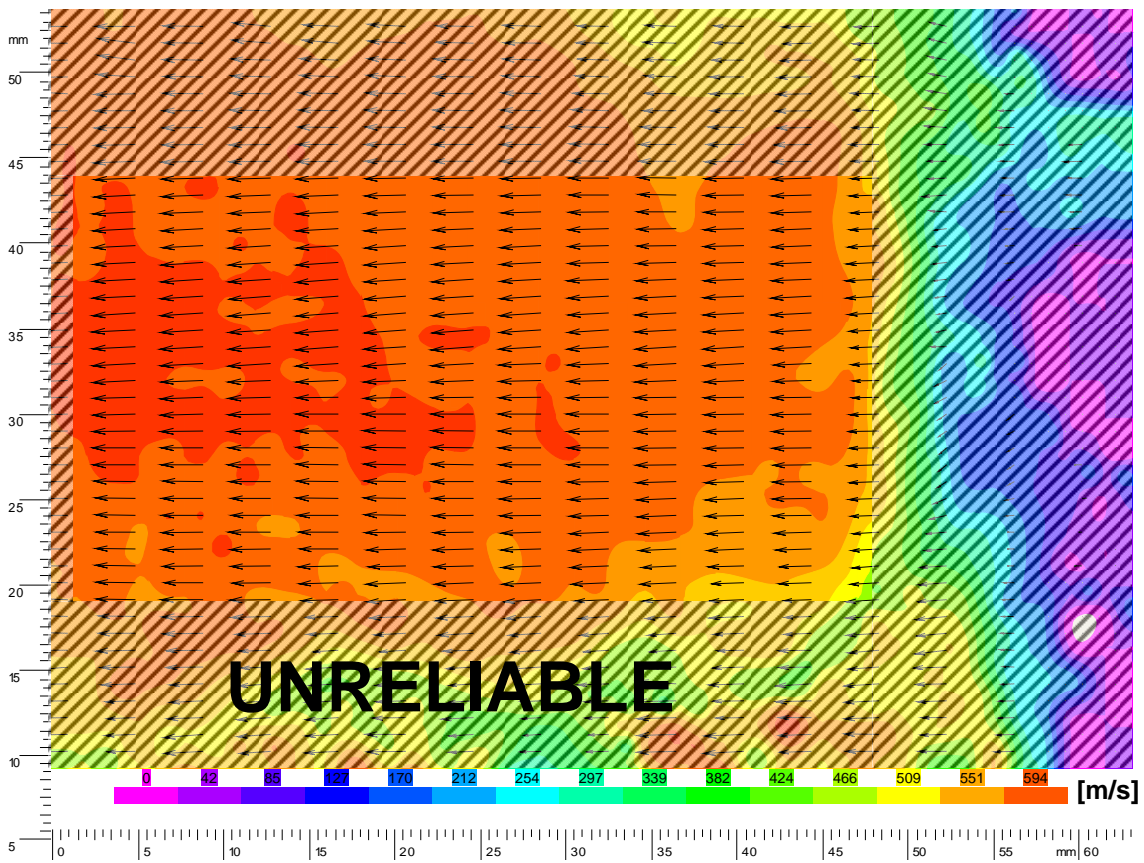
Figure 60: Vectored color map for nozzle injection imaged below cone (comb.).

4. 3. 6   Mid-Cone on Combination Sting, Single Injection.

The final run to be presented imaged independent nozzle injection at the mid-cone plane 1.25 inches from the test section floor. Once again, a laser blocker was employed to prevent reflections off of the cone surface. Judging from the images collected the laser plane may have been slightly below mid-plane.   This is suggested because no recompression region is seen, which may indicate the laser plane is slightly below the recompression shock. Granted, the images do include more cone area and therefore less down stream flow, which may prevent one from seeing the recompression region. Nonetheless a distinct convergent region is observed, most of which is shadowed by the laser blocker.   Additionally, the particle distribution density is magnificent, showing slight particle duplication of larger particles.
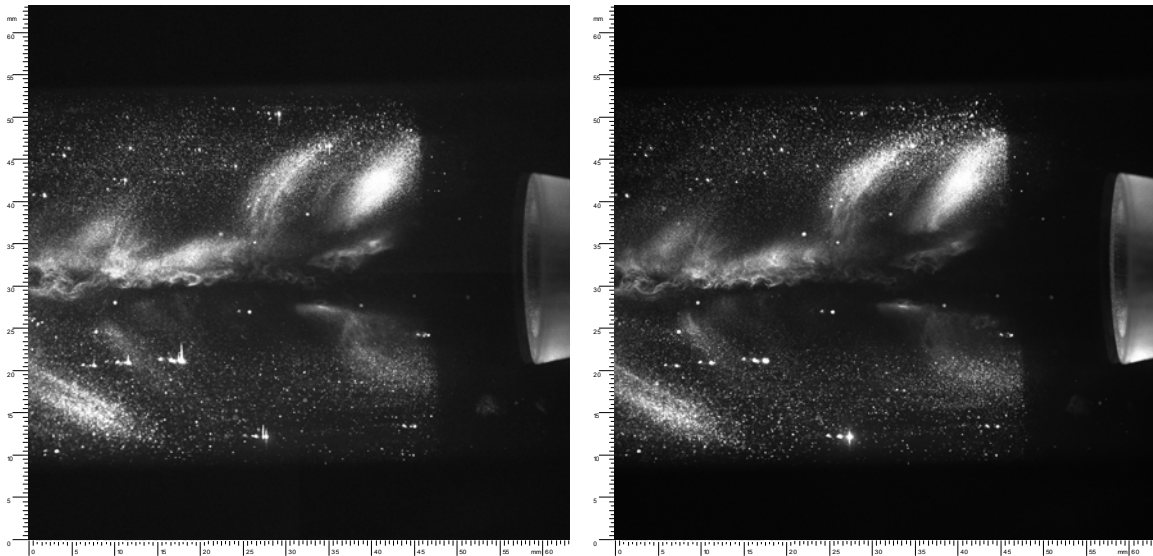
Figure 61: Nozzle injection imaged mid-cone (combination sting).

Table 18: Values for nozzle injection imaged mid-cone (combination sting).

Test Date	10-Apr (tst4)	Rejected Vectors	272
Setup	combination mid-cone	Substituted Vectors	1392
Injection	20/N	Total Vectors	2772
IM Pairs Correlated	75	Average Velocity	169 m/s
Scale Factor	4.17	Standard Deviation	139 m/s
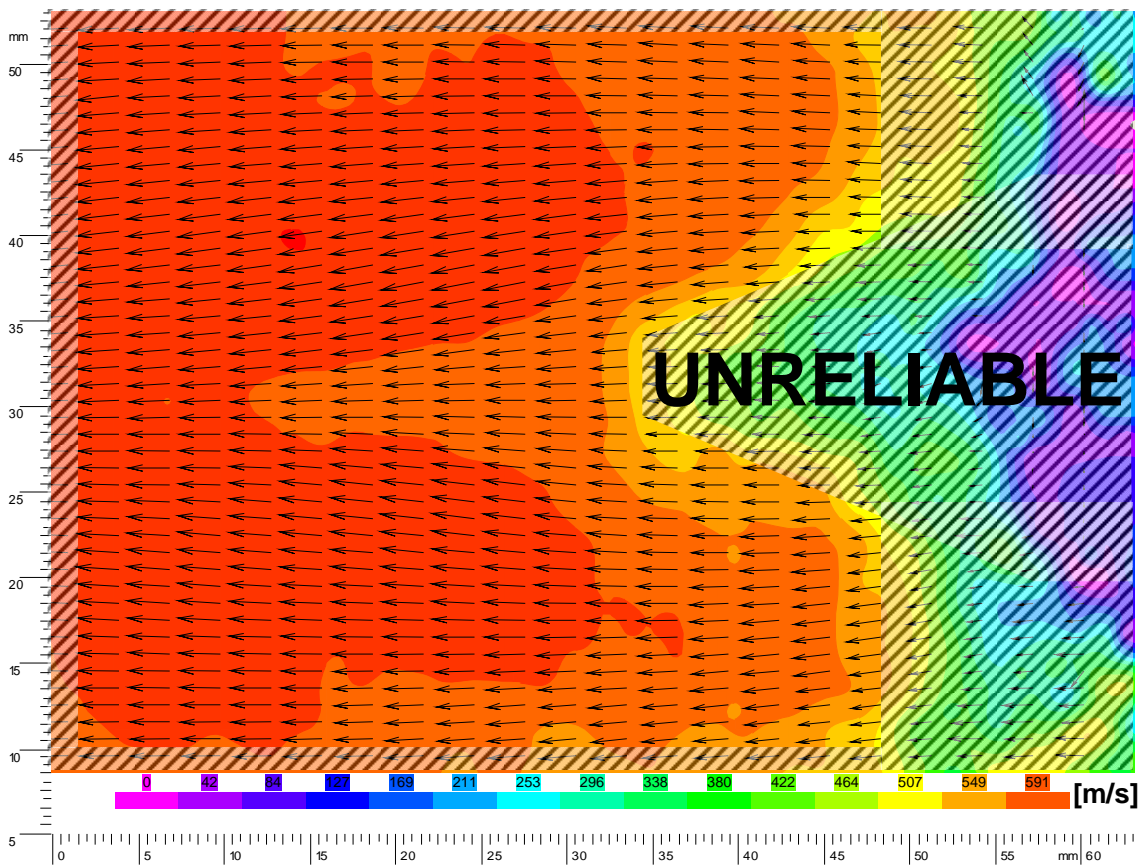
Figure 62: Vectored color map for nozzle injection imaged mid-cone (combination).

Even though Figure 62 utilized a larger scale factor than Figure 56, the velocities computed are smaller, which is contradictory. Additionally, the perceived recirculation region is smaller than seen in Figure 56. The flow is still seen converging towards the center of the image but less dramatically, accelerating to 591 m/s. Overall, the velocities are smaller indicating a weaker expansion, as would be experience by a streamline further away from the cone surface. These points reinforce the idea the images may have been taken below the mid-cone plane.

Lastly, velocity profiles for the two cone/sting combinations are compared at a downstream station in the far wake region greater than one cone base diameter downstream of cone. Since the two tests being compared were analyzed with different fields of view, it is hard to say the same position in the two vector maps (x = 20 mm) corresponds to the same station in the physical object plane of the two tests. Additionally there is a much larger x-velocity deficit for the forward swept case, indicating closer to the recirculation region. However, by visual inspection of the two raw image sets, the two stations appear to be within one millimeter of each other making the comparison reasonable. Based on Figure 63 the maximum x-velocity downstream of the cone supported by the forward swept sting is 2% greater than aft of the cone supported by the combination sting.
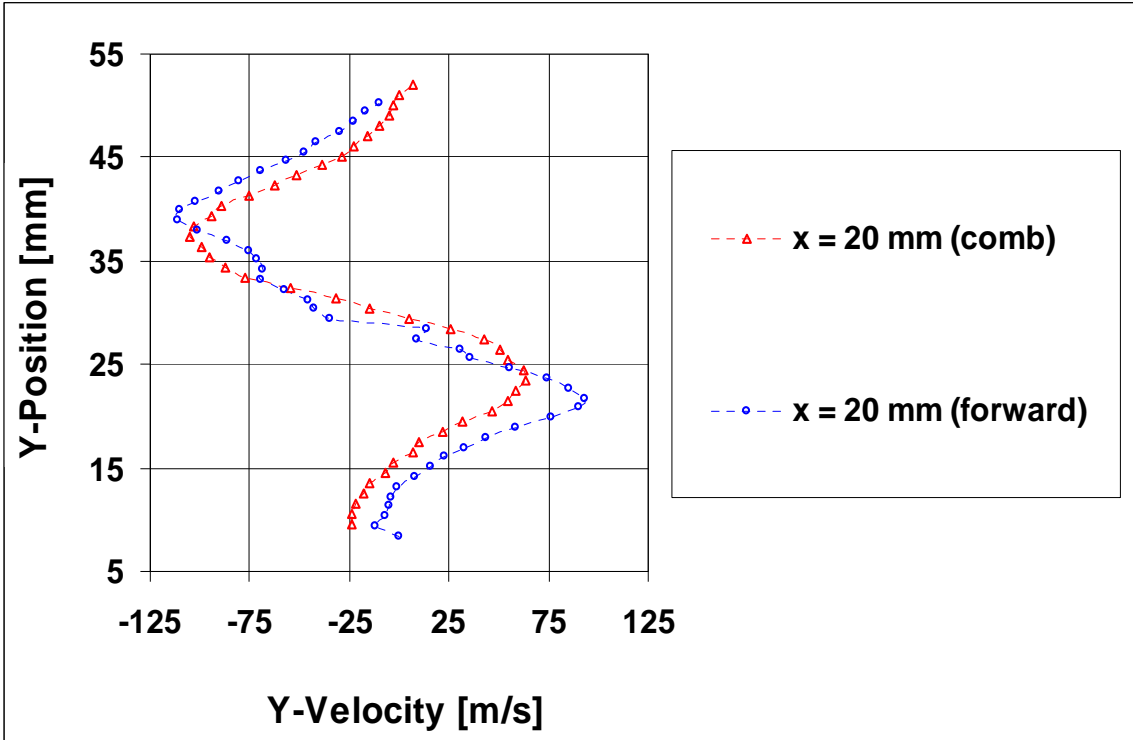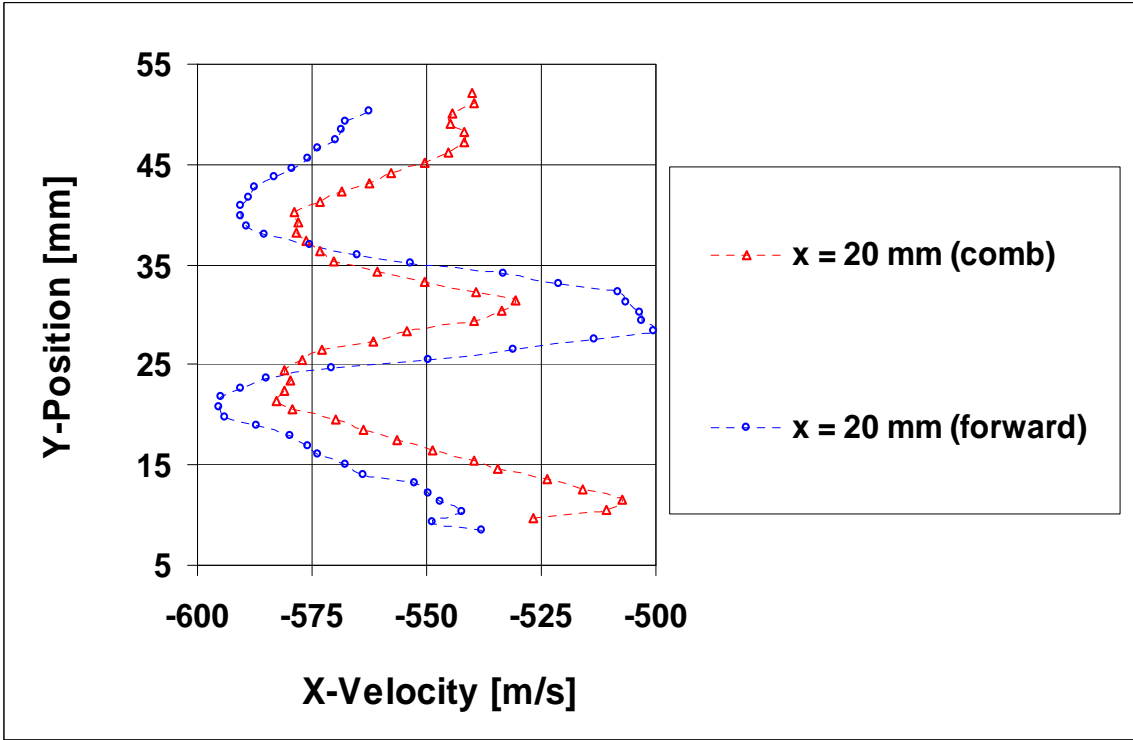
Figure 63: Cone and sting velocity profile comparison in far wake region.

5. Conclusions and Recommendations

5. 1   Results Summary and Conclusion

(1) The adaptive correlation recipe produced the best vector maps, which matched theoretical flow structure. The CO_2 particles had no trouble scattering sufficient light for a strong signal to noise ratio; in fact the signal was sometimes too strong, overexposing pixels. The seed particles showed slight ability to track recirculating flow. Carbon dioxide was found to be non-intrusive with regards to cooling effects and gas mixture molecular weight effects.

(2) All of the velocities measured using the PIV technique were approximately 3% to 9% below those predicted by compressible gas flow theory.

(3) Independent nozzle injection using a 3/16 inch shroud injector connected to a 20/1000 inch feed tube produced good PIV images of the empty test section and flow aft of a cone. Nozzle injection produced better vector maps than did stagnation chamber injection. The maximum velocities measured in the empty test section were 583 m/s, which is 5% below the 610 m/s predicted by compressible gas flow theory.

(4) Simultaneous nozzle injection and transverse cavity injection, using a 1/16 inch shroud injector connected to a 20/1000 inch feed tube at the test section injection point, produced good images of the transverse cavity jet. The jet plume cross section expansion

and the flow acceleration are easily identifiable. The flow is seen accelerating in the stream wise direction from 0 m/s at the injection point to 533 m/s at a point 32 mm downstream.

(5) Lower in the cavity complex flow patterns are predicted which affect the jet stream causing plume bifurcation and dispersion. The two plume branch cores are seen accelerating downstream from 0 m/s to 214 m/s while the particles along the branch periphery are observed curving around and redirecting upstream.

(6) Intra-cone injection mass flow rates were too high to supply supplementary particles to the recirculation region. Far field velocities above and below the intra-cone CO_2 jet were 566 m/s, 9% below the 625 m/s predicted. This test produced the largest velocity comparison disagreement.

(7) The cone supported by the forward swept sting provided the best data set. Flow regions and structures were clearly visible including flow expansion around the cone base, separated shear layer convergence, an empty recirculation region, the flow reattachment point and a symmetrical recompression shock. The flow velocity was measured accelerating from 560 m/s to 607 m/s around the cone base which is within 3% of the 625 m/s predicted.

(8) The freestream flow below the cone utilizing the combination sting was barely affected by the slender diamond cross section of the sting. The flow diverged and slowed slightly while passing around the sting but it converged and redirected downstream accelerating to a freestream value of 594 m/s, 3% below the 610 m/s predicted.

(9) The velocity measurements made aft of the cone supported by the combination sting were slightly below those measured downstream of the cone supported by the forward swept sting. Based on reduced flow velocities and a smaller recirculation region the measurement plane appears to be slightly below mid-cone plane. The flow accelerates around the cone up to 591 m/s, 5% below the 625 m/s predicted. This should be noted as 2% higher than the cone supported by the forward swept sting.

5. 2   Desired Impact of this Research

The information presented in this paper should enable fellow researchers to start employing this clean seeding process in similarly scaled wind tunnels. With more development, this PIV seeding technique could become better understood and more controllable allowing fine tuning of the process for more accurate results or even different applications. The enabling technology this approach to PIV seeding promises is exciting. Employing carbon dioxide as the seed material could lower facility cleaning cost and ultimately research and development cost, while still enabling researchers to obtain quality results.

5. 3   Recommendations for Future Experimentation

First and foremost the laser system needs to be calibrated and aligned; two identical laser sheet pulses with rectangular slot profiles are essential.

In regards to the dropping control pressure phenomena, I believe moving the control pressure to its own separate air supply, effectively removing its connection to the solenoid valves and any other component of the wind tunnel may be the solution to this problem. Additionally, a control pressure valve with feedback may be required; the simple fixed opening valve currently employed may not be appropriate. As the back pressure (vacuum pressure) increases additional stagnation pressure may be required to

144

maintain a run. However, this may have the adverse effect of increasing the air mass flow rate during a run.

The relaxation technique across a shock wave should be used to quantify the responsiveness of CO_2 particles and to estimate particle sizes. Along with this a detailed investigation of shock wave effects on CO_2 particles would be interesting.

Carbon dioxide mass flow regulators should be used to precisely control the amount of liquid CO_2 delivered to each injection location. If regulators had been used with the intra-cone injection the technique may have worked.

Different injectors based off the shroud injector should be tested. More control over particle size and dispersion can be obtained if the injector variables can be connected with associated parameters affected by each variable.

Lastly, if the nozzle injection location is going to be used then an assessment of its impact on the main flow should be completed. Comparing Schlieren images taken of the test section both with and without and injector present in the nozzle would at least qualify any major flow disturbances propagating downstream into the test section.

Appendix A :   Properties of Carbon Dioxide

(Wittemann)

Property	US Units	SI Units
Molecular Weight	44.01	44.01
Vapor Pressure of Saturated Liquid	853 psia	5,875 kPa abs
@ 70°F (21°C) [Cylinder]	505 psia	3,485 kPa abs
@ 32°F (0°C)	316 psia	2,180 kPa abs
@ 2°F (-17°C) [refrigerated liquid]	215 psia	1,482 kPa abs
@ -20°F (-29°C)	75 psia	518 kPa abs
@ -69.9°F(-56.6°C) [triple point]	14.7 psia	101 kPa abs
@ -109.3°F (-78.5°C) [dry ice]		
Density (Gas)	0.114 lb/ft3	1.833 kg/m3
@ 70°F (21°C) and 14.7 psia	0.123 lb/ft3	1.977 kg/m3
@ 0°C (32°F) and 1 atm (101 kPa abs)		
Density (Saturated Liquid)	47.6 lb/ft3	762 kg/m3
@ 70°F (21°C) [Cylinder]	58.0 lb/ft3	929 kg/m3
@ 32°F (0°C)	63.3 lb/ft3	1,014 kg/m3
@ 2°F (-17°C) [refrigerated liquid]	66.8 lb/ft3	1,070 kg/m3
@ -20°F (-29°C)	73.5 lb/ft3	1,177 kg/m3
@ -69.9°F(-56.6°C) [triple point]		
Density (Solid Dry Ice)	97.5 lb/ft3	1,562 kg/m3
@ 14.7 psia and -109.3°F (101 kPa abs and -78.5°C)		
Sublimation Temperature (at 1 atm)	-109.3°F	-78.5°C
Critical Temperature	87.9°F	31.1°C
Critical Pressure	1,071 psia	7,382 kPa abs
Critical Density	29.2 lb/ft3	468 kg/m3
Triple Point	-69.9°F / 75.1 psia	-56.6°C / 518 kPa abs
Latent Heat of Vaporization	100.6 BTU/lb	234.5 kJ/kg
@ 32°F (0°C)	119.0 BTU/lb	276.8 kJ/kg
@ 2°F (-17°C) [refrigerated liquid]	129.7 BTU/lb	301.7 kJ/kg
@ -20°F (-29°C)		
Latent Heat of Fusion	85.6 BTU/lb	571.3.0 kJ/kg
@ -69.9°F (-56.6°C) [Triple Point]		
Latent Heat of Sublimation	245.5 BTU/lb	199.0 kJ/kg
@ 109.3°F (-78.5°C) [Dry Ice]		
Specific Heat of Gas	0.203 BTU/lb°F	0.850 kJ/kg°C
Cp at 77°F (25°C) and 1 atm	0.157 BTU/lb°F	0.657 kJ/kg°C
Cv at 77°F (25°C) ant 1 atm		
Ratio of Specific Heats of Gas	1.304	1.304
@ 59°F (15°C)		
Specific Heat of Liquid	0.489 BTU/lb°F	2.048 kJ/kg°C
@ 2°F (-17°C) [refrigerated liquid)		
Solubility of gas in water, vol/vol	1.7	1.7
@ 32°F (0°C) and 1 atm	1.0	1.0
@ 60°F (16°C) and 1 atm	8.6	8.6
@ 32°F (0°C) and 60 psig (414 kPa g)		
Viscosity (Saturated Liquid)	0.287 lb/ft h	0.119 x 10-3 Pa s
@ 2F (-17C) [refrigerated liquid]		

Appendix B :   90° Pipe Bends

(Crane, 1988:A-29)

"K" FACTOR TABLE— SHEET 4 of 4
Representative Resistance Coefficients (K) for Valves and Fittings
(for formulas and friction data, see page A-26)

("K" is based on use of schedule pipe as listed on page 2-10)

PLUG VALVES AND COCKS

Straight-Way

3-Way

View X—X

If: $\beta = 1$,
$K_1 = 18 f_T$
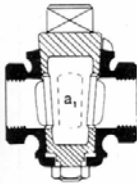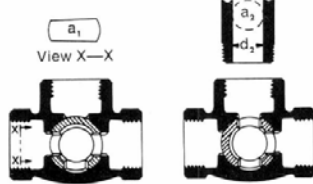
If: $\beta = 1$,
$K_1 = 30 f_T$

If: $\beta = 1$,
$K_1 = 90 f_T$

If: $\beta < 1 \ldots K_2 =$ Formula 6

MITRE BENDS

∝	K
0°	$2 f_T$
15°	$4 f_T$
30°	$8 f_T$
45°	$15 f_T$
60°	$25 f_T$
75°	$40 f_T$
90°	$60 f_T$

90° PIPE BENDS AND
FLANGED OR BUTT-WELDING 90° ELBOWS

r/d	K	r/d	K
1	$20 f_T$	8	$24 f_T$
1.5	$14 f_T$	10	$30 f_T$
2	$12 f_T$	12	$34 f_T$
3	$12 f_T$	14	$38 f_T$
4	$14 f_T$	16	$42 f_T$
6	$17 f_T$	20	$50 f_T$

The resistance coefficient, K_B, for pipe bends other than 90° may be determined as follows:

$$K_B = (n-1)\left(0.25\ \pi\ f_T \frac{r}{d} + 0.5\ K\right) + K$$

n = number of 90° bends
K = resistance coefficient for one 90° bend (per table)

CLOSE PATTERN RETURN BENDS

$K = 50 f_T$

STANDARD ELBOWS

90°

45°

$K = 30 f_T$

$K = 16 f_T$

STANDARD TEES

Flow thru run. . . . . . . $K = 20 f_T$
Flow thru branch. . . . $K = 60 f_T$

PIPE ENTRANCE

Inward Projecting
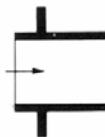
Flush

r/d	K
0.00*	0.5
0.02	0.28
0.04	0.24
0.06	0.15
0.10	0.09
0.15 & up	0.04

*Sharp-edged

$K = 0.78$

For K, see table

PIPE EXIT

Projecting

Sharp-Edged

Rounded

$K = 1.0$

$K = 1.0$

$K = 1.0$

Appendix C :   Moody Plots

(Crane, 1988:A-23 to A-25)

Relative Roughness of Pipe Materials and Friction Factors
For Complete Turbulence[18]
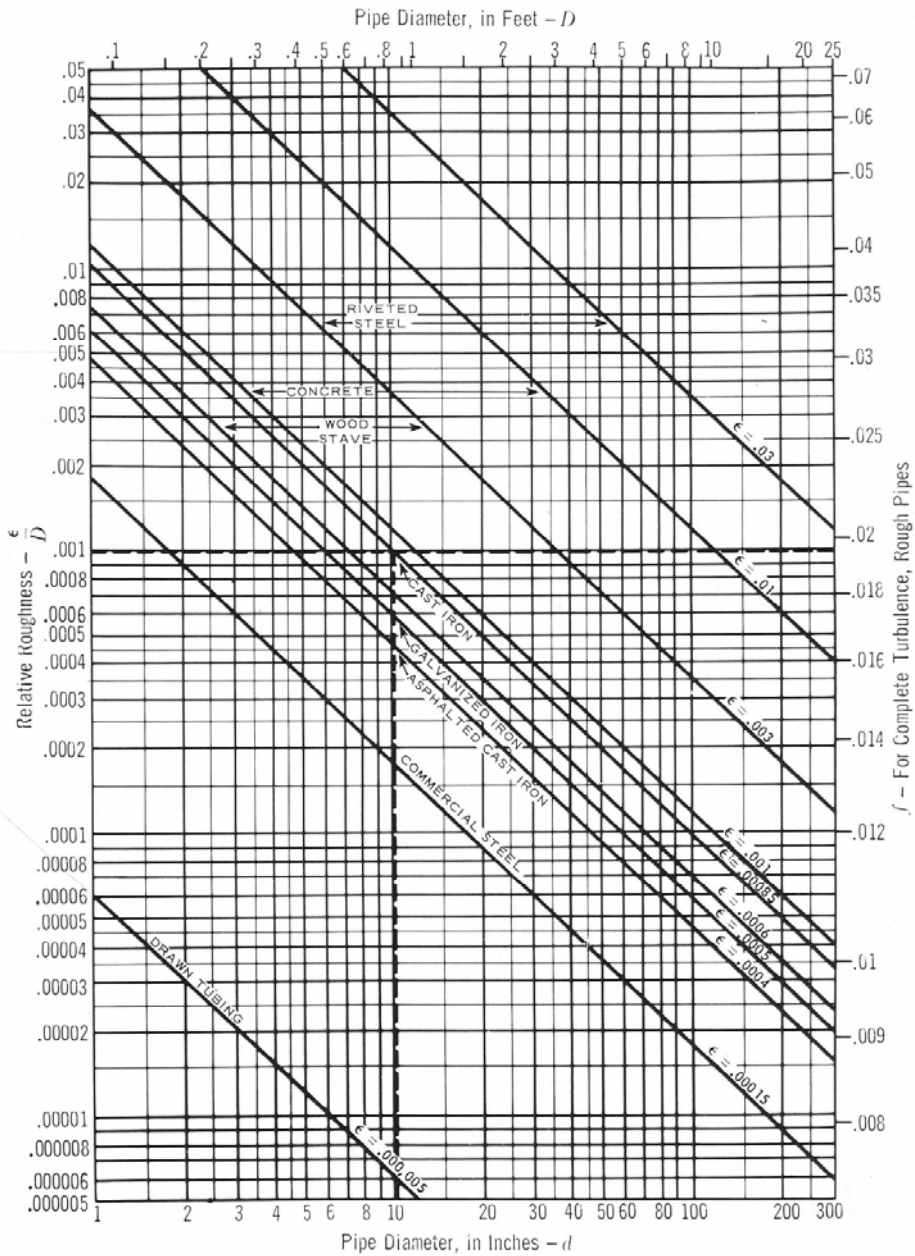
Problem: Determine absolute and relative roughness, and friction factor, for fully turbulent flow in 10-inch cast iron pipe (I.D. = 10.16″).

Solution: Absolute roughness (ϵ) = 0.00085 . . . . . Relative roughness (ϵ/D) = 0.001 . . . . . Friction factor at fully turbulent flow (f) = 0.0196.

151

VALUES OF (vd) FOR WATER AT 60° F (VELOCITY IN FT./SEC. X DIAMETER IN INCHES)

f

Friction
Factor =

$$\dfrac{h_L}{\left(\dfrac{L}{D}\right)\dfrac{v^2}{2g}}$$

Relative
Roughness

$$= \dfrac{\epsilon}{D}$$

$$f = 64\,/\,Re$$

LAMINAR ZONE
CRITICAL ZONE
TRANSITION ZONE
TURBULENT ZONE
COMPLETE TURBULENCE, ROUGH PIPES

SMOOTH PIPES

$$\dfrac{\epsilon}{D} = .000,001 \qquad \dfrac{\epsilon}{D} = .000,005$$

Re - Reynolds Number $= \dfrac{D v \rho}{\mu_e}$

Friction Factors for Any Type of Commercial Pipe [18]

152
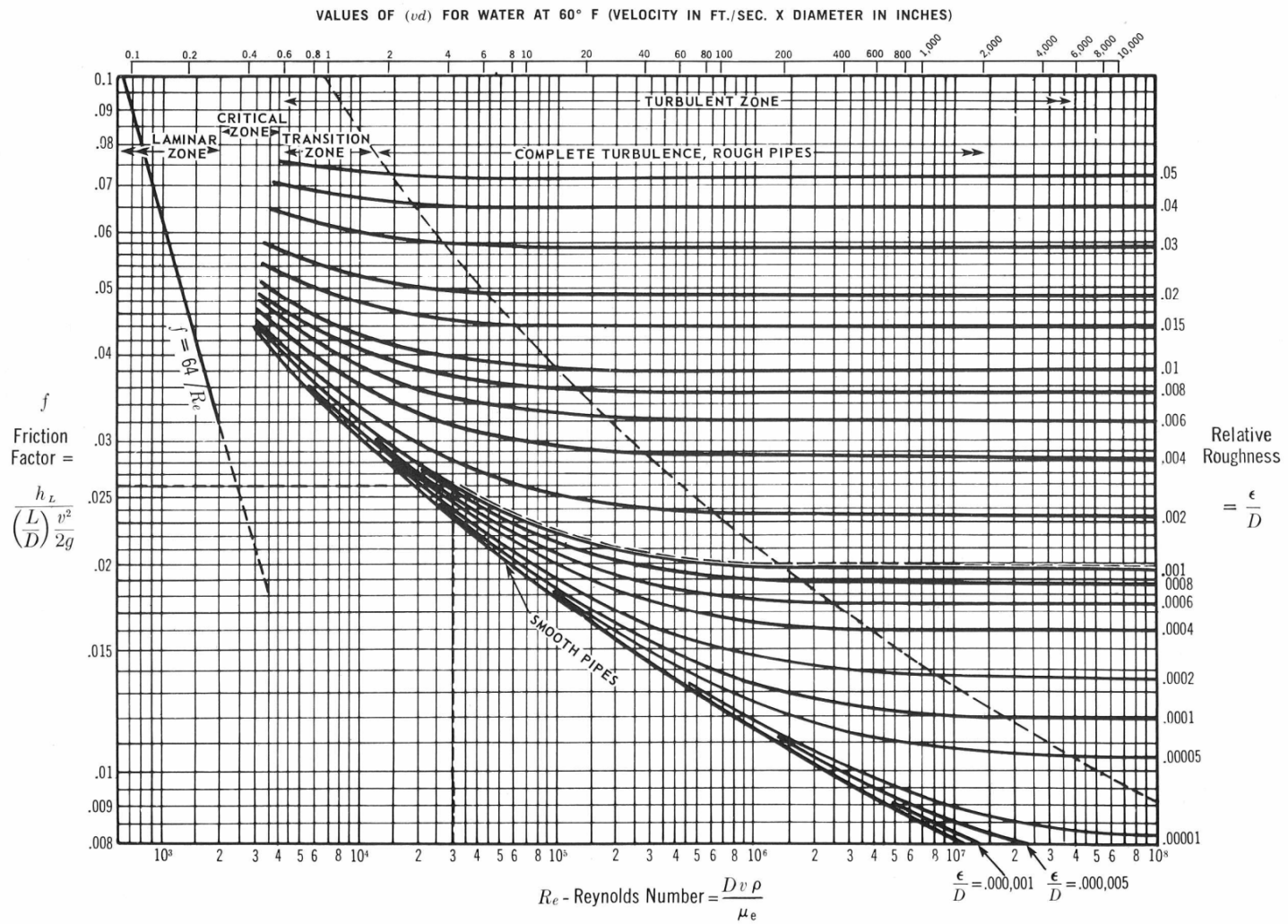
Friction Factors for Clean Commercial Steel Pipe[18]

VALUES OF (vd) FOR WATER AT 60° F (VELOCITY IN FT./SEC. X DIAMETER IN INCHES)

CRITICAL ZONE

LAMINAR ZONE

TRANSITION ZONE

TURBULENT ZONE

COMPLETE TURBULENCE

$f = 64/R_e$

f

Friction Factor $= \dfrac{h_L}{\left(\dfrac{L}{D}\right)\dfrac{v^2}{2g}}$

Inside Diameter, Inches

Nominal Pipe Size, Inches

Schedule Number

R_e – Reynolds Number $= \dfrac{Dv\rho}{\mu_e}$

For other forms of the R_e equation, see page 3-2.
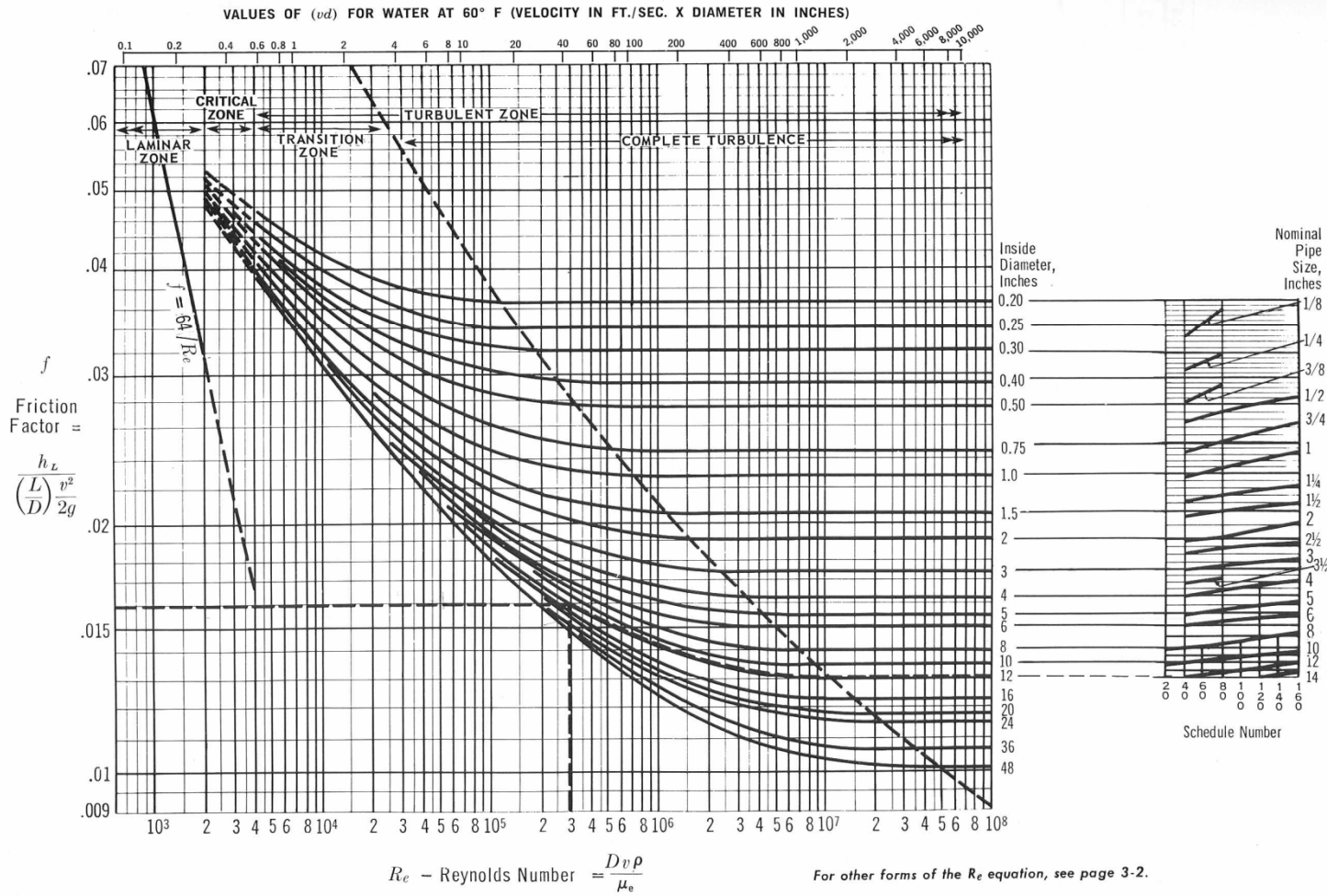
Problem: Determine the friction factor for 12-inch Schedule 40 pipe at a flow having a Reynolds number of 300,000.

Solution: The friction factor (f) equals 0.016.

153

Appendix D :   Properties Through the C-D Nozzle

	Position [mm]	Area [m2]	A / A*	Mach Number	Temperature [K]	Acoustic Velocity [m/s]	Flow Velocity [m/s]	Pressure [Pa]	Density [kg/m3]
Stagnation	0	0.0097	9.2395	0.0628	295	344	22	167198	1.0200
	5	0.0094	8.9755	0.0646	295	344	22	166710	1.0179
Linear	10	0.0091	8.7115	0.0666	295	344	23	166680	1.0177
0.000276497	15	0.0088	8.4476	0.0687	295	344	24	166647	1.0176
7	20	0.0086	8.1836	0.0709	295	344	24	166610	1.0174
	25	0.0083	7.9196	0.0733	295	344	25	166570	1.0173
	30	0.0080	7.6556	0.0759	295	344	26	166526	1.0171
Area 80% half way to throat	35	0.0077	7.3916	0.0786	295	344	27	166477	1.0169
	40	0.0068	6.4785	0.0898	295	344	31	166258	1.0159
	45	0.0058	5.5654	0.1047	294	344	36	165922	1.0144
Linear	50	0.0049	4.6524	0.1256	294	344	43	165365	1.0120
0.000956361	55	0.0039	3.7393	0.1571	294	343	54	164342	1.0075
7	60	0.0030	2.8262	0.2102	292	343	72	162126	0.9978
	65	0.0020	1.9131	0.3217	289	341	110	155631	0.9691
Throat	70	0.0010	1.0000	1.0001	246	314	314	88316	0.6466
	100	0.0014	1.3166	1.6774	189	275	462	35047	0.3341
Linear	130	0.0017	1.6333	1.9605	167	259	507	22721	0.2452
0.000331651	160	0.0020	1.9499	2.1685	152	247	536	16427	0.1945
9	190	0.0024	2.2666	2.3362	141	238	556	12635	0.1612
	220	0.0027	2.5832	2.4780	132	231	571	10126	0.1376
	250	0.0030	2.8999	2.6014	125	224	584	8361	0.1200
	280	0.0034	3.2165	2.7110	119	219	594	7060	0.1064
	310	0.0037	3.5332	2.8099	114	214	602	6069	0.0955
Exit	340	0.0040	3.8498	2.9000	110	210	609	5292	0.0866

Appendix E :   FlowManager Timing and Field of View Screen Shots

Appendix F :   Liquid CO$_2$ Injector Designs

1. Axisymmetric simple circular orifice
   a. Two internal nozzle lengths
      i. flush with inner wall
      ii. cantilever (variable diameter, length, & design)
         (see below)

   b. Advantages
      i. Minimal flow disturbance; non-intrusive
      ii. Simple injector
   c. Disadvantages
      i. Uniform dispersion problems?
      ii. Requires multiple injection points into wind tunnel?
      iii. Requires CO_2 distribution manifold to supply multiple injectors?

Injectors

Main Flow
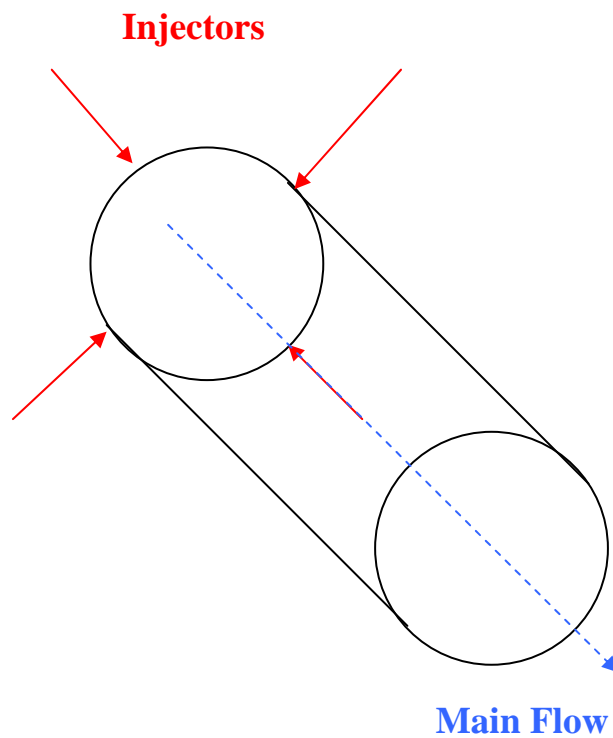
2. Cantilever coaxial sparge tubes with open ends (shroud)
- a. Advantages
    - i. Simple (tube-in-tube)
    - ii. Allows variable accumulation time in larger diameter shroud
    - iii. More direct dispersion control (variable injection center)
    - iv. Variable injection
- b. Disadvantages
    - i. Intrusive particle introduction method
    - ii. More complex mass flow rate into tunnel (same as from tank?)
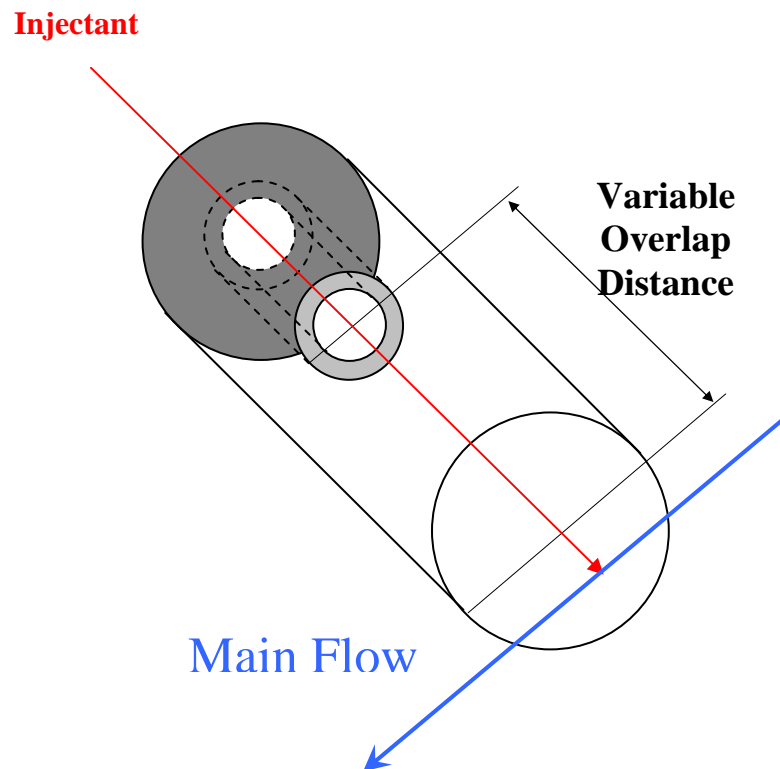
3. Cantilever sparge tube with orifice array
   (variations below)

   a. Advantages
      i. Greatest dispersion control (multiple orifices)
      ii. Variable injection plume profile (geometry)
      iii. Variable atomization (injection angle)
   b. Disadvantages
      i. Can be complex
      ii. Intrusive particle introduction method
      iii. More complex mass flow rate into tunnel
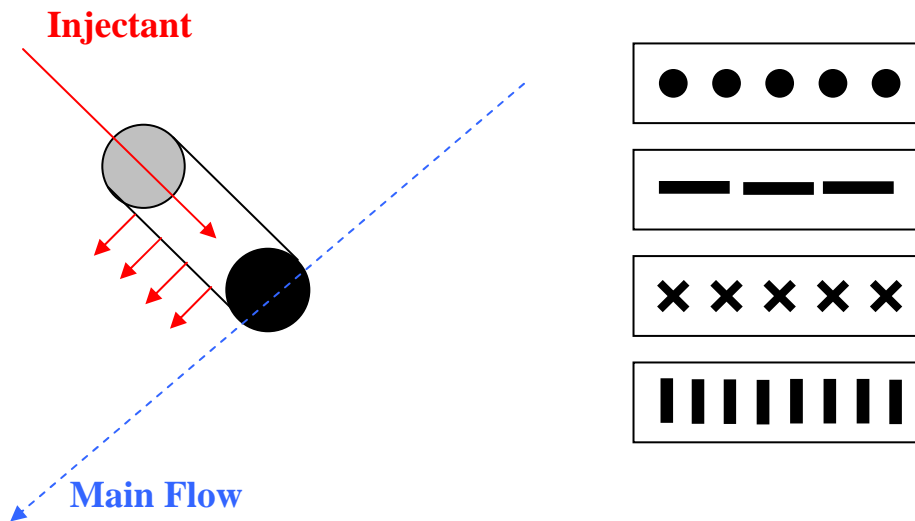
4. Impactor/accumulator - more control over particle size
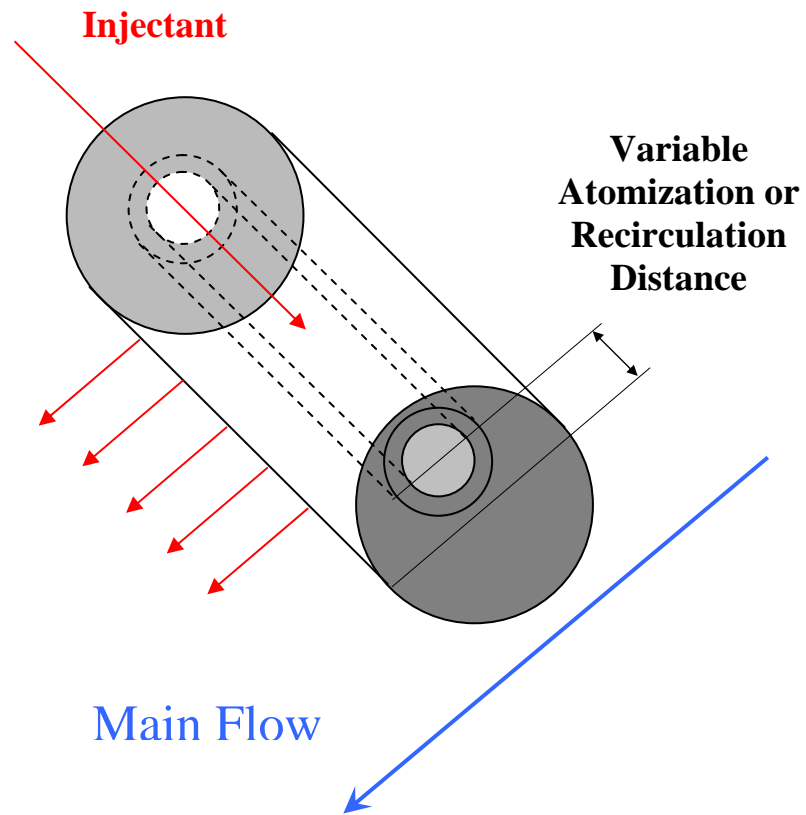
5. **Extended expanding nozzles - allow slightly more time for particles to agglomerate**
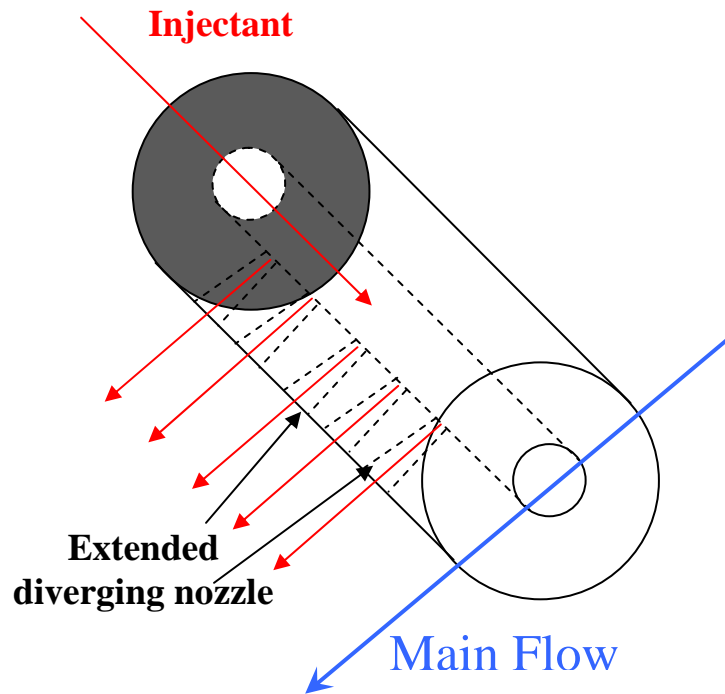
Appendix G :   Solid Works CAD Modeling

Forward Swept Sting   (units in mm)
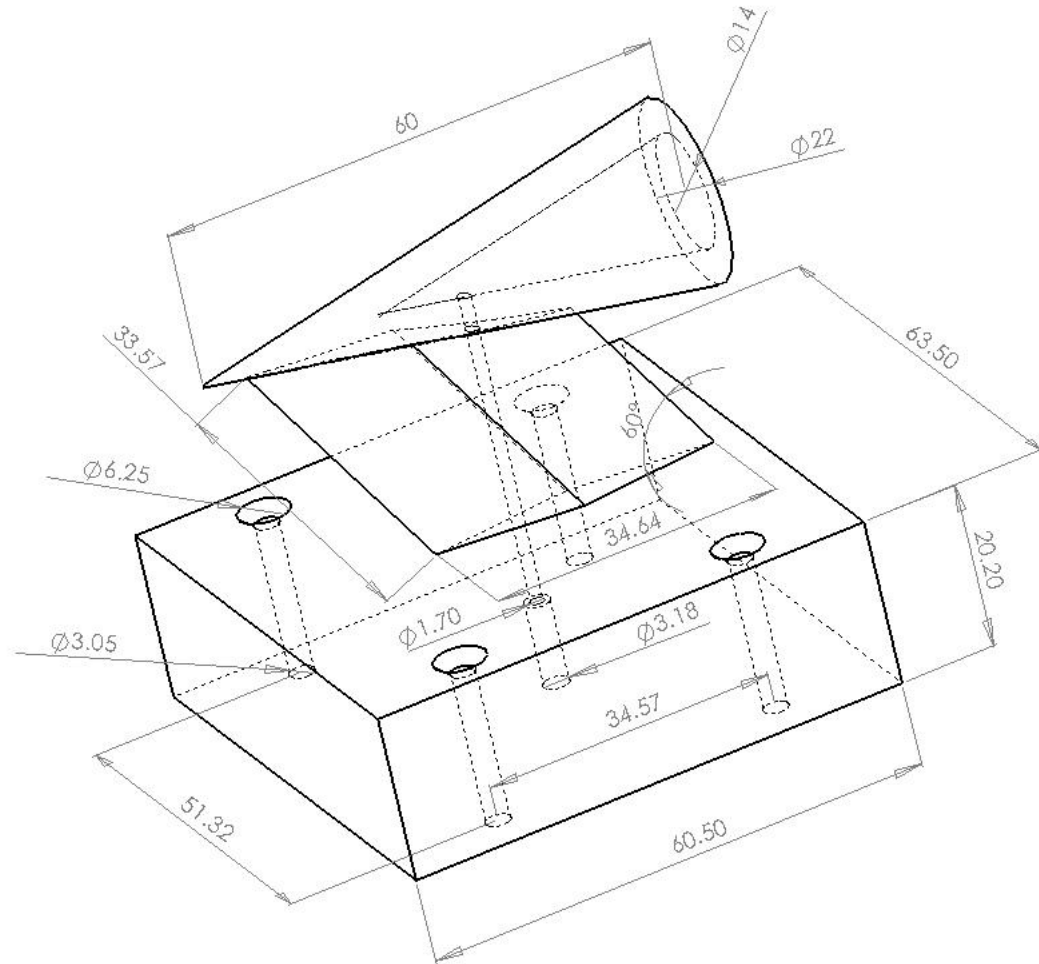
Combination Sting   (units in mm)

170
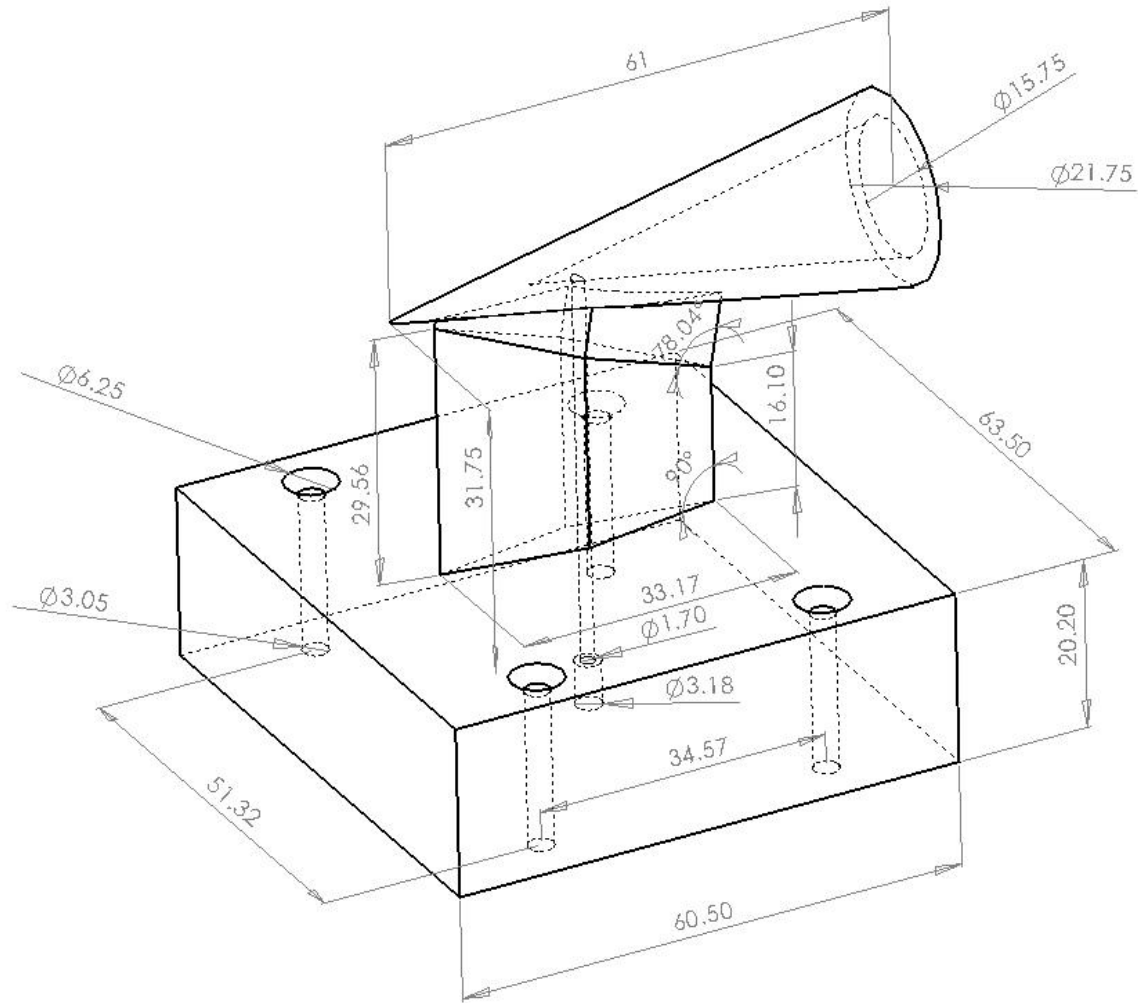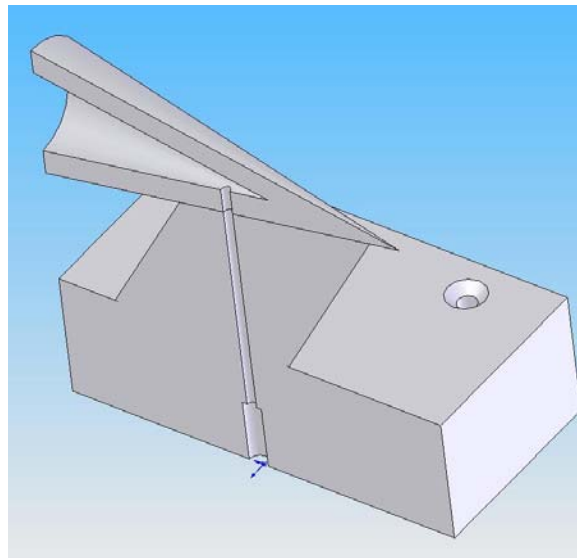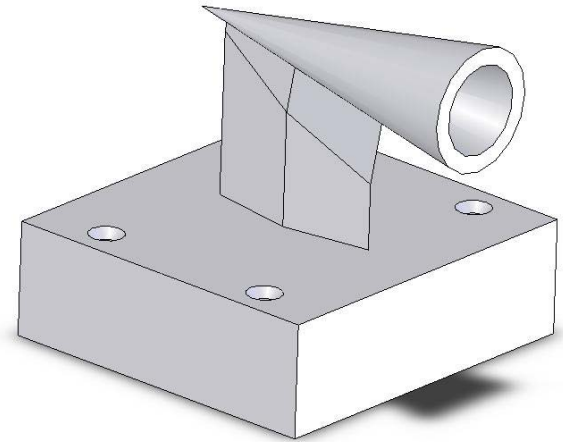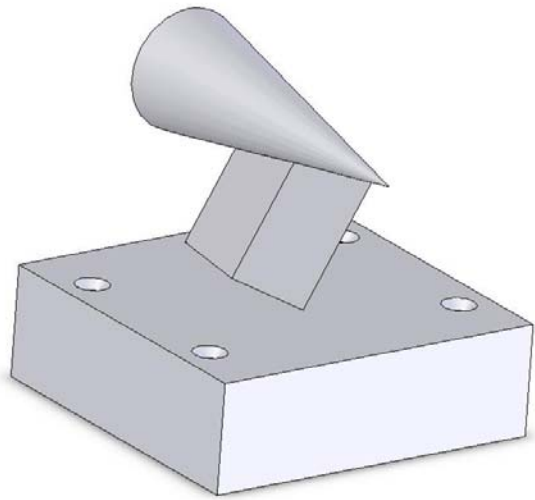
Appendix H :   AFIT Supersonic Wind Tunnel Operating Instructions

PERFORMING A SUPERSONIC WIND TUNNEL PIV TEST
BY: ENS PELTIER, April 2007

Process:

List the steps to performing a PIV test in the AFIT high speed wind tunnel in Rm: 256 Bldg: 640

Preparing the Air Supply: *NOTES*

Ensure the **VACUUM PUMP** and **COMPRESSORS** in Bldg: 644 are powered **ON**
Ensure the **GREEN LEVER VALVE** for the solenoid air supply is **OPEN** and the small black air tank is charged with ≈ 100 psi
Ensure the **GREY WHEEL VALVE** for the wind tunnel air supply is **COMPLETELY OPEN** and the feed tank gage indicates ≈ 160-180 psi   feed tank gage is near the large wind tunnel
Ensure the **RED LEVER VALVE** on the bottom of the main air filter is **CLOSED**   use to drain any water out at the end of each day
SET the regulator **CONTROL PRESSURE** using the **BLACK KNOB VALVE** atop the main air filter to the desired wind tunnel feed pressure

Preparing the Test Section:

Ensure the **MODEL** is properly **INSTALLED** and all test section **WALLS** are **SECURED**
Ensure the **LASER HEAD** is **SECURED** in correct position and **LASER SHIELDS** are **SECURED** in place
Ensure the **CAMERA** is plugged in and powered **ON**   unplug the camera at the end of each day
Ensure the **CAMERA FILTER** is **SECURED** in correct position
Ensure the **RELIEF VALVE** on wind tunnel diffuser is **CLOSED** but lead weight is free to slide open
Ensure all **TRANSDUCERS** are connected and **READING CORRECTLY** on the signal conditioning boxes.

Preparing the Laser and DAQ Systems:

EYE PROTECTION = LASER GOGGLES

TURN ON HALLWAY LASER LIGHT
WARM UP the **LASER**
START Dantec **FLOW MANAGER** software and prepare setup for data acquisition
START LabView **PIV AND AV CONTROL** and prepare for run

Running a PIV Test:

HEARING PROTECTION = EAR MUFFS

TURN OFF ROOM LIGHTS
"START AND SAVE" on the **FLOWMANAGER** software
START the **CO2 FEEDING** and then **CLICK WHITE ARROW** on the **LABVIEW** software   wait until you hear the laser begin to fire
STANDBY to click **START TEST "OFF"** in **LABVIEW** in case auto shut-off doesn't work
STOP CO2 FEEDING after the **LAST LASER PULSE**   -or-   when the **WIND TUNNEL** begins to **SHUT DOWN**

173

PREPARING WIND TUNNEL AIR AND VALVES
BY: ENS PELTIER, April 2007

Process:
Takes you through preparing the wind tunnel air supply, the wind tunnel valve controllers and the DAQ software (LabView).

Preparing the Air Supply:

In compressor/vacuum pump room, BLDG 643,

1   Press **START** on left circuit breaker 1st, let pump run 5 minutes, then rotate switch on right circuit breaker counter-clockwise (CCW) to **MANU**

2   Ensure both compressors are on and running

In wind tunnel lab room,

3   Ensrure the following **VALVES** are **CLOSED**:

Red bleed lever valve on bottom of large air tank (⊥ to pipe is closed); crack open quickly to check for water accumulation

4   Ensure the following **VALVES** are **OPEN**:

Up-high green lever valve on wall (⊥ to pipe is closed)

Grey wheel knob on metal pipe from wall to large grey air tank (CCW is open)

5   Turn black knob valve ontop of large air tank to **SET CONTROL PRESSURE** (∴ stagnation chamber pressure) to start wind tunnel (CCW closes valve, P->0)

NOTE: To a first approximation, stagnation pressure should be 4X the maximum expected vacuum pressure; increase for larger test section models.

A high stagnation pressure gives a shorter run time and a larger mass flow rate (see equations on "Test Environment" page)

Preparing LabView:

6   Start LabView and open **PIV and AV CONTROL.vi**

NOTE: Should be located in the folder "MY DOCUMENTS - VI's - AV CONTROL VI - AV CONROL"

7   Ensure **START, PIV**, **AIR** and **VACUUM** toggle switches are set to **ON** (you should see all green)

NOTE: This should not start the tunnel, merely prepare the program

8   Set the **MAX VACUUM** pressure to the level at which you would like the wind tunnel to automatically stop

NOTE: Generally 3-4 psia is good; anything higher and it takes awhile for the vacuum tanks to empty out again

9   If you would like to record the transducer pressures during the run, turn **DATA LOGGING ON** and select the file and folder location

174

CAMERA CALIBRATION & LASER PLACEMENT

BY: ENS PELTIER, April 2007

Process:

In order for the camera to acquire usable images it must be focused on the plane of the laser sheet.

Camera and Test Section Preparation:

1   Secure camera support at desired position on work table

2   Position camera at desired height above test section and in desired orientation to capture desired image (may need to be adjusted during calibration)

3   Remove test section wall(s)

4   Insert block covered in calibration pokie-dot paper or a ruler

6   Ensure camera is plugged in and powered on

Calibration Image Acquisition using FlowManager:

7   Left click top drop down menu "**Run - Online Acquisition**" and create a new image map if one does not currently exist.

8   Left click "**Continuous**" to see current camera image (hit "T" on keyboard to toggle between 1st and 2nd frame)
          Note: Frame 1 and 2 may look different due to different exposure times. Use the best one (2nd frame usually)

9   Focus camera so pokie-dots are in focus keeping the camera aperture as open as possible (a low f-stop, about 4, helps to reduce speckle and capture all particles)
          Note: You can also place a high definition image in the focus plane to get a good focus, but remove before the next step

10   Left click top drop down menu "**Run - Online Acquisition - Start and Save**" to acquire and save DOTS image (ensure 1 burst and 1 record only)

11   Left click top drop down menu "**Setup - Field of View - Measure - Browse**" to select calibration Image

12   Enter **Abs. Distance = 5mm** (for pokie-dots) and then **LEFT CLICK** on the center of one dot, and **RIGHT CLICK** on the center of a dot horizontally or vertically adjacent.

13   A new scale factor is calculated. Click **OK** and then uncheck "Scale Factor Preliminary"
          Note: The FlowManager Manual gives equations to estimate appropriate camera height (scale factor) for a given setup.

Laser Sheet Placement:

14   Secure laser mount to work table centered on test location and secure laser lens to laser mount

15   Secure the laser trap centered behind the focus plane of the camera

16   Go through the laser warm up procedures **EYE PROTECTION**

17   While firing the laser on low power, adjust the height so the laser sheet is seen reflecting in the focus plane of the camera

18   Remove the camera calibration material, install the test section model and replace the test section walls

19   While firing the laser on low power rotate the laser head so the sheet is illuminating the desired region of the test section
          Note: Look into finding users manual for cylindrical lens in order to characterize light sheet dimensions
                      Could possibly use a fog generator to visualize laser sheet for accurate dimensions

20   When needed. move the entire work table top up and down to readjust the laser height. This will keep the camera, laser, laser trap, etc. relatively locked in position.

TURNING ON DANTEC SOLO PIV LASER

BY: ENS PELTIER, April 2007

2 minute warm-up	Toggle **SWITCH** on back of laser tower to **ON** "	" Turn **KEY** to **ON** "	"and **PRESS START** button Set system to **LOW** power Set lasers to **INTERNAL TRIGGER (both)** Engage by pressing **LASER EMISSION (both)**

10 - 15 minute warm-up	Press start button to put lasers on **STANDBY** Switch system to **HIGH** power Reengage system with **LASER EMISSION (both)**

Prepare to Run Test	Press start button to put lasers on **STANDBY** Set lasers to **EXTERNAL TRIGGER (both)** Press **LASER EMISSION (both)** to prepare for trigger

Lasers will now be controlled by the DANTEC FlowManager Software…

...At end of testing (after you've ensured your last dataset is recorded), turn off laser

Turning laser off	Press **STOP** button Turn **KEY** to **OFF** " 0 " Toggle **SWITCH** on back of laser tower to **OFF** " 0 "

PIV SYSTEM START-UP
BY: ENS PELTIER, April 2007

Process:

Takes you through turning on the DANTEC PIV acquisition hardware and software. Hardware includes the computer running the DANTEC system and the FlowMap System Hub. Software includes Dantec Flow Manager.

Initialize DANTEC System Hub:

1 Ensure PC is powered on

2 Start DANTEC FlowManager software

3 Press **POWER** button on **FlowMap System Hub** box (wait ≈ 1 minute for ready noise and blue "Power On" light)

4 Left click top drop down menu "**Run - Initialize System Unit - Transfer**" to transfer setup info from PC to System Hub

Setting Up FlowManager to Collect PIV Data:

NOTE: See Chapter 8 in FlowManager Manual to learn basics

5 **Open** previous **DATABASE** (.fdb) you were working with or create a new one (ctrl+N)

6 **CLICK** on current **PROJECT FOLDER** of create a new one (ctrl+N):

7 **CLICK** on current **SETUP** or create a new setup by right clicking on project folder or ctrl+N

NOTE: Once you record a dataset, your abilities to alter the current setup will be restricted

8 To open PIV system acquisition panel, "**Run - Online Acquisition**"

NOTE: Current settings will match those from the previous run; modify if necessary.

NOTE: Must re-open "Online Acquisition" before each run

Shutdown DANTEC System Hub:

9 Left click top drop down menu "**Run - Shutdown System Unit**"

10 Press **POWER** button on **FlowMap System Hub** box

11 Close FlowManager software

RUNNING THE WIND TUNNEL
BY: ENS PELTIER, April 2007

Process:

Takes you through the final steps of performing a CO2 injection PIV wind tunnel test.

Preparing and Injecting the CO2:
Running the Tunnel and Collecting Data:

EAR & EYE PROTECTION

1. Record initial mass of tank in kilograms (or **ZERO** out scale to read mass deficit at end of run)
2. Ensure all fittings and connections are secure and put on protective gloves
3. Turn **LIGHTS OFF** in the room once operators are in position
4. Using the FlowManager software, select **"First Burst on Trigger, Subsequently use Fixed Time Interval"**
5. To start the PIV system, left click "**Run - Online Acquisition - Start and Save**"

    NOTE: Ensure you have opened the online acquisition (OLA) while the correct setup is highlighted (OLA must be reopened before each run)
6. Left click **RUN** button on LabView toolbar (looks like an white right arrow)

    NOTE: The wind tunnel should stop at the specified vacuum pressure

    NOTE: Can stop the wind tunnel at any time by toggleing "START TEST" switch to OFF

    NOTE: Do not try to stop wind tunnel with toolbar stop sign button, it won't work
7. Turn wheel valve atop **CO2** tank CCW completely **OPEN** (until it stops ≈ 10 turns) **IN UNISON** with step above and start watch
8. Standby and turn wheel valve atop **CO2** tank CW completely **CLOSED** (until it stops) on command and stop watch
9. Record final mass of tank in kilograms [kg] and CO2 run time in seconds [s]

    NOTE: Can use timer on LabView to record run time instead of stop watch

AFIT SUPERSONIC WIND TUNNEL
RM: 256   BLDG: 640

	NUMBERS	UNITS	NOTES
Wind Tunnel - General			
Type:	open circuit pressure-vacuum blowdown		
Test Section Dimensions	2.5 x 2.5 x 11	inches	
Current Nozzle Design Speed:	2.9	Mach	
Nozzle Wall Thickness:	1	inch	
Measured Throat Dimensions:	2.5" x 1.25" = 3.125	in^2	
Calculated Throat Dimensions:	1.62	in^2	from isentropic theory
Cavity Dimensions:	2 1/2 x 2 3/8 x 3 3/16	inches	
High Pressure Air:	160 - 180	psia	
Required Pressure Ratio to Run (Po/Pvac):	3		empty test section
Instrumentation			
Signal Conditioning Boxes:	ENDEVCO, Model 4428A		
Transducers:			
Control Pressure:	50	psig	needs to be recalibrated
Stagnation Chamber:	50	psig	needs to be recalibrated
Test Section:	50	psia	needs to be recalibrated
Vacuum Tank:	15	psia	needs to be recalibrated
Thermocouples:			
Stagnation Chamber:	??	K	needs to be recalibrated

AFIT SUPERSONIC WIND TUNNEL
RM: 256   BLDG: 640

CO2 Injection System

	NUMBERS	UNITS	NOTES
### CO2 Nozzle Injector			
Shroud Injector:			
Shroud and Feed Tube Material:	304 S.Steel		
Shroud Dimensions:	1/4 OD x 3/16 ID	inches	
Shroud Length:	190	mm	
Feed Tube Dimensions:	1/16 OD x 10-30/1000 ID	inches	
Feed Tube Length (initial):	95	mm	
Overlap Length (initial):	20	mm	
Feed Tube Length (final):	55	mm	
Overlap Length (final):	15	mm	

CO2 Test Section Injector

Cavity Shroud Injector:			
Plate Dimensions:	61 x 64 x 3.175	mm	W x D x H
Shroud and Feed Tube Material:	304 S.Steel		
Shroud Dimensions:	1/8 OD x 1/16 ID	inches	
Shroud Length:	35	mm	
Feed Tube Dimensions:	1/16 OD x 10-30/1000 ID	inches	
Feed Tube Length:	55	mm	
Overlap Length (shroud injector):	10	mm	
Cone Injector:			
Feed Tube Dimensions:	1/16 OD x 20/1000 ID	inches	
Feed Tube Length:	130	mm	

Compression Fittings

Maunfacturer:	Swagelok		
Material:	Stainless Steel and Teflon		

AFIT SUPERSONIC WIND TUNNEL
RM: 256   BLDG: 640

PIV and DAQ SYSTEM

NATIONAL INSTRUMENTS DAQ System:

Computer:	PXI-1042
Computer Board:	PXI - 6070E multifunction I/O
DAQ Board:	BNC - 2120
Software:	Labview 8, Version 8.0, 2005

DANTEC DYNAMICS PIV System:

Computer:	Dell Dimension 8300, Pent 4, 3 GHz, MS XP 2002
FlowHub:	System Hub, 2003
Software:	FlowManager, Version 4.50.17, 2005

AFIT SUPERSONIC WIND TUNNEL
RM: 256 BLDG: 640

KODAK REDLAKE MEGAPLUS Model ES 4.0/E

Camaer Type:	4 Mpixel, Monochromatic, CCD	grey scale pictures, charged couple device
Total Number of Pixels:	2048 (H) x 2048 (W)	given in camera users manual
Photosensitive Pixels:	0 - 2047	indexes the pixels; must be 0-2047
Pixel Dimensions [μm]:	7.4 x 7.4	given in camera users manual
Pixel Pitch [μm]:	9.55 x 9.55	center to center distance between adjacent pixels; calculated from pixel dimension and fill ratio for square pixel
Fill Ratio:	60%	fill factor: fraction of the area of one cell used for light collection (100% for full-frame sensor)
		storage cells adjacent to light sensative cells reduce fill factor
Number of Output Channels:	2	can be set to 1 or 2
Output data rates [MHz]:	10, 20 or 40	depends on # channels and binning used (pg. 3-5, camera users manual)
Run Modes:	Continuous	15 fps in 2x2 and 30 fps in 1x1
	Controlled	
	Triggered	
	Double Exposure (DE)	11.4 fps (max) and 5.6 triggers/second (max)
Exposure Time [μs]:	98 (minimum)	using electrical shutter
	64946	in double exposure/continuous mode with 2K x 2K binning
	32495	in double exposure/continuous mode with 1K x 1K binning
	112298 (max)	in triggered mode
Transfer Pulse Width [ms]:	12	minimum time required to transfer charge from photo pixel to storage cell (can change but will decrease quality)
Binning Modes:	1K x 1K	binning groups neighboring pixels
	2K x 2K	decreased frame rate and signal to noise ratio
Frame Rate:	30 (max at 1K x 1K)	
	15 (max at 2K x 2K)	
	11.4 (double exposure)	
Trigger:	Positive or negative wave signal	
	2.5 Volts	
	Trigger pulse >= 100 ns	

Command:	**Action**	
RDM 2	dual channel readout	
MDE DE	double exposure mode	
BNS 1	no binning performed (2Kx2K)	
BNS 2	binning (1Kx1K)	
TPD xxx	transfer pulse delay	sets exposure time for 1st image. Exposure time for 2nd image depends on BNS.
DGN 4	camera gain increased 4x	
DEF ON	Defect concealment on	corrects abnormal input from irregular pixels with averages from neighboring pixels

NOTES: double frame mode uses 2 separate frames to capture the laser pulses (for use with cross-correlation)
integration time: exposure time that light can effect CCD pixel (see FlowManager glossary)
close time: I think it's the desired integration time (max + delay)

Camera Lens: NIKON 60mm AF Micro Nikkor, manual
Camera Filter: MELLES GRIOT, 50mm, 509 nm center wavelength, 90% distribution thickness = 52 nm, 67.4% transmission

AFIT SUPERSONIC WIND TUNNEL
RM: 256 BLDG: 640

NEW WAVE RESEARCH Solo 120

# of Lasers: 2

Class of Lasers: IV (400mJ/4ns)

Lasing Medium: Solid Crystal: Nd-Yag (neodyndium yittrium aluminum garnett)

Wave Length: 1064 nm (IR) halved to 532 nm (green)

Power: 120 mJ @ 532 nm

Run Mode: Pulsed

Repititon Rate: 15 Hz maximum

Beam Energy: 120mJ

Beam Diameter: 4.5mm

Beam Divergence: < 2mrad

Optimum Q-Stitch Setting: 180-200 μs

Laser Pulse: 3-5 ns

Laser Housing:

length: 22.4 in

width: 9.24 in

height: 4.86 in

weight: 34 lbs

Attachments:

Dantec Dynamics Mirror Arm
D.D. Cylindrical Lens - 80 x 20 Light Sheet

Appendix I :   LabView Graphical Code

True

PIV On Time Delay [ms]
I32

High Pressure Air
T F

Vacuum
T F

PIV Trigger
T F

PIV and AV ON Control.vi

Air ON Time Delay [ms]
I32

0

Start Test
T F

Max Vac
T F

Max Vacuum Pressure [psi]
DBL

Vacuum Pressure [psi]
DBL

Vacuumn [psia]
DBL

Test Section [psia]
DBL

Stilling Chamber [psig]
DBL

Control Pressure [psig]
DBL

Data Logging
OFF
T F

Pressure Log File Name
Path

Write To
Measurement
File

Signals

Sampling Frequency
DBL

# of Samples per Loop Iteration
DBL

DAQ Board 3

Current Time Stamp
DBL

Test Run Time [s]
1.23
DBL

Loop Iterations
DBL

i

1

Initial Time Stamp
DBL

Start Up

186

187

Running

Shut Down

189
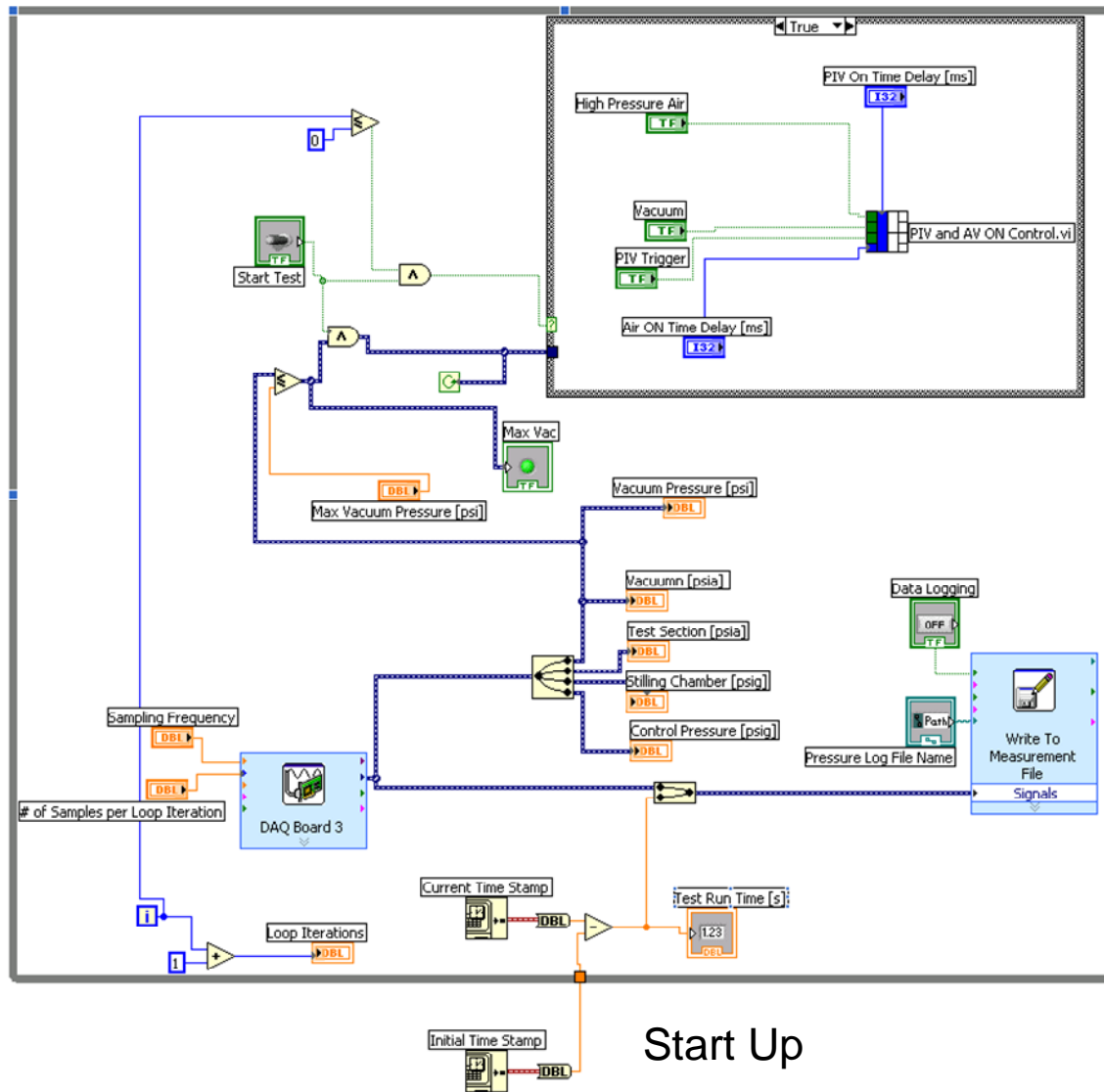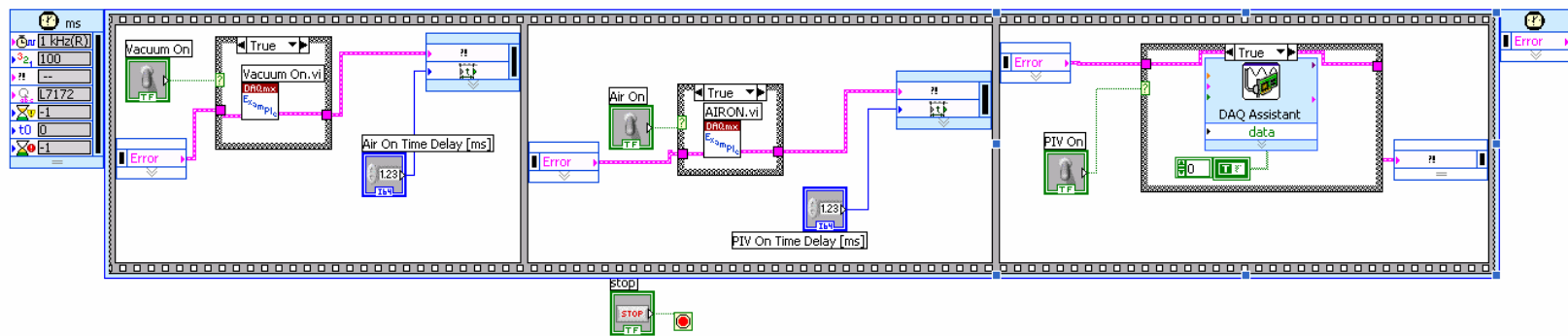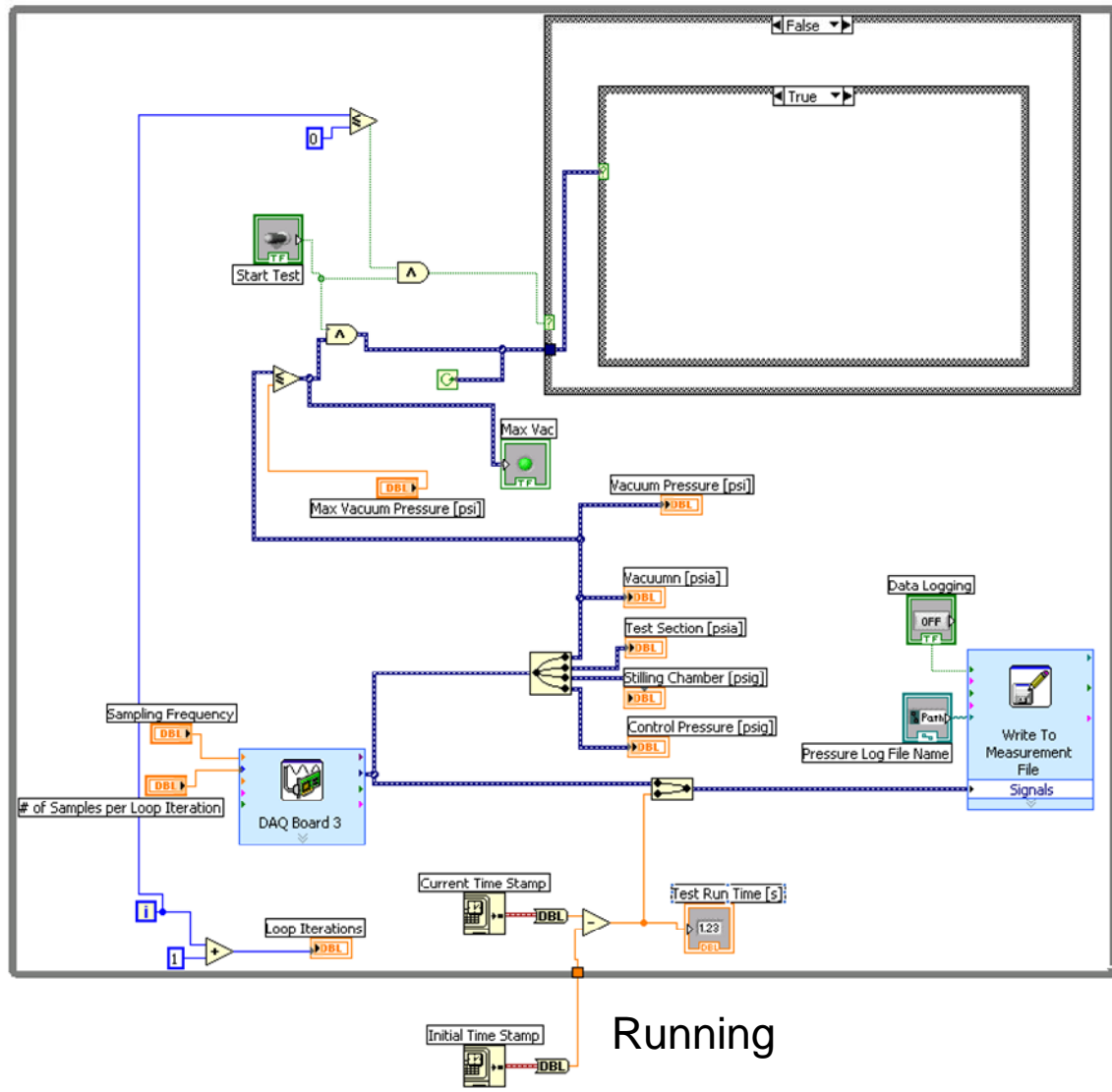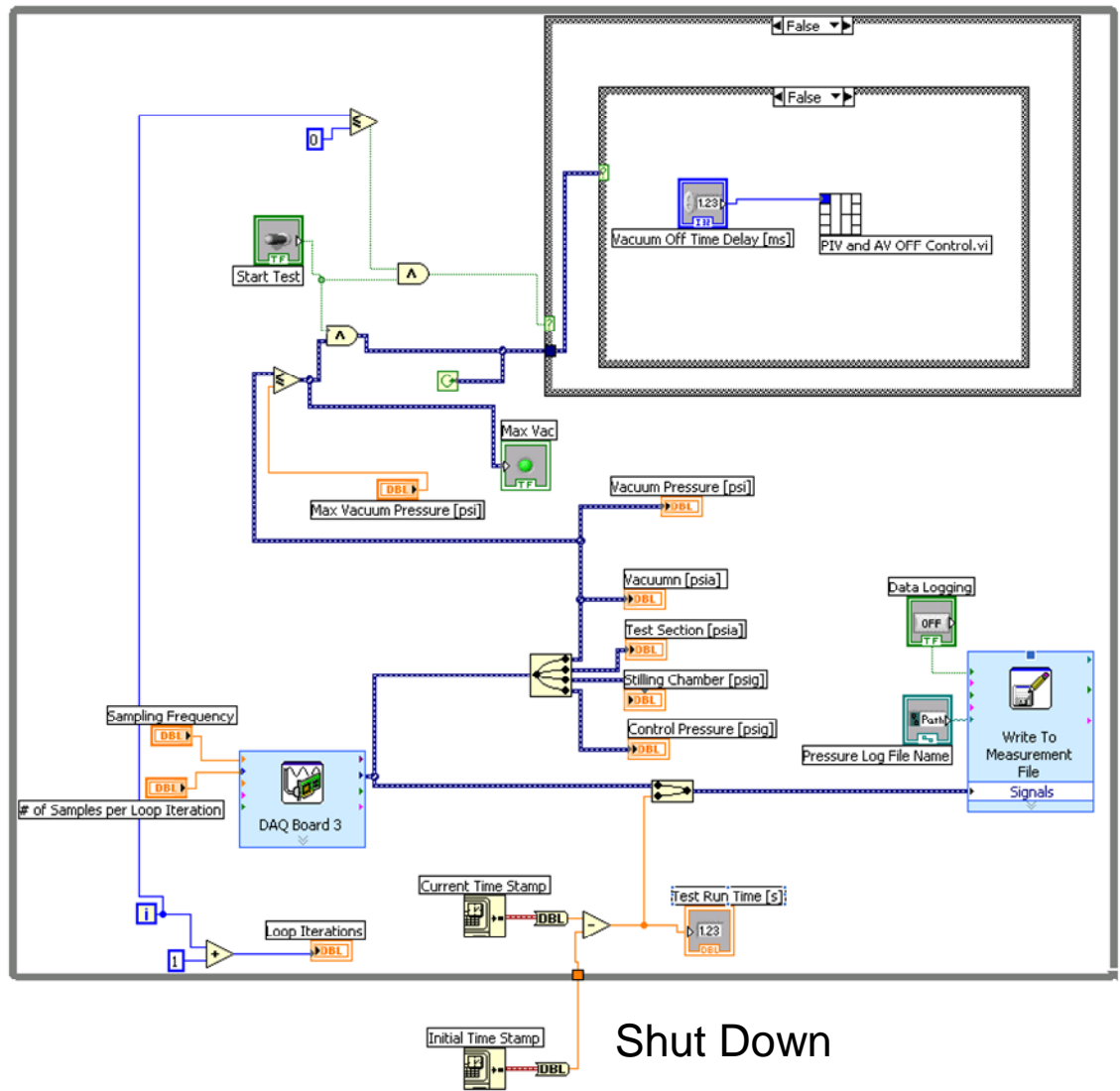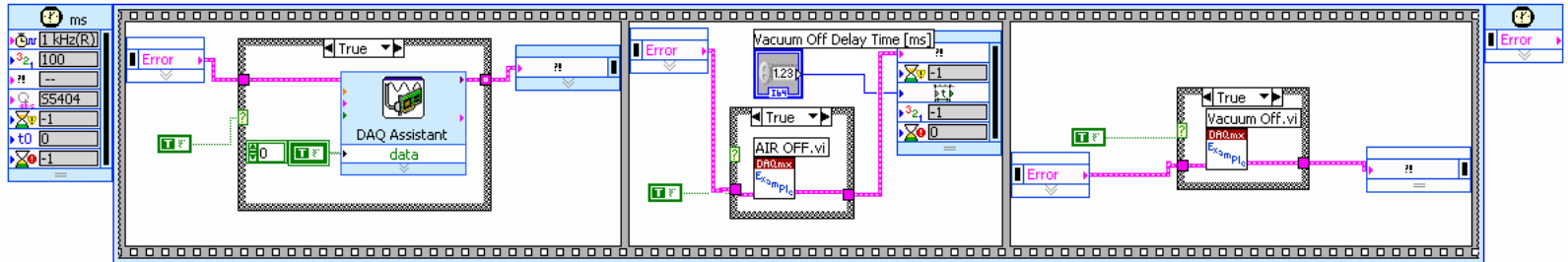
Appendix J :   FlowManager Post Processing Screen Shots

194

Appendix K :   FlowManager Figure Making Screen Shots

References

Air Products (2004). *Safetygram #30: handling liquefied compressed gas, Brochure No. 900-01-101-US*. Air Products and Chemicals Inc.

Anderson, J. (2003). *Modern compressible flow: with historical perspective*. Boston: McGraw Hill.

Bjorge, S., Reeder, M., Subramanian, C., Crafton, J. and Fonov, S. (2005). Flow around an object projected from a cavity into a supersonic freestream. *American Institute of Aeronautics and Astronautics, 43*(7), 1465-1474.

Brown, R. (1985). Seeding materials: Health and safety considerations. *NASA Langley Research Center: Wind Tunnel Seeding Systems for Laser Velocimeters*, *N86-11454*, 211-219.

Chen, T., Smith, C., Schommer, D. and Nejad, A. (1993). Multi-zone behavior of transverse liquid jet in high-speed flow. *31st AIAA, Aerospace Sciences Meeting and Exhibit; Reno NV; USA; 11-14 Jan. 1993, AIAA Paper 1993-0453*.

Crane (1988). *Flow of fluids through valves, fittings and pipe. Technical paper No. 410*. Crane Company, Joliet IL.

Crosswy, F. (1985). Particle size distributions of several commonly used seeding aerosols. *NASA Langley Research Center: Wind Tunnel Seeding Systems for Laser Velocimeters*, *N86-11441*, 53-75.

Dantec Dynamics A/S (2002). *FlowManager software and introduction to PIV instrumentation: software users guide. Publication No. 9040U3625*. Dantec Dynamics, Skovlunde Denmark.

DeLapp, C. (2006). *Particle image velocimetry using novel non-intrusive particle seeding*. MS thesis, AFIT/GAE/ENY/06-J01. Graduate School of Engineering and Management, Air Force Institute of Technology, Wright-Patterson AFB OH.

DeLapp, C., Reeder, M. and Crafton, J (2006). Clean seeding material for particle image velocimetry measurements. *25th AIAA Aerodynamic Measurement Technology and Ground Testing Conference; San Francisco CA; USA; 5-8 June 2006, AIAA Paper 2006-2807*.

Fuller, R., Wu, P., Kirkendall, K. and Nejad, A. (2000). Effects of injection angle on atomization of liquid jets in transverse airflow. *American Institute of Aeronautics and Astronautics, 38*(1), 64.

Hill, P. and Peterson, C. (1992). Mechanics and thermodynamics of propulsion. Massachusetts: Addison-Wesley.

Kochtubajda, B. and Lozowski, E. P. (1985). The sublimation of dry ice pellets used for cloud seeding. *Journal of Climate and Applied Meteorology, 24*(6), 597-605.

Li, H., and Karagozian, A. (1991). Breakup of a liquid jet in supersonic crossflow. *29th AIAA, Aerospace Sciences Meeting; Reno NV; USA; 7-10 Jan. 1991, AIAA Paper 1991-0689.*

McNiel, C. (2007). *Demonstration of clean particle seeding for particle image velocimetry in a closed circuit supersonic wind tunnel*. MS thesis, AFIT/GAE/ENY/07-M19. Graduate School of Engineering and Management, Air Force Institute of Technology, Wright-Patterson AFB OH.

Melling, A. (1997). Tracer particles and seeding for particle image velocimetry. *Measurement Science & Technology, 8(12),* 1406-1416.

Mercer, C. (2003). *Optical metrology for fluids, combustion and solids*. Boston: Kluwer Academic Publishers.

Merzkirch, W. (1974). *Flow visualization*. New York: Academic Press.

Ames Research Staff (1953). Report 1135: Equations, tables and charts for compressible flow. *National Advisory Committee for Aeronautics, Ames Aeronautical Laboratory, Moffett Field CA.*

Rockwell, R. and Naudascher, E. (1978). Self-sustaining oscillations of flow past cavities. *Journal of Fluids Engineering, June 1978, Vol. 100,* 152-165.

Sabroske, K. (1993). Seeding materials for use in laser anemometry. *31st Aerospace Sciences Meeting and Exhibit; Reno NV; USA; 11-14 Jan. 1993, AIAA Paper 1993-0006.*

Scarano, F. and van Oudheusden, B. (2003). Planar velocity measurements of a two-dimensional compressible wake. *Experiments in Fluids, 34(3),* 430-441.

Toromont Process Systems. *All about carbon dioxide: properties, applications, sources and plants*. Toromont Industries, Inc.

Wittemann. *Physical properties of carbon dioxide. Bulletin No. DataProp1003*.
Witteman Company LLC, Palm Coast FL.

Zhang, X., and Edwards, J. (1990). An investigation of supersonic oscillatory cavity
flows driven by thick shear layers. *Aeronautical Journal, Dec. 1990,* 355-364.

Vita

ENSIGN DONALD WALLACE PELTIER III, a native Austinite for 20 years, attended David Crockett High School in Austin, Texas, where he graduated as Salutatorian with highest honors in 2001. In true Texas fashion, ENS Peltier attended The University of Texas at Austin from 2001 – 2006, graduating with a Bachelors of Science in Aeronautical and Aerospace Engineering. While at UT Austin, ENS Peltier was also a member of the UT Naval Reserve Officer Training Corps. During his five years at UT Austin, ENS Peltier led the battalion of midshipman under many different titles including Sailing Officer, Physical Training Officer, Company Commander and Battalion Commander. Ensign Peltier earned his commission as a Naval Officer in May 2006 and was order to the Air Force Institute of Technology to continue his engineering education and earn a Masters of Science in Aeronautical Engineering. Upon successful completion of his studies in June 2007, ENS Peltier is ordered to flight school at NAS Pensacola where he will prepare to serve his country as a naval aviator.

REPORT DOCUMENTATION PAGE	*Form Approved* *OMB No. 074-0188*

The public reporting burden for this collection of information is estimated to average 1 hour per response, including the time for reviewing instructions, searching existing data sources, gathering and maintaining the data needed, and completing and reviewing the collection of information. Send comments regarding this burden estimate or any other aspect of the collection of information, including suggestions for reducing this burden to Department of Defense, Washington Headquarters Services, Directorate for Information Operations and Reports (0704-0188), 1215 Jefferson Davis Highway, Suite 1204, Arlington, VA 22202-4302. Respondents should be aware that notwithstanding any other provision of law, no person shall be subject to a penalty for failing to comply with a collection of information if it does not display a currently valid OMB control number.
PLEASE DO NOT RETURN YOUR FORM TO THE ABOVE ADDRESS.

1. REPORT DATE *(DD-MM-YYYY)* 14 Jun 07	2. REPORT TYPE **Master's Thesis**	3. DATES COVERED *(From – To)* **June 2006– Jun 2007**
4. TITLE AND SUBTITLE Performing Particle Image Velocimetry In A Supersonic Wind Tunnel Using Carbon Dioxide As The Seed Material		5a. CONTRACT NUMBER 07 - 301
		5b. GRANT NUMBER
		5c. PROGRAM ELEMENT NUMBER
6. AUTHOR(S) Peltier, Donald W., Ensign, USN		5d. PROJECT NUMBER
		5e. TASK NUMBER
		5f. WORK UNIT NUMBER
7. PERFORMING ORGANIZATION NAMES(S) AND ADDRESS(S) Air Force Institute of Technology Graduate School of Engineering and Management (AFIT/EN) 2950 Hobson Way WPAFB OH 45433-7765		8. PERFORMING ORGANIZATION REPORT NUMBER AFIT/GAE/ENY/07-J17
9. SPONSORING/MONITORING AGENCY NAME(S) AND ADDRESS(ES) James Grove (937.785.8484, James.Grove@WPAFB.AF.MIL) CAPT Chris McGaha, USAF (Christopher.McGaha@AFIT.EDU) AFRL/VAAI WPAFB OH 45433		10. SPONSOR/MONITOR'S ACRONYM(S)
		11. SPONSOR/MONITOR'S REPORT NUMBER(S)

12. DISTRIBUTION/AVAILABILITY STATEMENT
      APPROVED FOR PUBLIC RELEASE; DISTRIBUTION UNLIMITED.

13. SUPPLEMENTARY NOTES

14. ABSTRACT
Particle image velocimetry (PIV) was performed utilizing clean seed particles generated by injecting liquid carbon dioxide (CO_2) directly into an open-circuit blowdown Mach 2.9 supersonic wind tunnel. Rapid atomization and cooling of the liquid CO_2 created a preponderance of nearly uniform and well dispersed microscopic dry ice particles which were illuminated using a frequency double Nd:YAG laser. Ample light was scattered from the flow tracers, which provided a strong signal to noise ratio. The particles completely sublimed into an innocuous gas downstream of the test section causing no side effects or problems with wind tunnel operation. A variety of geometries were inspected using PIV. In addition to empty test section characterization, flow aft of a cone and transverse injection through a long shallow cavity was visualized and adaptive cross-correlation vector maps were computed. These vector maps revealed many relevant flow structures pertinent to each test setup. Measured velocities followed the trends expected for each test setup but the vector magnitudes were shifted 3-9% below those predicted by theory. Procedures and information pertinent to liquid CO_2 injection are provided to help researchers implement this process in similarly scaled supersonic wind tunnels.

15. SUBJECT TERMS
Particle Image Velocimetry, Seed Particles, Tracer Particles, Carbon Dioxide, Clean Seeding, Supersonic Wind Tunnel

16. SECURITY CLASSIFICATION OF:			17. LIMITATION OF ABSTRACT	18. NUMBER OF PAGES	19a. NAME OF RESPONSIBLE PERSON Dr. Mark F. Reeder (AFIT/ENY)
REPORT U	ABSTRACT U	c. THIS PAGE U	UU	230	19b. TELEPHONE NUMBER *(Include area code)* (937) 255-3636, ext 4530; e-mail: Mark.Reeder@afit.edu

Standard Form 298 (Rev: 8-98)
Prescribed by ANSI Std. Z39-18

211